Distribution Agreement

In presenting this thesis or dissertation as a partial fulfillment of the requirements for an advanced degree from Emory University, I hereby grant to Emory University and its agents the non-exclusive license to archive, make accessible, and display my thesis or dissertation in whole or in part in all forms of media, now or hereafter known, including display on the world wide web. I understand that I may select some access restrictions as part of the online submission of this thesis or dissertation. I retain all ownership rights to the copyright of the thesis or dissertation. I also retain the right to use in future works (such as articles or books) all or part of this thesis or dissertation.

Signature:

_____ _____

Xia Hong Date

Flow of Quasi-two-dimensional Emulsions: Clogging, Avalanches, and Dynamics

By

Xia Hong

Doctor of Philosophy

Physics

Eric R. Weeks
Advisor

Family Fereydoon
Committee Member

Minsu Kim
Committee Member

James Nagy
Committee Member

Connie Roth
Committee Member

Accepted:

Lisa A. Tedesco, Ph.D.
Dean of the James T. Laney School of Graduate Studies

Date

Flow of Quasi-two-dimensional Emulsions: Clogging, Avalanches, and Dynamics

By

Xia Hong

B.Sc., Tsinghua University, China, 2009

Advisor: Eric Richard Weeks, PhD.

An abstract of

A dissertation submitted to the Faculty of the

James T. Laney School of Graduate Studies of Emory University

in partial fulfillment of the requirements for the degree of

Doctor of Philosophy

in Physics

Spring, 2017

Abstract

Flow of Quasi-two-dimensional Emulsions: Clogging, Avalanches, and Dynamics

By Xia Hong

We experimentally study the flow of oil-in-water emulsion droplets in a quasi-two-dimensional system. Due to surfactants coating the droplets, they easily deform and slide past each other, approximating frictionless and soft disks. Similar experiments were done in granular material [1–9] and it is exciting to see both similarities and disagreement between prior results and our new findings.

In Chap. 4, by flowing emulsion using gravity, droplets have chances to clog at the hopper exit. By varying the hopper width, the transition from clogging to unclogging is observed. This clogging at the hopper exit requires a narrow hopper opening that is slightly larger than the droplet diameter and no observation of large arch at the hopper exit. Prior studies with frictional disks found long arch formation and cloggings at the hopper exit with significantly larger hopper openings [1]. However, our simulation work shows the importance of gravity and softness that is leading to the change in the clogging probability.

Chap. 5 uses syringe pump to drive the droplets flowing through a hopper. In this system there is no permanent clogging, unlike gravity driven hopper flow, due to the continuous pumping. The droplets would eventually exit the hopper due to the

pressure build-up in the system. There are three types of very different flow behaviors observed. At the lowest flow rates, the droplets exit the hopper via intermittent avalanches. At the highest flow rates, the droplets exit continuously. The transition is a fairly smooth function of the mean strain rate. This is remarkable because emulsion system is frictionless while friction is crucial in granular material to have avalanche [1–3]. However, there is little or no dependence of the flow behavior on the area fraction of the system.

Chap. 6 is inflating oil droplet into the emulsion in an open chamber to study its dynamic response. We examine both monodisperse and bidisperse sample with a large range of packing fraction. The mean flow is well defined like simple fluid. But the fluctuation of velocity increases as the packing fraction gets further above jamming regardless of the polydispersity of emulsions.

Flow of Quasi-two-dimensional Emulsions: Clogging, Avalanches, and Dynamics

By

Xia Hong

B.Sc., Tsinghua University, China, 2009

Advisor: Eric Richard Weeks, PhD.

A dissertation submitted to the Faculty of the
James T. Laney School of Graduate Studies of Emory University
in partial fulfillment of the requirements for the degree of
Doctor of Philosophy
in Physics

Spring, 2017

Acknowledgments

First and foremost, to the best advisor and mentor I image I'll ever have, I thank **Eric Weeks** for his invaluable advice and guidance. Erics constant encourage and support, sharp insights, optimism, enthusiasm, amazing metaphor in teaching, unique and dry sense of humor made my six years more enjoyable than I could have ever expected. Eric is like a guiding light, remarkable and sometimes uncanny. I always look up to him not only because he is an extraordinary scientific researcher but also because he is a great person. I will forever grateful for all he has done for me.

I also thank my committee members,**Fereydoon Family**, **Connie Roth**, **Alberto Fernandez-Nieves**, and **James Nagy** for their support and suggestions over the years, with extra thanks to Connie for her professional guidance and effort on different perspectives of life beyond graduate school. Thanks to Fereydoon Family for his great mentoring as my advisor for my second rotation project. Thanks to **David Lynn** for teaching me to be a better communicator, teacher, and scientist in the ORDER program.

Thanks to **Dandan Chen** for giving me the lab tour, which is the beginning of my enjoyable journey. She is the first person I met when I visited the Weeks lab as a prospective, highlighting that it would be a great place to work. She is also the previous worker on the emulsion hopper flow experiment. It was very beneficial to have **Kenneth Desmond** as my officemate due to his patient mentoring and willingness to help, especially IDL programming stuff, which I knew nothing about before I joined the lab. Big and special thanks to **Carlos Orellana**, my officemate in the last couple years of my Ph.D. journey. This is not only for his optimism, encouragement, and support to my research as a mentor but also for his cuteness and

entertainment as a fun person in life.

I would like to express my appreciation to all those that I have interacted with over the years in and outside the research lab in our department. There are too many of these people to list everyone but special thanks to **Xin Du**, **Skanda Vivek**, **Cong Cao**, **Janna Lowensohn**, **Gary Hunter** and **Kazem Edmond**. Thanks to all the staff for their patient help with paperwork, electronic and mechanical techniques. Especially, thanks to **Jason Boss**, our lab's IT administrator, who can always ensure the smooth operation of computers in our lab. His thoughtfulness and care about our research and life make the friendship in Weeks lab lasting no matter students come and go over the years.

I thank my roommates and friends **Jane Wei**, **Chao Song** and **Shunyuan Zhang** for being constant sources of support, encouragement, and affection.

Most importantly, thanks to my parents and sister for having faith in me all the times when I was a little kid and during my stint as an undergraduate and graduate student. Their support, encourage and love would be the most invaluable treasure in my life.

Finally, I want to thank the financial support for this research, which was provided by the National Science Foundation Grants CBET-1336401 and the Petroleum Research Fund (47970-AC9), administered by the American Chemical Society. Also thanks to ORDER fellowship for teacher-scholars, organized by David Lynn. I also would like to thank the physics department, Laney Graduate School and Emory University for their support over the years.

Xia Hong

Emory University

Spring 2016

Dedicated to my father Guoping Hong,
my mother Guanxian Wu,
and my sister Xiao Hong.

Contents

List of Figures

List of Tables

Citations to Previously Published Work

Portions of Chapter 4 appears in the experimental work in the following manuscript:

"Clogging of soft particles in 2D hoppers",
Xia Hong, Meghan Kohne, and Eric R. Weeks,
Submitted to *Physical Review E* and received refree reports, Fall 2016
arXiv:1512.02500v2 [cond-mat.soft]

Large portions of Chapter 5 appear in the following manuscript:

"Avalanches of rearrangements in quasi-2D emulsion hopper flow",
Xia Hong, Kenneth W. Desmond, Dandan Chen, Eric R. Weeks,
Submitted to *Physical Review E* and received refree concerns, Spring 2015
arXiv:1503.07569v1 [cond-mat.soft]

Large portions of Chapter 6 appear in the following manuscript:

"Dynamic response to local perturbations in quasi-2D emulsion",
Xia Hong and Eric R. Weeks,
In preparation, to be submitted.

Portions of Chapter 3 appear in the following manuscript:

"Notes for Emulsion Tracking with IDL",
Xia Hong, Janna Lowensohn and Carlos Orellana,
Notes for lab use.

Chapter 1

Introduction

1.1 Soft Materials and Jamming

The three states of matter: solid, liquid, and gas, are adequate for classifying many materials. However, some interesting materials are hard to be categorized in any of these three states. Such materials are very common in our daily lives including shaving cream, mayonnaise, ground coffee, and toothpaste. These materials are known as *soft materials*, and the study of them is in the field of soft condensed matter. A great introductory review can be found in chapter "Soft jammed materials" in the book [3]. Soft materials are typically composed of mixtures of two or more components. Common model systems that people use for experimental study include colloids (microscopic solid particles in a liquid), emulsions (liquid droplets dispersed in another immiscible liquid), foams (air bubbles in a liquid like shaving cream), and granular materials (solid particles in a gas with particle size usually larger than millimeter). They are neither simply liquids nor crystalline solids [4] and share both

solid-like and liquid-like properties.

The transition from a fluid-like state to a solid-like jammed state is recognized as the *jamming transition*. The jamming transition has been attracting people's attention for more than 15 years. P.W. Anderson said in his paper [5]: "The deepest and most interesting unsolved problem in solid state theory is probably the nature of glass and the glass transition. This could be the next breakthrough in the coming decade." This is a non-equilibrium transition that exists in various soft condensed systems including molecular liquids, colloidal suspensions, foam, emulsion and granular systems. Take shaving cream for example: a pile of shaving cream sitting on a table can hold its shape, unlike a liquid spreading out into a puddle; but if you push it on your hand, the pile flows and will not reserve back to its original shape, which process is more like liquid. Other soft materials are similar to this character of shaving cream: by applying stress, the material can transit from solid-like to liquid-like properties. The definition of a jammed material is an amorphous solid. It means that it is structurally disordered, and possesses a yield stress. There are other parameters we can tune to achieve jamming transition. One important idea of jamming transition is that different control parameters for various soft materials can be unified by one phase diagram [6]. As shown in Fig. 1.1(a), A. J. Liu and S. R. Nagel introduced a jamming phase diagram to propose an analogy between these three control parameters: temperature, packing density and load (or stress). The states which lie within the curved surface, close to the origin, are jammed states. By raising up temperature, reducing volume fraction or applying shear stress, the materials can transit from jammed state to unjammed state. However, this diagram has

been modified by considering different types of interactions like attractive or repulsive particles [7]. As shown in Fig. 1.1(b), the surface of the bubble, as an indication of where the transition happens, has different curvature from the original jamming phase diagram. They also revised the diagram by replacing temperature T with k_BT/U, where U is the depth of potential well for attractive particles [7]. The continuity of the surface in Fig. 1.1 that indicates the jamming transition implies that there is a universal jamming transition and a universal jammed state, with perhaps differences that vary smoothly as a function of the parameters.

Therefore, granular systems, bubbles, droplets, etc., of which the sizes are large enough that thermal fluctuations can be ignored because it is too small comparing to the large gravitational energy of each particle or potential energy between particles. They are the typical model systems used to investigate the jamming behavior in the plane of zero temperature $T \approx 0$, shown as the blue planes in both plots in Fig. 1.1. This is because only density and external stress can drive the system to explore phase space in this limit. One advantage of using these model systems with this limit to study jamming is that we can eliminate the temperature by treating it as $T = 0$ to reduce the complexity [8]. In this plane, there are some possible mapping from stress related variables to temperature [9–11]. If so, many thermal physics might be generalized to apply in and describe stress driven systems. Also, due to the wide availability of the practical materials in this plane (the blue plane in Fig. 1.1), study jamming transition using these materials can help us to obtain valuable information related to many other systems. The two control parameters at $T = 0$ are inverse density and load, or packing fraction and external stress, specifically for particles.

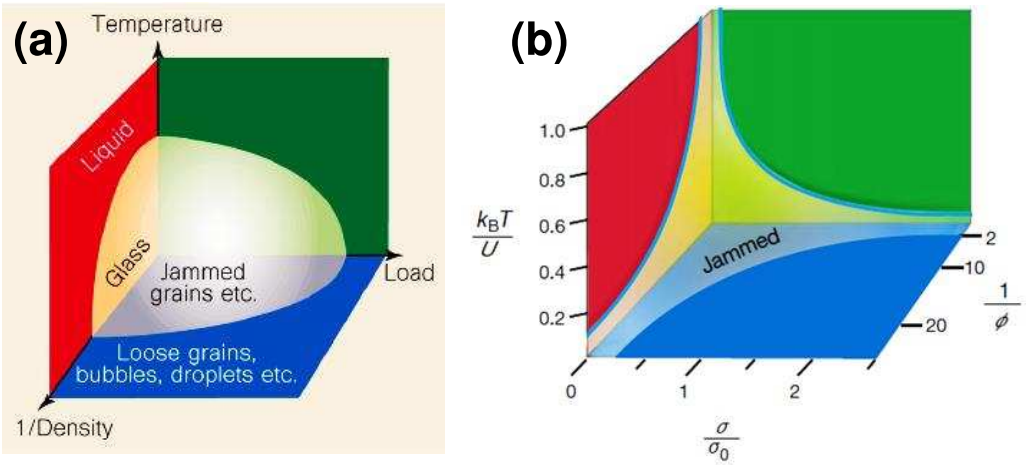

Figure 1.1: Jamming phase diagrams. (a) The three control parameters are temperature, 1/density, and applied load. The states which lie within the curved surface, close to the origin, are jammed states. The red plane formed by temperature and 1/density is the regular glass transition, where the inverse density represents the influence of the more normal glass transition parameter pressure. As temperature increase or density gets smaller, it becomes liquid. For grains, bubbles, droplets, etc, the inverse density is equivalent to inverse volume fraction, or inverse area fraction if 2D. If the load is above the yield stress, the materials unjam and flow like liquids. Crossing the jamming transition surface means the material transiting from unjammed state to jammed state, or vice versa.(b) Jamming phase diagram for attractive particles. The control parameters are the ratio between thermal energy k_BT and potential energy U due to the attraction interaction between particles: k_BT/U, inverse density: $1/\phi$ and stress σ/σ_0. It is the same that athermal system like grains, bubbles, droplets, etc sit on the blue plane formed by inverse density and applied load. (Thanks to Nature Publishing Group's permission. (a) Reprinted by permission from Macmillan Publishers Ltd: Nature ([6]), copyright (1998). License Number: 3817291391827. (b) Reprinted by permission from Macmillan Publishers Ltd: Nature [7], copyright (2001). License Number: 3817301180058.)

The critical point where the jamming transition occurs is defined as jamming point with yield stress $\sigma = \sigma_0$ or with packing fraction $\phi = \phi_J$ when there is no external stress. The $\phi_J \sim 0.84$ is the area fraction in 2D and $\phi_J \sim 0.64$ for 3D in binary systems. ϕ_J slightly varies in different samples, or even depends on the route to the jamming point [12]. However, the kinetic and dynamic response of these model systems are thought to only depend on the distance to the jamming point $\phi - \phi_J$. This is because of the critical-like scaling that people observed in soft materials analogous to a classical phase transition regardless of dimensionality and force law. There are numerous experimental and numerical study explored on the critical scaling laws and found the universal scaling with distance to jamming [13–22].

However, the origin of this universal dependence is still unclear [8, 23]. By studying more details on the dynamic responses of soft materials at different distance to the jamming point would provide new insights to help us better understand what is happening near jamming transition. More specifically, in the model system that I use for this dissertation, quasi-two-dimensional emulsion, the main two control parameters are area fraction and shear stress. The area fraction is controlled by different packings of condensed or dilute droplets. The novel idea is on the axis of applied load. We apply shear by flowing them using different approaches. The response of our emulsion system to external stresses consist of two types of responses. One is a liquid-like viscous response: dissipating energy by flowing. The other one is solid-like response: storing energy by internal elastic deformations and dissipating energy by plastic events of local rearrangements. The results show some interesting dependence of the dynamics of emulsion on area fraction ϕ, which is that the velocity fluctuation

is greater when the system is further above jamming point. This is unexpected because typically one associates dynamic heterogeneity at lower area fractions closer to jamming point [14, 24–31]. This contradictory observation might provide a different perspective on understanding jamming transition. More details in Chap. 6.

1.2 Flow of Soft Materials

Two dimensional jamming phenomena could be easily found in our daily lives like traffic jams of automobiles in a city and also in industry like the transports of cans and bottles in factories. They all involve the flowing of objects. In experimental models, usually flow is imposed by applying external stress. Different from simple fluid, soft materials have granularity and yield stress. They often show a mix of solid-like (like jammed in disordered state) and liquid-like behavior, when the shear stress is above a critical yield stress. The mixture leads to large fluctuations of local strain and stress in space [32–39]. Microscopically, it is due to the disordered spatial configurations consist of local groups of particles that are temporally jammed. During flow, the stress build to a critical point and the local groups of particles can unjam. This spatially inhomogeneous flow is composed of these local jamming and unjamming processes. During slow steady state flow, where the strain rate and shear stress can have well defined long time averages, which can be considered as the cumulative effect of those jamming and unjamming local events. In many cases, the flow behavior can be captured by the archetypal Herschel-Bulkley constitutive relation:

$$\sigma = \sigma_Y + A\dot{\gamma}^n, \tag{1.1}$$

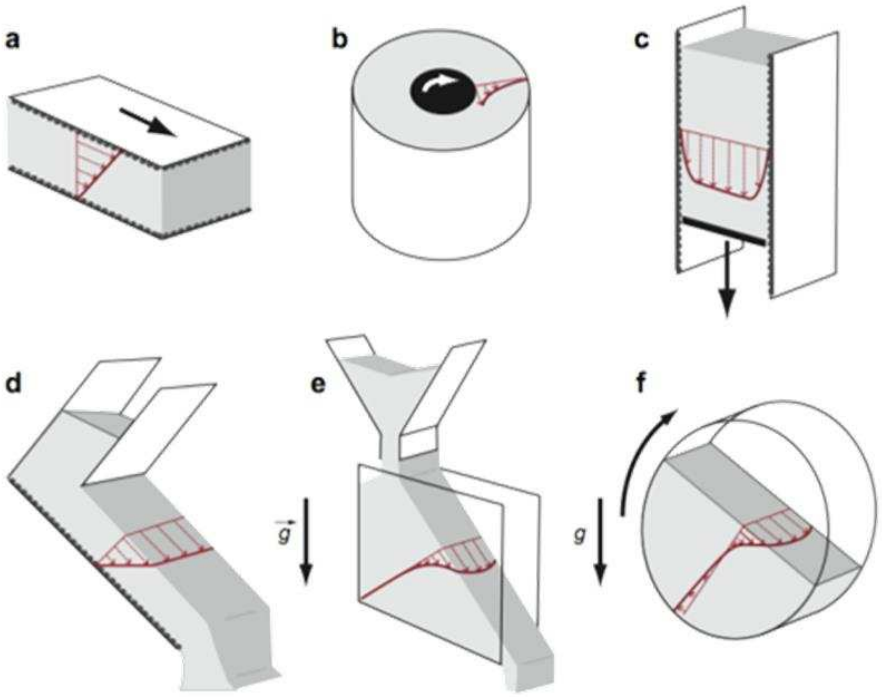

Figure 1.2: Six common granular flow geometries [40]. Gray areas indicate grains and red arrows indicate resulting strain. (a) plane shear, (b) annular shear, (c) vertical-chute, (d) inclined plane, (e) heap, (f) rotating drum.(Reprint permission is not required for a thesis/dissertation.)

where σ_Y denotes a yield stress, A is the consistency, and n is a power-law index. For simple fluid, $\sigma_Y = 0$ and $n = 1$.

The geometries for study the flow of soft materials has a large variety to create different stress fields. Take typical geometries in granular studies for example, Fig. 1.2 shows six different flow geometries including plane shear, annular shear, vertical-chute, inclined plane, heap, and rotating drum. The gray areas in the figure indicate the grains and the red arrows indicate the strain of grains. Typically the stress is due to gravity or an external device and the resulting strain is measured. This is similar with the approach that I use for the study in emulsion in this dissertation.

Though a lot of recent work has been done describing the flow properties in these different geometries, extracting common features is still difficult. In the flow of soft materials, the velocity and stress profiles usually can be described using a exponential or power-law decay with distance from boundary [41, 42]. Usually, this decay has a length scale of 5-15 particle diameters and the flow is localized in the narrow region, which is known as *shear banding* or shear localization [41, 43]. This localization phenomena exist in various soft materials including granular material, colloidal suspension, foam and emulsion [41, 44]. Take 2D foam as an example, previous study on flowing them using external shear stress in different geometries, as shown in Fig. 1.3, help us better understand shear banding. No shear banding is observed in Couette experiment using bubble raft [45, 46]. The side view of this configuration is shown in Fig. 1.3(a). Strong localization is observed in both liquid glass geometry, as shown in Fig. 1.3(b) [46, 47] and in Hele-Shaw cell, as shown in Fig. 1.3(c) [48]. They also find that the shear-banded velocity profiles has dependence on the shear rate. Based on the different response in these geometries, shear bands in this 2D foam system result either from stress inhomogeneities or drag forces from the confining glass plates. However, we do not see shear banding in my flow of emulsion.

1.2.1 Emulsion

Emulsion is a type of soft material consisting of droplets of one liquid dispersed into another immiscible liquid. There are basically two types of emulsion, water droplets in oil and oil droplets in water. In order to prevent coalescence, which is when two droplets merge together to form one single droplet, surfactant molecules

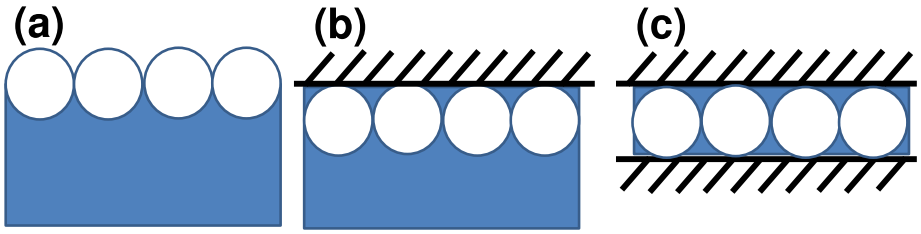

Figure 1.3: Side views of typical geometries for flow of 2D foam. White circles are air bubbles, blue region is water and black segments indicate solid boundary. (a) bubble raft, (b) liquid glass, (c) Hele-Shaw cell.

are necessary to stabilize the droplets. Surfactant molecules have both hydrophilic head that prefers to stay with water phase and hydrophobic tail that prefers oil phase. As examples, a cross-section of a confocal microscope image of a 3D emulsion is shown in Fig. 1.4 and a sketch of an emulsion droplet with surfactant molecules is shown in Fig. 1.5. With well developed microfluidic technique (more details in Sec. 2.2), making emulsion is quite easy and controllable, especially compared to making colloids. Existing techniques can precisely control the sizes of the droplets in a wide range from micrometers to millimeters, the packing fraction with almost the whole range from 0 to 1, and the interactions between droplets by using different surfactant. The surfactant that we use in this dissertation is Fairy soap (more details in Sec. 2.2).

The droplets in an emulsion stay like a spherical shape because of surface tension. Spherical shape can minimize surface area so that it minimizes surface energy, which is the product of surface tension and surface area. When they start to pack together, droplets contact each other and make each other deformed. Based on the features extracted from imaging them, a technique has been developed in our lab to measure

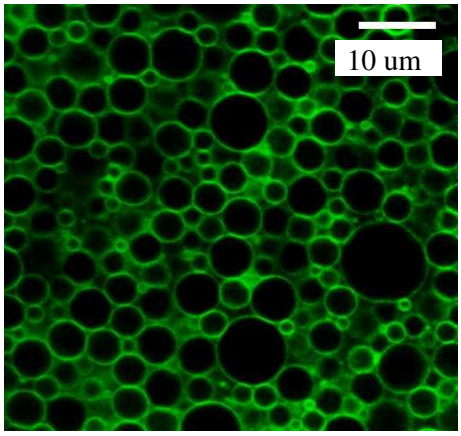

Figure 1.4: Confocal microscope image of an emulsion. The droplets (dark) are dodecane, a transparent oil. The space between the droplets is filled with a mixture of water and glycerol, designed to match the index of refraction of the dodecane droplets. The droplets are outlined with a fluorescent surfactant. The hazy green patches are free surfactant in solution, or else the tops or bottoms of other droplets. (Picture taken by ER Weeks and C Hollinger.)

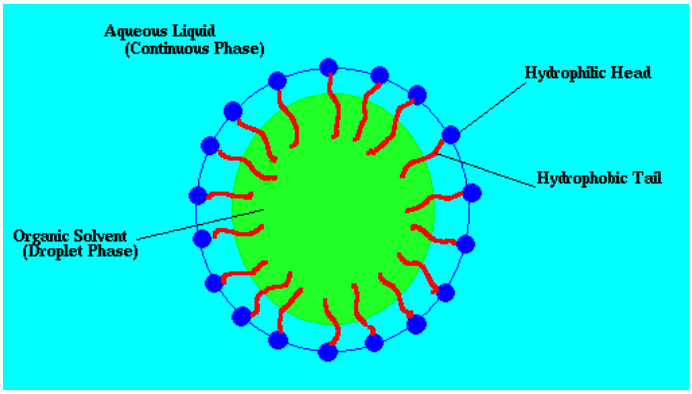

Figure 1.5: Sketch of an emulsion droplet. Not to scale: typically the surfactants are tiny molecules, whereas the droplet is micron-sized. (Sketch by C Hollinger.)

the repulsion forces between droplets [14] (more details in Sec. 3.4). The droplets are interacting via nonlinear normal forces and viscous forces. There is a slight adhesion between oil droplets but no static friction between oil droplets in our system [14]. These are some of the main differences of emulsion from granular materials. Another difference is that grains are hard particles while emulsion is largely deformable, which makes our force measurement technique feasible based on image information alone. Since surfactant can lower the surface energy, it makes this difference even more dramatic that oil droplets are very "soft". This can introduce another degree of comparison on softness between different model systems to study the dynamics of soft materials. Each model system has its most well-known feature: foams and emulsions are viscous and deformable, colloidal suspensions are Brownian, and granular media are frictional. For the similar model systems, foam and emulsion, while they share various common features, there are some nuances between them. These can include but not limited to the strength of adhesion between bubbles, the viscous drag force between bubbles and between bubble and glass slides, compressibility of bubbles, different surface tension, coarsening effect in bubbles, etc. Overall emulsion is a great and inexpensive candidate as an experimental model to study the flow property of soft material due to many of its unique characteristics. The features most relevant to this dissertation is the lack of static friction between droplets and the deformability of droplets.

1.2.2 Flow of Emulsion

The side view of the geometry that I use for this dissertation, as shown in Fig. 2.8, is very similar to the Hele-Shaw cell shown in Fig. 1.3(c). But it has a bit more complexity in another dimension (in the plane) with a constricting hopper shape as described in Chap. 4 and Chap. 5. Hopper is a popular geometry for studying the flow of soft materials because of not only its simplicity but also its wide application in industry like the funnel-shaped concrete mixer and the funnel on production line in food or pharmaceutical industry. With the hopper chamber, I use two different approaches to drive the hopper flow including gravity and constant flux rate pumping.

In granular hopper flow, the mean flow rate is a function of the difference of the opening size to the critical size for clogging, a result often attributed to Beverloo [49–51]. In other words, the flow is influenced by the possibility of clogging even when the hopper opening size is larger than the critical size mentioned above. For example, the flow rate would have fluctuations for the sand flow [52–54] and this is what I observed with emulsion flow as well. To better understand the flow properties in the hopper geometry when the opening size is around critical size, it is crucial to understand what happens when hoppers clog and the corresponding hopper opening size for clogging and the clogging probability. The clogging process in hard 2D disks hopper flow is known to be due to arch formation near the hopper exit [1, 53, 55]. The static friction between particles is critically important in the studies of the dynamics of granular materials. For example, with bigger friction coefficient, the flow gets easier to be clogged at the opening. Using oil droplets would remove the effect of static friction but introduce softness into the system. Referring back to the jamming idea

in Sec. 1.1, we define clogging in hopper flow in our system as that when droplets stop flowing and clog the hopper exit (more details in Chap. 4). And, we observed clogging in frictionless system as well. The critical size for clogging is much smaller though and no observation of long arch formation at the hopper exit. With more simulation work done by Eric Weeks, we rule out the necessity of the existence of static friction for clogging and discover the crucial impact of deformability on the clogging via arch formation [56]. This greatly help us understand the clogging process in hopper flow.

There are various versions of models for simulating the flow of soft materials. One popular model in foam was introduced in 1995 by Durian [13], referred as "bubble model". In this model, bubbles are represented by soft spherical particles interacting only when they are in contact. When they contact each other, there are elastic forces as a function of their overlap and viscous forces as a function of the velocity difference between bubbles sliding pass each other. This model and its further revised versions work well in explaining foam dynamics [57]. Since foam and emulsion share a lot of common features including athermal system, large deformability, lack of friction, easy to achieve quasi-2D system, etc., bubble model could be a great model to describe our emulsion system and Eric's simulation work is using a model based on it. In the perspective of describing the dynamics of soft materials using theoretical models, our experiment provides a great use case to better understand the physical principles that govern the flow behavior of soft materials, particularly soft particles with large deformability.

Another broadly studied flow behavior observed in soft material is the intermittent flow with long still periods punctuated by rapid avalanches [35, 58–61]. The power-law

scaling is largely used for measuring the dynamics and kinetics in the avalanche flow in many soft materials system [36, 55, 58, 60, 62–77]. For granular materials, the static friction can prevent the flowing and lead to avalanche. However, in emulsion there is no static friction and we still see avalanche in the quasi-2D hopper flow driving with constant flux rate pumping (details in Chap. 5). Unlike the static friction in granular material, the stress in emulsion is supported by surface tension, which resists the deformation of droplets. This is demonstrating that the physics governing avalanche in these two systems could be fundamentally different.

Microscopically, one important feature of the flow of soft materials is its plastic deformation. This could be considered as one type of the jamming and unjamming events mentioned above. For materials with granularity, the constituent particles like grains, bubbles and droplets have such plastic deformation in the form of rearrangements widely observed [19, 36, 45, 46, 60, 70, 78, 79]. The complex rearrangements of the internal structure is a direct observation of the interval stress at a microscopic level and thus provide rich information for us to understand the interactions between particles. The rearrangements are not strictly local but deform their neighborhood over a certain finite range [80]. A well-studied case of the rearrangements and also the most fundamental topological change is called T1 event, which is a group of four droplets exchange neighbors. As shown in Fig. 1.6, two dark blue droplets as the nearest neighbors move apart and the two light blue droplets as the next-nearest neighbors move together and become nearest neighbors. Previous study in our lab has been experimentally explored the local stress field redistribution around T1 event [24].

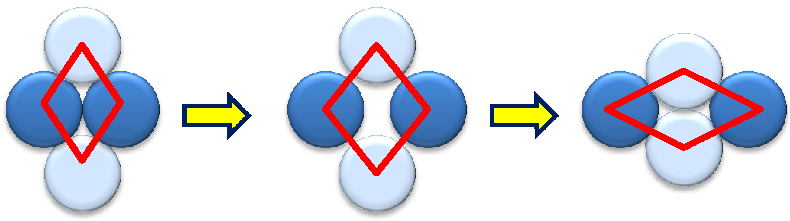

Figure 1.6: Schema of a T1 event involving a group of four droplets. Two dark blue droplets as the nearest neighbors move apart and the light blue droplets as the next-nearest neighbors move together and become nearest neighbors. The red lines connect the centers of droplets, from which we can see the deformation of the diamond formed by the red lines.

The most exciting observation is that we can have both smooth flow and intermittent flow in the same experiment by controlling strain rate. The transition from smooth flow to avalanche is happening while strain rates get bigger. The transition is fairly smooth but around the time scale that has the same order of magnitude of the time scale of T1 event (mentioned above). This is distinctively different from granular avalanches. In granular experiment, the most common cases of avalanches are due to stick-slip events where static friction plays a critical role. In emulsion, we do not even have static friction. The match between the transition time scale for two distinct flow behavior and the time scale for local rearrangement events provides the implication that the internal structural relaxation is the dominant controlling factor that affect the flow behavior of jammed emulsion. Essentially it is saying that the energy dissipation mechanism is different in frictionless system from that in granular material. This is adding a new perspective into the existing understanding of avalanche flow behavior of soft materials.

Chapter 2

Experimental Apparatus and Procedures

Our samples are oil-in-water emulsions prepared by a standard co-flow microfluidic technique [81]. We load droplets into chambers made with glass slides and some spacer material. Then we use gravity or syringe pump to drive the flow of droplets. The dynamics are recorded by using microscope and camera. This chapter describes the details of the experimental devices and approaches.

2.1 Making Microfluidic Device

The main steps of making a co-flow microfluidic device (version one) includes: (1) Make micro-pipette by pulling borosilicate glass tubes using pipette puller. Burn and break the tip to make a smooth and flat tip with specific size. The tip inner diameter ranges from 20 to 80 μm. The catalog number of the glass tubes could be

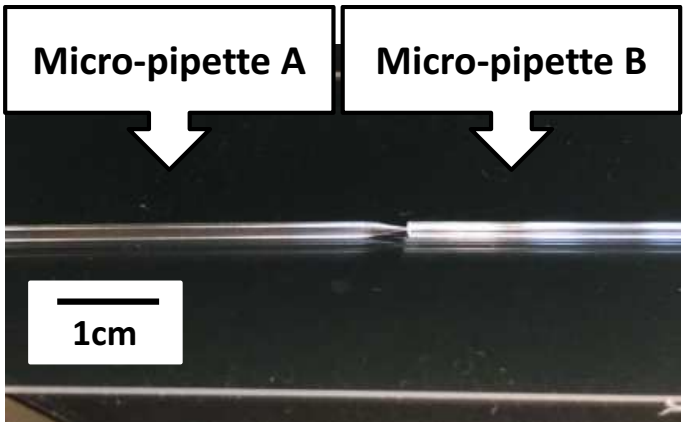

Figure 2.1: Photograph of two micro-pipettes. Micro-pipette A is inserted into micro-pipette B.

Sutter Instrument B100-75-10 (meaning of parameters: outside diameter 1.00mm, inside diameter 0.75mm, and length 10cm), B100-50-10, B150-86-10 or B100-30-7.5HP. The pipette puller setting parameters for future experimenter's reference: unlocked, P=500, 0, 1, HEAT=575, PULL=75, VEL=100, TIME=100.

(2) Break the floppy tip of the micro-pipette into the size you need. The inner diameter of the tip we commonly use is $20 \sim 80\mu$m. Using scoring tile to break is simple and easy but have less precise control on the size. Another approach is using a glass burner to get more accurate tip size under microscope.

(3) Insert the tip of micro-pipette into another glass tube and fix them on a glass slide using epoxy. Make sure the tip is at the center and inside the other glass tube under microscope. Photograph is shown in Fig. 2.1. Micro-pipette A is inserted into micro-pipette B. (4) Cut grooves on the bottom of two needles as shown in Fig. 2.2(a). The size of the grooves should be as small as possible but big enough to fit the outer diameter of glass tubes. Needle parameters: Stainless Steel, 26 Gauge, Length 0.5",

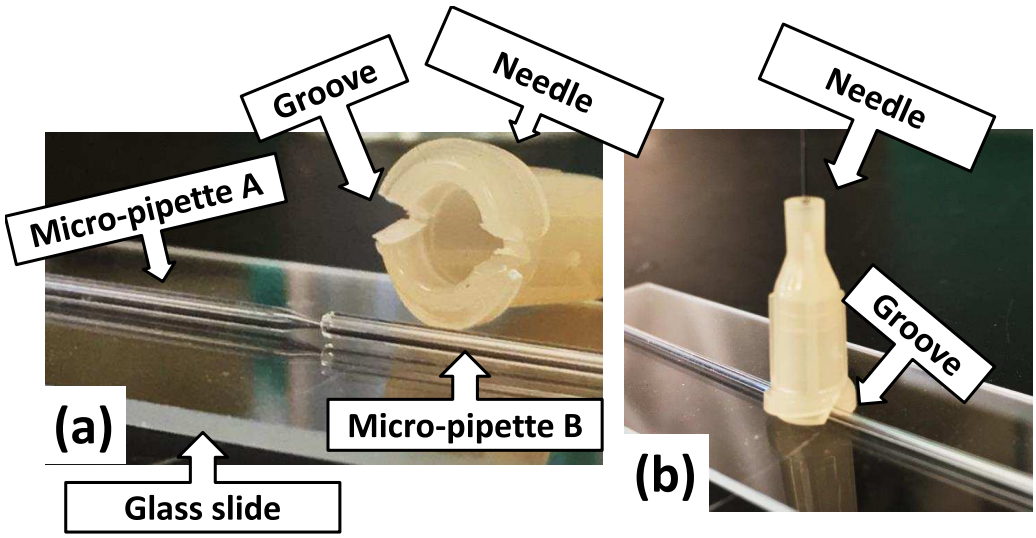

Figure 2.2: Photograph of (a) cutting grooves on the bottom of needles to fit glass tubes, and (b) placing the needle on top of the junction, where micro-pipette A is inserted into micro-pipette B.

Inner diameter 0.011" and Outer diameter 0.019", Jensen Global Part#: 651-128

(5) Place one needle on the junction near the micro-pipette tip, which is for water flow, as shown in Fig. 2.2(b). And, place the other needle on the other end of the pipette with the tip, which is for oil flow. Then, apply 2 Ton epoxy to fix the two needles (Devcon 14310 Clear 2 Ton Medium Cure Water-Resistant Adhesive Epoxy). Let the device stay overnight to maximize the epoxy strength. There are two versions of microfluidic devices as shown in Fig. 2.3. The main reason is that the first version usually has leaking issue over time. This is due to the high pressure built up at the small tip of the micro-pipette during the production of droplets (more details about the mechanism is in Sec. 2.2). The version two has one more step on the basis of version one:

(6) Place a hollow cylinder outside the needle (the one for oil flow) and fill up the

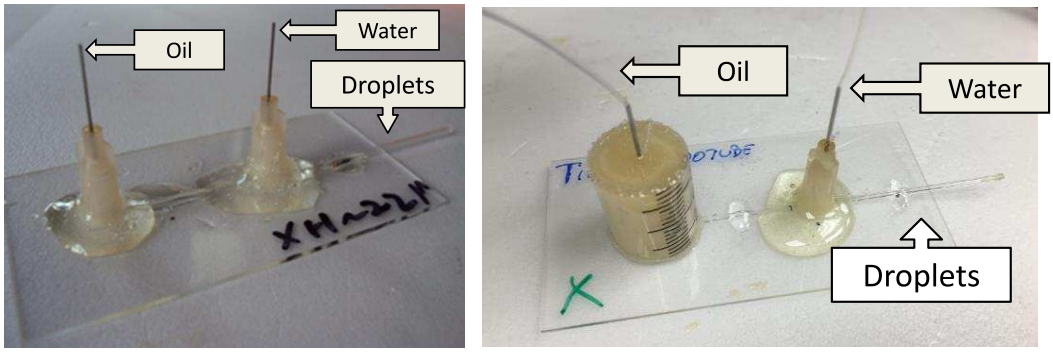

Figure 2.3: Photograph of microfluidic devices. (a) version one; (b) version two.

cylinder with 2 Ton epoxy that are pre-mixed for 8 min. This is shown at the left side of Fig. 2.3(b). The cylinder in the photograph is a portion of a plastic syringe, where the tick marks are still on the surface. The strength of the adhesion in this version is sufficient to bear the high pressure on the side of oil flow. This improvement in design is credited to Carlos Orellana.

We keep using this design of microfluidic device due to its simplicity and robustness for producing emulsion given the requirements for our study. Mainly we need droplet size around couple hundred micrometers and the amount of droplets we need can be produced up to 2 hours. For different size, smaller droplets for example, and higher throughput, there are other options. Polydimethylsiloxane (PDMS) microchannels using glass-etching or soft-lithography is a popular technique to fabricate microfluidic devices [82–85]. The advantages of PDMS-based chips include the fastness of manufacture by means of soft-lithography, the consistency in construction since it is fabricated in mold, the high throughput of emulsion production since multiple channels can be molded in one chip [86]. However, fabrication of microfluidic

devices is difficult and the chemical robustness is poor. The softness of the PDMS microchannels lead to some difficulty in photolithographically patterning their surface properties, although some surface treatment technique has been developed [82]. Specifically for our experiment using oil, PDMS-based micro-channels without surface treatment using chemicals has disadvantage. For example, silicon oil can swell PDMS [83].

2.2 Making Droplets

Our emulsion samples are oil droplets in water, stabilized by a surfactant [14]. The three main types of primary material to make oil-in-water emulsion is oil, distilled water and surfactant. The options for the oil include mineral oil (Fisher Scientific O121-1, density $\rho_{\text{mineral oil}} = 0.83$ g/mL, viscosity $\eta_{\text{mineral oil}} \approx 69$ mPa $\cdot$ s) and silicon oil (Fisher Scientific S159-500, density $\rho_{\text{silicon oil}} = 0.96$ g/mL, viscosity $\eta_{\text{silicon oil}} \approx 69$ mPa $\cdot$ s; Brookfield 10cps or Brookfield 100cps). Several types of surfactant have been tried including sodium dodecyl sulfate (SDS), different types of detergent (Dawn is a molecular surfactant and Fairy is a polymer surfactant), and human serum albumin (HSA). HSA is an exception since it is for water-in-oil emulsion. Mineral oil has bigger density difference with water than silicon oil, which make it as a better candidate for the hopper clogging experiment described in Chap. 4 in terms of the droplets running speed. Not like many organic liquids, another reason for choosing mineral oil is that it is not harmful since we do not place the microscope and pumping system in a fume hood and some of the chambers are simply open to the atmosphere. Note that different surfactant could change the properties of droplets

including its stability, deformability due to different surface tension and possibly the adhesion and viscous drag between droplets. Fairy soap is a type of polymeric surfactant commonly used in Britain. The big size of the molecule might be the reason for its efficiency in stabilizing oil droplets. For consistency, I use the same materials to make droplets. So, the final recipe for my studies in Chap. 5 and Chap. 6 are the same including mineral oil, distilled water and Fairy dish-washing detergent. The detergent is added at mass fraction 0.025 as the surfactant to prevent coalescence of the droplets. This is the also the same recipe as that has been used in previous work [14, 87].

After the mixing of distilled water and Fairy soap is done and the microfluidic device is ready, we can insert each needle into a plastic tube. As shown in Fig. 2.4, one of the needles is attached to a 1mL syringe (BD 309628) for oil pump and the other one to a 60mL syringe(BD 309653) for water pump using PTFE tubes (Light Wall, 28 Gauge, Inner diameter is $\approx$ 0.38mm, Component Supply Co. Part#: /STT-28-C).

Two syringe pumps create the co-flow in the microfluidic device. KD Scientific Model 200 is for water pump and Chemyx Inc.Model: Fusion 100 for oil pump. The former one is for big syringe that can produce large flow rate. This is good for water flow since we need the water flow to be fast enough to create the shear at the micro-pipette tip to break off the droplets. The latter syringe pump is good at precision and it fits small syringe. So, this is good for oil flow because we need to produce small droplets and the tip of the micro-pipette needs to be small, which creates high pressure if we pump oil too fast. Another reason we use this syringe pump for oil flow is that we need the oil droplets size to be uniform and the precision

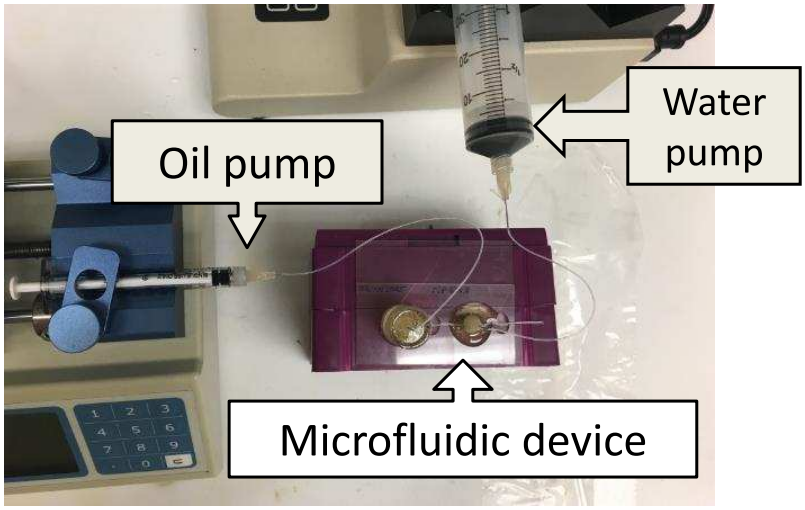

Figure 2.4: Photograph of apparatus for making droplets including microfluidic device and pumping system to pump water flow and oil flow through two syringe pumps.

of the pumping is important for the stable droplet growth. Most importantly, the oil flow need to be slow enough that a jet does not develop [88], which might cause turbulence and droplet size is not uniform. In this technique, mineral oil is injected into a flowing stream of distilled water and surfactant, as shown in Fig. 2.5. The flow rate of the water Fairy soap mixture is $0.1 - 2$ mL/min and the flow rate of the oil is $0.1 - 0.5$ mL/hr depending on the tip size and the inner diameter of the outer tube (typically 500 μm). In Fig. 2.5, top figure is the schema showing the co-flow details and the bottom image is a photograph of a real co-flow microfluidic device with an oil droplet forming at the pipette tip. Once the two flow rates are steady, this microfluidic technique produces droplets of a desired size with $\sim 3\%$ polydispersity (standard deviation divided by mean). We control the size of the droplets by varying the flow rates of the oil and water in the microfluidic device. Given the range of flow rates mentioned above, typically we can produce droplets with diameter in the

range of $80 - 380$ μm. However, it is not straightforward to predict the size of the droplets based on the two flow rates. So, I need to calibrate the relation between flow rates and droplet sizes for each microfluidic device. Given the dimension of the microfluidic device and the flow rates that I tried, one observation that might help for future experimenter to repeat is as follows: (1) smaller pipette tip size usually gives smaller droplets; (2) when the oil flow rate is low enough, the droplet size is more dependent on the water flow rate: faster water flow gives smaller droplets [88]; (3) when the oil flow rate is high enough, the droplet size is more dependent on the oil flow rate: this might reach the jetting regime [88].

More experimental and theoretical work has been done related to this technique [82, 86, 89–91]. More advanced techniques exist including producing double emulsions: multiple oil droplets in another droplet[81] or a small water droplet in a bigger oil droplet [84], producing very small droplets with stable size in the order of $0.1 - 1$ μm [83], and using surface acoustic wave to direct the motion of droplets in microfluidic channels [85].

In order to get high concentration of oil droplets, I use the method as shown in Fig. 2.6. The glass pipette is placed inside a vial. Since oil droplets are lighter than water, they will be trapped inside the pipette floating on top of the water, shown as the white area in the figure. Water is flowing to the bottom and coming out of the pipette and fills the glass vial. Since water flow is much faster than the oil flow, there is much more water coming out from the microfluidic device. However, in this way we can trap all the oil droplets and get condensed sample using gravity.

In some cases we mix together two batches of droplets with different sizes to make

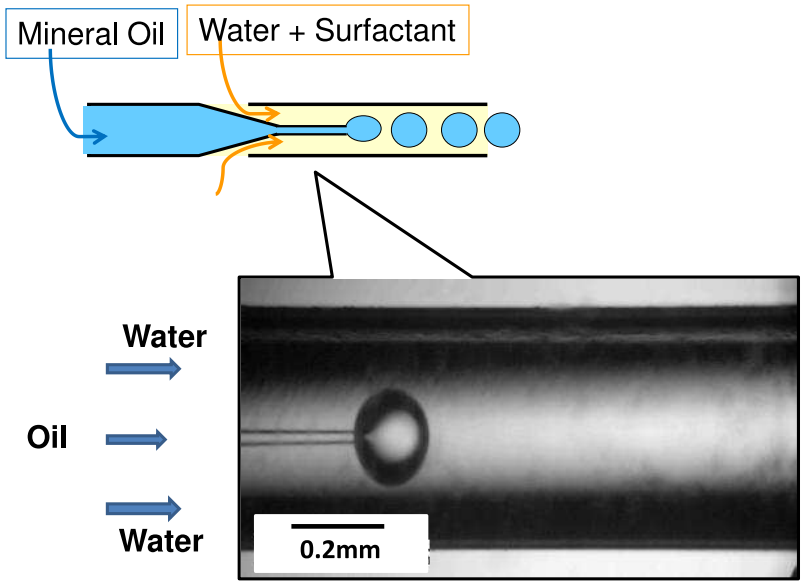

Figure 2.5: Top: Schema of the co-flow technique. Mineral oil (shown in blue) is flowing inside the micro-pipette and water with surfactant (shown in light yellow) is flowing outside the micro-pipette but inside another glass tube. The shearing on the micro-pipette tip can pinch the droplets off the tip. Bottom: Photograph of the co-flow details of a real microfluidic device (credit to Kenneth Desmond and James Sebel). The tip size of the micro-pipette is about 30 μm and the inner diameter of the outer glass tube is 0.38 mm. An oil droplet is forming at the micro-pipette tip.

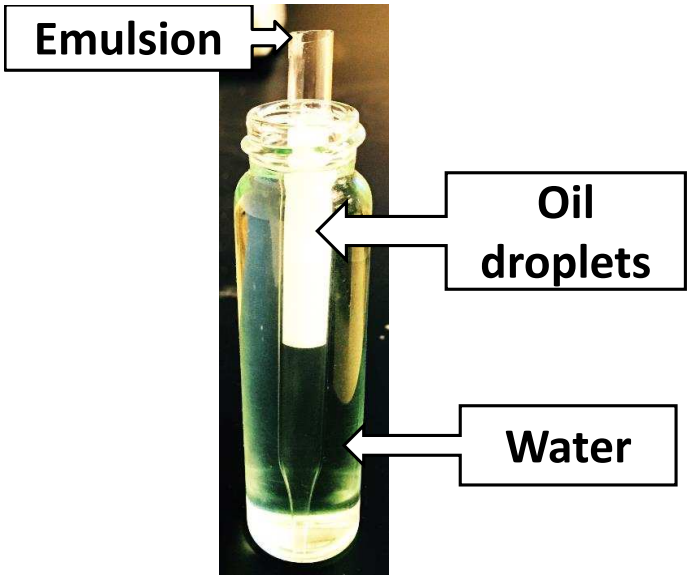

Figure 2.6: Photograph of apparatus collecting droplets. The glass pipette is placed inside the vial. Emulsion produced by microfluidic device is flowing into the glass pipette. The white region in glass pipette are condensed oil droplets and other area in the glass vial is filled with water with surfactant.

disorder samples. For example, a bidisperse sample made with two different sizes at size ratio 1.4 can prevent crystallization effectively. One way is to use the same vial to collect droplets. The water flow during the droplets production can mix the sample very well.

2.3 Making Chambers and Loading Samples

The chamber consists of two microscope glass slides of dimensions 25 mm $\times$ 75 mm (Corning) separated by some spacer material. For spacers, some of the chambers in Chap. 4 use double sided tape ($\approx$ 100 μm thickness) and others use parafilm ($\approx$ 130 μm thickness) because both double sided tape and parafilm do no require epoxy to seal the chamber. But both of them can swell and change the shape of the chamber over time. The rest of the work all use transparency film (100 μm thickness) as the spacer material, which requires very precise control on the amount of epoxy applied to seal the chamber but helps the chamber last longer. These pieces of film act as spacers and thus creating a gap between the slides. The gap thickness is a little larger than the film thickness due to the epoxy between films and slides. Fig. 2.7 shows the basic construction of the chambers. More specific details will be described in each chapter. For example, in Chap. 4 there are multiple hopper chambers in one slide; in Chap. 5 a syringe needs to be connected to the chamber via PTFE tube and the chamber is sealed with UV epoxy (Thorlabs NOA68) on the syringe side; in Chap. 6, a glass pipette is inserted into the sample for injecting an inflating oil droplet with a syringe pump. Note that the difficult part is to apply the right amount of epoxy (Thorlabs NOA81) to adhere the transparency film with the glass slides. It

is important since the epoxy could change the geometry of the chamber. If too much epoxy is applied, it will flow out of the edge of the pieces of film and the chamber gets narrower than designed. If the amount of epoxy is not sufficient, the region that is lack of epoxy can create some tiny space between film and glass slide. This space will be filled with water or oil droplets, which will change the boundary condition of the chamber that we cannot control.

In all my studies in this dissertation, I need to make the gap thickness as uniform as possible for each sample chamber. We need try our best to apply a uniform layer of epoxy. The approach to accurately measure gap thickness is using differential interference contrast microscopy (DIC). I use microscope (Leica DM IRB) with 63× objective lens (air, working distance ≈ 1 mm). The main steps include:

(1) Set up Kohler illumination to get a uniform bright field.

(2) Keep the brightness of illumination as low as possible so we can see tiny dust of the surface of the glass slides.

(3) Use high magnification lens so the focal plane is thin and thus the measurement is more accurate.

(4) Adjust the condenser to achieve small depth of focal plane balanced with the contrast for a good image quality.

(5) Use a glass slide with pre-known thickness to calibrate the fine focus knob on the microscope because different magnification settings would give different scales for the fine focus knob. While we turning the fine focus knob, its change is corresponding to the change apparent depth. However, the change in real depth, which is the true thickness of the gap that we want to measure, also depends on the index of refraction

of the medium in the chamber gap. The scale that I calibrated for the given setting is 2 μm per tick mark on the fine focus knob, which is a $360/100 = 3.6°$ turn of the knob. So, the gap thickness = number of ticks $\times 2$ μm $\times$ n, where n is the index of fraction in the chamber ($n_{air} = 1$ and $n_{mineral\ oil} = 1.4735$)
The measurement uncertainty is up to 1 tick ≈ 2 μm. The variation of gap thickness is very small within a small region. For example, the chamber in the study in Chap. 6 has this variation less than 1%.

Another approach to construct chambers has been tried using PDMS. The simple fabrication without chemical treatment is done at Hang Lu's lab Georgia Institute of Technology. The chamber is used in the study of pumping emulsion through a hopper, described in Chap. 5. However, the surface property is not suitable for our study and the treatment is not straightforward as mentioned in Sec. 2.1. Another reason I do not use PDMS for this study is the softness of PDMS. The relatively low modulus of PDMS comparing to glass slides under high pressure can bring more compliance in the system, which is better to minimize to study avalanche due to pressure build up. More explanation will be in Chap. 5.

Our sample chamber is designed to create a system of quasi-2D frictionless emulsion droplets, analogous to 2D granular systems of photoelastic disks but without static friction [92]. So, we fill the chamber with emulsion where the diameters of the oil droplets are larger than the gap distance between the microscope slides. Fig. 2.8 is the schema of chamber side view, where the droplets are sandwiched between two parallel pieces of glass and are thus deformed into pancake-like disks. In the study described in Chap. 5 and Chap. 6, packing fraction ϕ is one of the control parame-

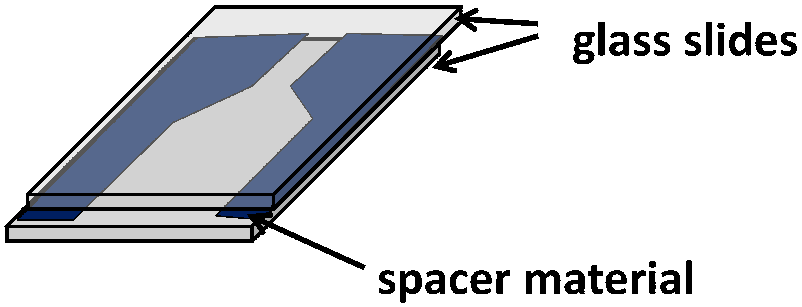

Figure 2.7: Sketch of basic structure of chambers. Two microscope glass slides are separated by spacer material. The shape of the pieces of spacer material determine the geometry of the created chamber.

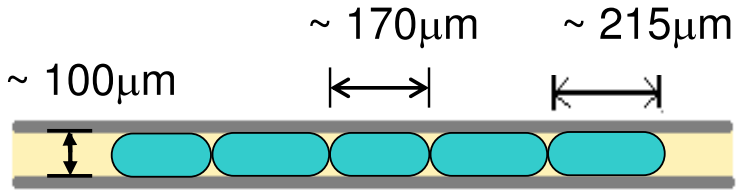

Figure 2.8: Schema of side view of the chamber and sample. Droplets (shown in blue) are squeezed between two glass slides to achieve quasi-2D system. The gap thickness is typically about 100 μm. The schema shows bidisperse sample with two typical diameters of droplets 170 μm and 215 μm.

ters. ϕ can be somewhat controlled by preparing bulk emulsion samples at different 3D volume fractions and loading the sample at a higher or lower concentration.

2.4 Pumping and Imaging

After the sample chambers are loaded, they are placed on a microscope for imaging during pumping. In Chap. 5, I use 1mL syringe (BD 309628) to achieve flux rate between 0.0001 and 0.02 mL/hr. In Chap. 6, I use Hamilton glass syringe 25 μL (model 1702 RN SYR) in order to have extremely low flux rate 5 μL/hr (more details

in Sec. 6.2.1). Both studies use syringe pump Chemyx Inc.Model: Fusion 100.

In Chap. 5 and Chap. 6, to acquire accurate measurements of each droplets' dynamics and deformation, balanced with a reasonable frame rate, I take images with resolution 2000 × 1800 pixels using a Mightex 5MP monochrome CMOS camera (M/N: BCE-B050-U) at frame rate range from 0.2 to 4 images/second. The frame rate is picked to meet the following requirements. It needs to be slow enough so taking a long movie does not create too big file in the computer. For example, in Chap. 5, it could take several hours to see avalanche events due to the extremely slow strain rate in the system. However, the frame rate needs to be fast enough to track the emulsion trajectory (details in Sec. 3.2) and also record the details of local structure change, which could be relatively fast. For example, in Chap. 5, though observing avalanche takes long time, local rearrangements happens in a few seconds. For the bright field microscope (Leica DM IRB), we use Kohler illumination to get better image quality (uniform illumination). For this microscope, different objective lens could be used to achieve different magnification including 1.6× and 5× lens. And, there is a lens in the connector that is connecting the camera and the microscope. Their commonly used magnification includes 0.35×, 0.55×, and 1×. These are relatively small magnification. One reason is that our emulsion droplets are not very tiny (typically with diameter $\approx$ 200 μm). Another reason is that we need sufficient number of droplets (typically a few hundreds of droplets) to get good statistics so we need a relatively large field of view. However, under these condition, we want the magnification as big as possible to obtain high resolution. Especially for force analysis, high resolution would increase the accuracy of force measurement

(details in Sec. 3.4).

Both oil phase and water phase are bright (white) in the image while the boundary of the droplet appears dark. The thickness of the droplets' boundary could be different depending on the choices of objective lens, eye piece, and oil phase, which is due to the difference in the indices of refraction between the oil and water. More specifically, the droplets boundary, which is the interface between oil and water, refracts the light from the microscope away. The larger the index of refraction difference gives larger refraction and thus phase difference and thicker boundary in the images. More details about the imaging can be found in Sec.4.1 in Kenneth Desmond's dissertation [93].

Note to future experimenters: it is highly suggested to read Chap. 3 before you start imaging and recording the movie of emulsion flow. The reason is that there are various details you need to keep in mind in terms of recording different parameters of the illumination, taking background image, taking extra images for force calculation, choosing the right format and size of the images, etc. in order to use the IDL programs. A great guidance is in a note for our lab "Notes for Emulsion Tracking with IDL" by Xia Hong, Janna Lowensohn and Carlos Orellana.

Chapter 3

Analytical Method

For the experiments we present in Chap. 5 and Chap. 6, it is essential to know the location of each droplet in order to obtain the local dynamics of the droplets. And, it is important to design the algorithms for the computer to detect local rearrangements during the motion of droplets. It is also great if we can get force information on a droplet scale. In this chapter, we present the computing programs to determine the droplets' location, trajectory, velocity, local rearrangements, and forces. Our programs are written in Interactive Data Language (IDL). The program names are listed in italic.

Note that this chapter is more about algorithms and methods. A great guidance with lots of details about how to use the program is in one of our lab notes: "Notes for Emulsion Tracking with IDL" by Xia Hong, Janna Lowensohn and Carlos Orellana.

3.1 Emulsion Identification

Starting with a high resolution image as the example shown in Fig. 3.1, first step is to convert the image to a 1-bit image. As the figure shows, each droplet has black boundary as the perimeter and both water phase and oil phase are in white. The conversion is to make the image size much smaller not only for a faster processing due to the small size for computers but also for simplicity dealing with less information in the 1-bit image. The conversion is basically pick a threshold, above which all pixels are set to be 1 and other pixels are assigned to be 0. After this, a built IDL function *label_region* can locate the enclosed regions of pixels with value 1, which are the white regions in the 1-bit image. These include both the regions that belong to oil droplets and the voids. In order to distinguish them, the boundaries need to be identified. Given the boundaries as well as the center of the white regions, we can use two metrics to separate them. One is the minimum area: most of our emulsion is far above jamming point, which means that droplets are in contact with each other and there are tiny voids between droplets. Using this metric, the small voids below the minimum area threshold can be ignored (not considered as droplets). Another metric is using the feature of the boundary. As Fig. 3.1 shows, if the white region is convex, it is a droplet; while if the white region is concave, it is a void. After identifying all the droplets, a continuous function using a Fourier series is used to fit the perimeters. More details in Sec.4.4 in Kenneth Desmond's dissertation [93].

Given the location for each droplet, we can decompose the space into polygons. There is only one droplet center assigned in each polygon cell. The method is called radical Voronoi tessellation. An example of a Voronoi tessellation for one of our

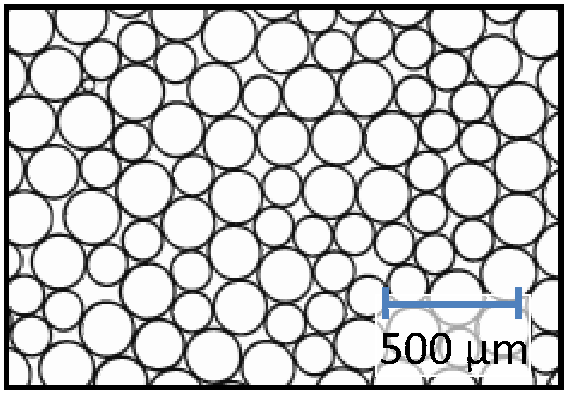

Figure 3.1: Example of a quasi-2D emulsion image. Black denotes the boundaries of droplets and white regions are oil phase and water phase.

samples is shown in Fig. 3.2, where the blue lines indicate the boundaries of the polygon cells, which also could be called Voronoi cells. The algorithm of Voronoi tessellation are based on computing the power distance $pow(r_i, v) = (x_i - v_x)^2 + (y_i - v_y)^2 - R_i^2$, where r_i is the center of a certain droplet, v is an arbitrary point in space, $R_i = \sqrt{A_i/\pi}$, and A_i is the area of the droplet [94, 95]. Then we use the coordinates of three neighboring droplets r_1, r_2, and r_3 to determine the point in space v using $pow(r_1, v) = pow(r_2, v) = pow(r_3, v)$. This point v is the Voronoi vertex for the triplet r_1, r_2, and r_3. There are more rules to restrict which triplets to use for tessellation. We use the built IDL function *qhull* and more details can be found in Sec.4.6 in Kenneth Desmond's dissertation [93] and [94]. Based on the Voronoi cells we obtained, connecting the center of two droplets that share a polygon edge will give you a network. This is called Delauney triangulation, which is unique corresponding to a fixed Voronoi tessellation. Each line of the network is considered as first nearest neighbors in our algorithm. An example is shown in Fig. 3.2. The green lines between each pair of droplets indicates that they are nearest neighbors. This information will

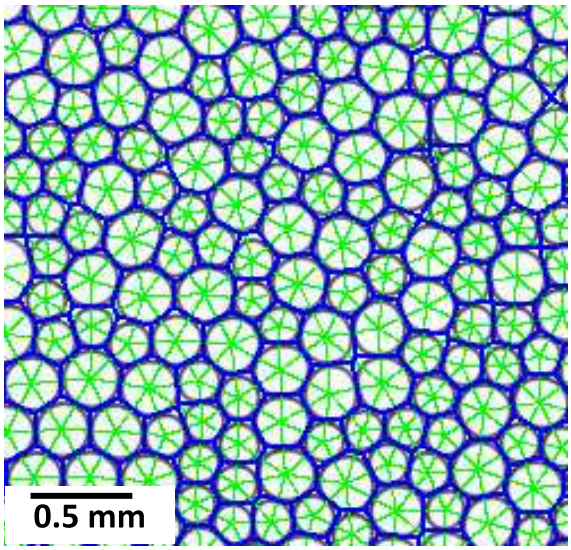

Figure 3.2: Example of a quasi-2D emulsion image with radical Voronoi diagram (blue lines) and its corresponding Delauney triangulation (green lines).

be needed when we capture rearrangements.

When two droplets are in contact, they share a common boundary. Also, when a droplet is experiencing force and thus deformed, the radius of curvature of the droplet would change. In this stage of identifying droplets, we also determine the contacts and the radius of curvature. The contacts identification provide the information to calculate number of contacts for each droplet, which is the contact number z. More details about the contacts and radius of curvature can be found in Sec.4.7-4.9 in Kenneth Desmond's dissertation [93]. Carlos Orellana is working on improving the algorithm of measuring contacts and radius of curvature with the purpose of improving the accuracy of our currently existing force measurement technique.

One important parameter that is calculated during the identification of droplets is the packing fraction, or area fraction ϕ in our 2D system. The ratio of the droplet

area and the area of its corresponding Voronoi cell can be considered as the local ϕ for a certain droplet. The average ϕ is the sum of all droplets' area divided by the whole space. ϕ is one of the main control parameters in this dissertation, so I state the algorithm here and related imaging processing as following. The image is composed of pixels, which give random radius uncertainty. This random uncertainty in radius due to resolution limit leads to a 1% random uncertainty in average ϕ. Another source of uncertainty in ϕ is due to systematic radius uncertainty. It can be related to the imaging artifacts of droplet outlines or the threshold we choose to convert image to a 1-bit image, as mentioned above.

An improvement on the algorithm related with imaging is reflected in my IDL program *xpre_emulsion_track.pro*. For getting larger field of view, I use 1.6× objective lens but the illumination is not as uniform as that with larger magnification. There is no issue with identifying droplets and tracking their trajectory but it could be problematic for future force analysis. I use *xunshade.pro* to a fitting function of the background image and *xpre_emulsion_track.pro* can remove the background mainly by dividing the image by rescaled fitting function of background image. The background image needs to be taken with an empty chamber during imaging.

Another improvement is to automate the process of picking a parameter 'minp' for identifying droplets. 'minp' is the minimal number of pixels of the perimeter of a droplet. It can change due to different batch of emulsion with different droplet size or due to different magnification of the illumination system during imaging. My IDL function *xcheckminp.pro* can display an array of the same image running *xpre_emulsion_track.pro* with different minp values. The results of using each minp

value will play in an IDL display window like a movie with the minp value written in the lower left-hand corner.A copy of the movie will automatically be saved in the working directory as 'checkminp.gif'. More options and keywords can be found in the source code.

List of IDL functions:

- *xunshade.pro*: based on *unshade2.pro* but adding keyword 'offset' to cut the edge of the background image for a better fitting.

- *xpre_emulsion_track.pro*: based on *kpre_emulsion_track.pro* but adding some keywords obtained from *xunshade.pro* and remove the background image from raw image of emulsions to get uniform illumination effect.

- *xpre_emulsion_track_tif.pro*: similar with *xpre_emulsion_track.pro* but dealing with tif type of images.

- *xcheckminp.pro*: display the droplet identification results with different 'minp' values as input for picking the best 'minp'. Type s to make the movie play slower, f to make the movie play faster, r to make the movie reverse, and q to quit. A copy of the movie will automatically be saved in the working directory as 'checkminp.gif'.

3.2 Emulsion Tracking and Velocity

We track the trajectory of each individual droplet using standard software[96]. The main function that I use is *kemulsion_track.pro*. The only parameter that requires

a little bit explanation is 'max_disp', which is the maximum displacement between two successive frames accepted for the program to correctly find the trajectories of all droplets. This is an important parameter since the program is not as smart as our eyes and brains and it might get confused to link the actual trajectory of a droplet. This maximum displacement needs to be smaller than the droplet radius because the program need to see that the next location of the droplet center is close enough to the previous location and thus link them together without confusion. In order to achieve this, a faster frame rate would help the program to track droplets that are moving fast. However, limited by the file size, we cannot use infinitely large frame rate. Our frame rate ranges from 0.2 to 4 images/second.

Another possible concern is about the tracking noise. Limited by the resolution, the identification of the droplet centers have noise, which is less than 0.1 pixel though. We are measuring motions that take place are on length scales of 1-3 μm which are large enough that tracking noise will not be an issue.

Based on the tracking results, we can easily compute the velocity of each droplet including both the direction and magnitude. Once we know how each droplet moves, many variables can be obtained like velocity profile, strain, strain rate, fluctuation, bond breaking events, local rearrangements, etc.

3.3 T1 Events

As mentioned in Sec. 1.2 and shown in Fig. 1.6, a T1 event involves a group of four droplets exchanging neighbors. It seems straightforward to human eyes to catch these events but I have been through some explorations on several algorithms defining

and capturing those rearrangements.

3.3.1 Neighbor Exchange

Originally, Dandan Chen use this idea of neighbor exchanging process. It is based on the Delauney triangulation described in Sec. 3.1 and shown as green lines in Fig. 3.2. Pairs of droplets that are first nearest neighbors and second nearest neighbors can be obtained. Second nearest neighbor is defined as the first nearest neighbor's first nearest neighbor. At the beginning, the program need to find potential groups of four droplets as the T1 events candidates sticking together. After some time, if the program detects two first nearest neighbors becomes second nearest neighbors and another two droplets in the group change from second nearest neighbors to first nearest neighbors, it would be considered as a T1 event.

I use the function *xt1_neighbor_exchange.pro* to identify T1 events for this method. The main parameter is the time window, during which the process happens. If the time window is too short (shorter than a typical rearrangement happens), the program would miss a lot of T1 events that actually happened. If the time window is too large, some super slow process that are not really plastic events would be counted. Based on our observation, the T1 events usually happen in the range of a few seconds to 10 seconds. This might give us a reasonable value to try at the beginning. However, time window is critical and still we need to verify the accuracy of the results by using this method to detect T1 events.

One disadvantage of this method is when the following scenario happens. When two first nearest neighbors move apart for a tiny amount of position, the bond be-

tween these two droplets, which is determined by Delauney triangulation, would break immediately. They are then considered as second nearest neighbors and this might considered as a T1 event, which is not actually a plastic event if these two droplets move that tiny amount of distance back and reverse the process.

List of IDL functions:

- *xt1_neighbor_exchange.pro*

3.3.2 Strain Method

As shown in Fig. 1.6, the red diamond is changing its shape during T1 events. The directionality of major axis and minor axis changes after a complete neighbor exchange. By considering the disadvantage of the neighbor exchange method described in 3.3.2, this strain method can resolve the issue. There are two versions of this method.

If we define the two axis as l_{AB} and l_{CD} as the initial lengths, and l'_{AB} and l'_{CD} as the final lengths after some time, we can define the deformation of the red diamond in Fig. 1.6 during this time window as:

$$D(\Delta t) = \frac{1}{2}|(\frac{l'_{AB} - l_{AB}}{l_{AB}} - \frac{l'_{CD} - l_{CD}}{l_{CD}})|, \tag{3.1}$$

where Δt is the time window we need to choose before running the program. We can get D as a function of time t and pick the peaks as the large deformation and count them as T1 events.

However, this method is not time symmetric. If we reverse the T1 process, the value of deformation defined in Eqn. 3.1 would be different. Using equations, it means $D(\Delta t) = \frac{1}{2}|(\frac{l'_{AB}-l_{AB}}{l_{AB}} - \frac{l'_{CD}-l_{CD}}{l_{CD}})| \neq \frac{1}{2}|(\frac{l_{AB}-l'_{AB}}{l'_{AB}} - \frac{l_{CD}-l'_{CD}}{l'_{CD}})|$. For example, if the initial length l_{AB} is small, the change $\frac{l'_{AB}-l_{AB}}{l_{AB}}$ is biased and over weighted.

It brings us to the second version of the method using strain and deformation idea. If we consider a new definition of deformation as:

$$D(\Delta t) = |\log(\frac{l'_{AB}}{l_{AB}}) - \log(\frac{l'_{CD}}{l_{CD}})| \tag{3.2}$$

It solves the time asymmetry issue because Eqn. 3.2 only consider the change in the length of bonds regardless of initial length of the bond before T1 events. So, it is plausible that another definition would work to make the definition of deformation symmetric but we did not test this:

$$D(\Delta t) = \frac{1}{2}|(\frac{l'_{AB} - l_{AB}}{l'_{AB} + l_{AB}} - \frac{l'_{CD} - l_{CD}}{l'_{CD} + l_{CD}})| \tag{3.3}$$

List of IDL functions:

- *xgett1events.pro*

3.4 Force and Stress

In granular materials, one advantage of them to be a good experimental model system is that forces can be measured using photoelastic disks. As shown in Fig. 3.3, the bright particles are experiencing large forces and they can be accurately measured by extract information out of the light pattern in each particle. Force chains are

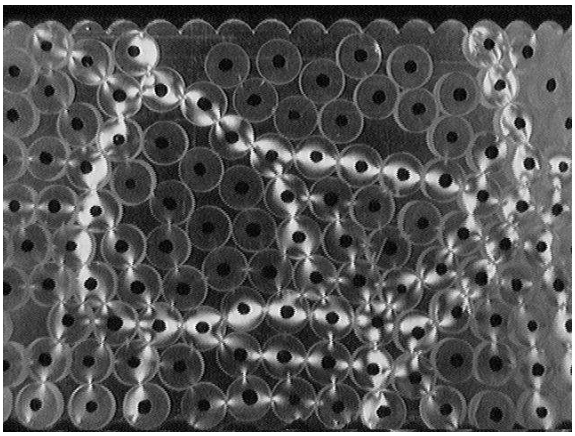

Figure 3.3: Photoelastic disks viewed between cross-polarizers. They are confined to a thin channel so that they are a two-dimensional system, and they are compressed between the top and bottom of the image. The bright particles are experiencing large forces. (Picture from SV Franklin & ER Weeks.)

a powerful idea in granular physics, and almost all experiments related to dense granular materials invoke force chains as an explanation for their observations [97, 98]. So, it is really cool for our lab to have force measurement technique in 2D emulsion system developed by Kenneth Desmond based on the observed deformation of droplets. And, we can measure forces in a simpler way. The empirical force law works well for our 2D emulsion system. More details can be found in Chapter 5 in Kenneth Desmond's dissertation [93]. Recent work has shown success in 3D force measurement technique using imaging with refractive index matching tomography and based on the deformation of fluorescence dyed hydrogel particles [99].

Basically, our empirical force law is a function of contact length l of each contact and radius of curvature r of each droplet. The bigger the contact length is, the bigger force the droplet is experiencing. Inversely, the smaller radius of curvature, which means the boundary of the droplet is more curved, the bigger the force is. The

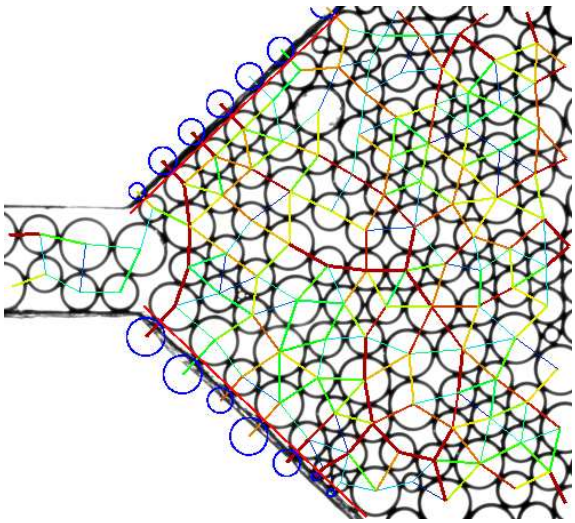

Figure 3.4: Force on the boundary. Blue circles are the imaginary droplets. Color lines are the forces (more red-ish denotes bigger forces).

noise level depends on the illumnication setting. Higher resolution would give the measurement of l and r higher accuracy. This is alao why we choose the magnification mentioned in Sec. 2 to get as high resolution as possible given the limit of large field of view. More details are in Kenneth Desmond's dissertation [93] and his publication [14].

3.4.1 Force On the Boundary

One technique that I developed but not used in this dissertation is to calculate the forces on the boundary. The idea is to get the forces on the wall of the chamber and thus obtain the pressure to make the boundary work like a pressure sensor. As shown in Fig. 3.4, the blue circles are the imaginary droplets, which are used in order to apply the existing force law. The reason is that our empirical force law only works in the case of two droplets that are in contact.

List of IDL functions:

- *xbdforce.pro*: get forces for the droplets on the boundary.

3.5 Visualization

Various visualization functions exist in our IDL function library. I integrate them into a big program with lots of keywords, acting like a visualization package. The function is *xmkvismovie.pro*. Various options include saving is as a picture or movie, scale the value of the variable you want to display, use different symbol styles like colored circles, gray-scale circles, arrows, etc. and you can choose different variable to be indicated by colors or the size of the symbols. The purpose is to build a tool in IDL that is integrated, fast and easy to visualize different kinds of variables. It works well especially with droplets. Fig. 6.20 is an example as a snapshot of a movie.

List of IDL functions:

- *xmkvismovie.pro*: powerful visualization tool with 2D emulsion system.
- *xcolorbar.pro*: based on *kcolorbar.pro* but added RBG option to deal with RGB three channel color wheel or color palette.

Chapter 4

Clogging of Oil Droplets in 2D Hopper

4.1 Introduction

Flowing sand differs qualitatively from flowing fluid and understanding the differences leads to interesting physics [40, 100]. A dramatic difference is seen in the gravity-driven flow of sand out of a hopper: when the exit opening from a hopper is small, the sand can clog at the hopper exit [68, 101]. The existence of a critical exit opening size of 3-6 particle diameters has been long-known [49–51, 74, 77, 102, 103]. Even when the hopper opening is slightly larger, and clogs do not form, the flow is influenced by the possibility of clogging: for example, there are fluctuations of the flow rate of the sand [52–54]. The mean flow rate is a function of the difference of the opening size to the critical size for clogging, a result often attributed to Beverloo [49] although mentioned by earlier authors as well [50]; see a discussion of the history

in Ref. [51]. In this sense, understanding what happens when hoppers clog – and the size of the opening that causes clogging – is crucial for understanding the flow properties when the opening is larger than the critical size [49, 51]. We note that two experiments suggest that clogging does not have a critical size but rather becomes exponentially unlikely as the hopper opening increases [55, 104]; nonetheless, it's clear that understanding the flow properties requires understanding the clogging probability.

The clogging process itself is known to be due to arch formation at the hopper exit [1, 53, 55]. The difficulty of forming large arches is the reason why hoppers do not clog when their exit opening is sufficiently large [1]. For that matter, observations of clogging at the hopper exits are a way to probe the sizes of arches which may also be present in the interior of granular materials [105–107]. Friction might be important for the formation of these arches [1], and more generally it has long been seen that friction influences hopper flow to an extent [50–52, 54, 108]. However, it was unclear exactly how friction played a role – friction influences the angle of repose [108] and the packing density [49], for example, but it was unclear which of these (if either) influences the flow rate or clogging. A different experiment studied the flow of foams, and showed that the softness of the bubbles influenced the flow [71]. In this case, there was no static friction. Due to the ability of bubbles to deform, clogging required the exit orifice to be smaller than the mean bubble size, and this profoundly changed the flow rate at larger exit orifice sizes [71] as compared to the granular Beverloo flow law [49]. One recent experiment used repulsive magnetic particles in a quasi-2D hopper and reported clogging for small orifices, but did not systematically study clogging

[109]. In that work, the particles repelled each other at moderate separations, and so it was not clear how the clogging related to the particle size (or even how to define that size). Another experiment studied the shapes of arches formed in 2D granular hoppers, finding that the effect of static friction is quite relevant for arch formation and these shapes differed somewhat from simulated frictionless arches [110].

In this chapter, we experimentally study a quasi-two-dimensional emulsion as a model of a soft frictionless granular material. More detailed features about the sample is mentioned in Sec. 2.2 in Chap. 2. The droplets are sandwiched in a hopper chamber, as shown in Fig. 4.2. While these droplets feel a viscous force when they move, they do not experience any static friction between each other or with the glass. We find that in our experiments, droplets only clog when the hopper opening is less than two diameters wide. Arches, to the extent they can be defined, involve only one or two droplets. Our results are a strong contrast to prior results from two-dimensional experiments using hard frictional granular particles, which saw larger arches and which clog at larger opening sizes [1, 54, 55, 102, 111, 112]. This is a dramatic demonstration of the significant influence of friction or softness on the clogging process, and shows that flowing particulate materials behave qualitatively different in our emulsion system when friction is absent and particles are easily deformable by the flow. However, it is unclear which of these two is playing the critical role. A later simulation work with frictionless particles and varying the softness of the particles, done by Eric Weeks using Durian bubble model [13], shows that the softness of the experimental droplets explains the ease of flow that observed in the experiment. In addition, we also observed some interesting phenomena in monodisperse samples which might be

related to breaking a crystal. This is seen when droplets have crystalline packing close to the hopper exit. However, this is only a preliminary observation without analysis or explanation and might be a direction to explore in the future on polydispersity of the packing.

4.2 Experimental Methods

The droplets are prepared using the methods introduced in Chap. 2. The oil we chose for this experiment is mineral oil (details in Sec. 2.2). In some cases we mix together two batches of droplets with different sizes, but for most of our results we study samples composed of a single batch of droplets. Sometimes the emulsion gets sheared when we add it to the sample chamber, resulting in a few droplets that are unusually small, or the coalescence of droplets so that some are unusually large. Examples of each can be seen in some of the images in this chapter.

Each sample chamber is a sandwich of a spacer between two glass slides, as shown in Fig. 4.1. The spacer material is either transparent plastic film (≈ 120 μm thickness), double sided tape (≈ 100 μm thickness) or parafilm (≈ 130 μm thickness). For each of these, the spacer material is cut into a desired shape using scissors. We briefly put the parafilm chambers onto a hot plate to slightly melt the parafilm to seal the chamber. For the plastic film chambers, we adhere films to glass slides using UV epoxy (Thorlabs NOA81). In each case, after the initial preparation, the sample chambers are additionally sealed with epoxy to prevent leakage or evaporation. As we use scissors and position the spacer materials onto the slides by hand, often the sample chambers are imperfect. However, given the simplicity and rapidity of

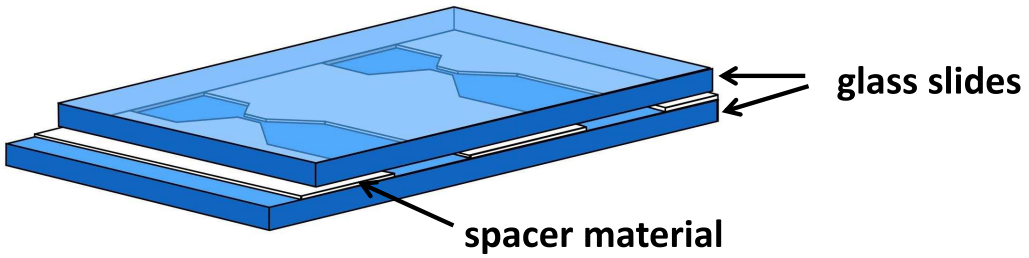

Figure 4.1: Sketch of hopper chamber construction. Two glasses (in blue) are separated by pieces of spacer materials (in white). Figure credit to Meghan Kohne.

making these chambers, we simply select the best sample chambers to use in our experiments, where the hopper exit is adequately shaped. Examples are shown in Fig. 4.6 and Fig. 4.14. The hopper angles are set to be $32 - 35°$, close to To *et al.*'s experiment with an angle of 34° [1]. Given the spacer thickness (≈ 120 μm or ≈ 130 μm) and the droplet diameter (≈ 200 μm), note that the emulsion droplets are neither too small nor too large. If the droplets are too small, they would stick to the glass slides; while if they are too big, they would easily flow through the hopper exit and it will be difficult to see a clogging event. The high deformability seems counterintuitive but this is due to the low penalty from surface energy comparing to the high reward from gravitational energy (more details will be explained in Sec. 4.3).

The chamber designs have gone through various versions. First version of chambers, as shown in Fig. 4.2(a), are made by plastic film. There is only one hopper chamber in one slide and the chamber is sealed up by high vacuum grease. Since our aim is to measure the clogging probability and the number of trials is large, observing one hopper at one time is not efficient. The long channel of hopper also takes a long time for droplets going through. Second version of chambers, as shown in Fig. 4.2(b),

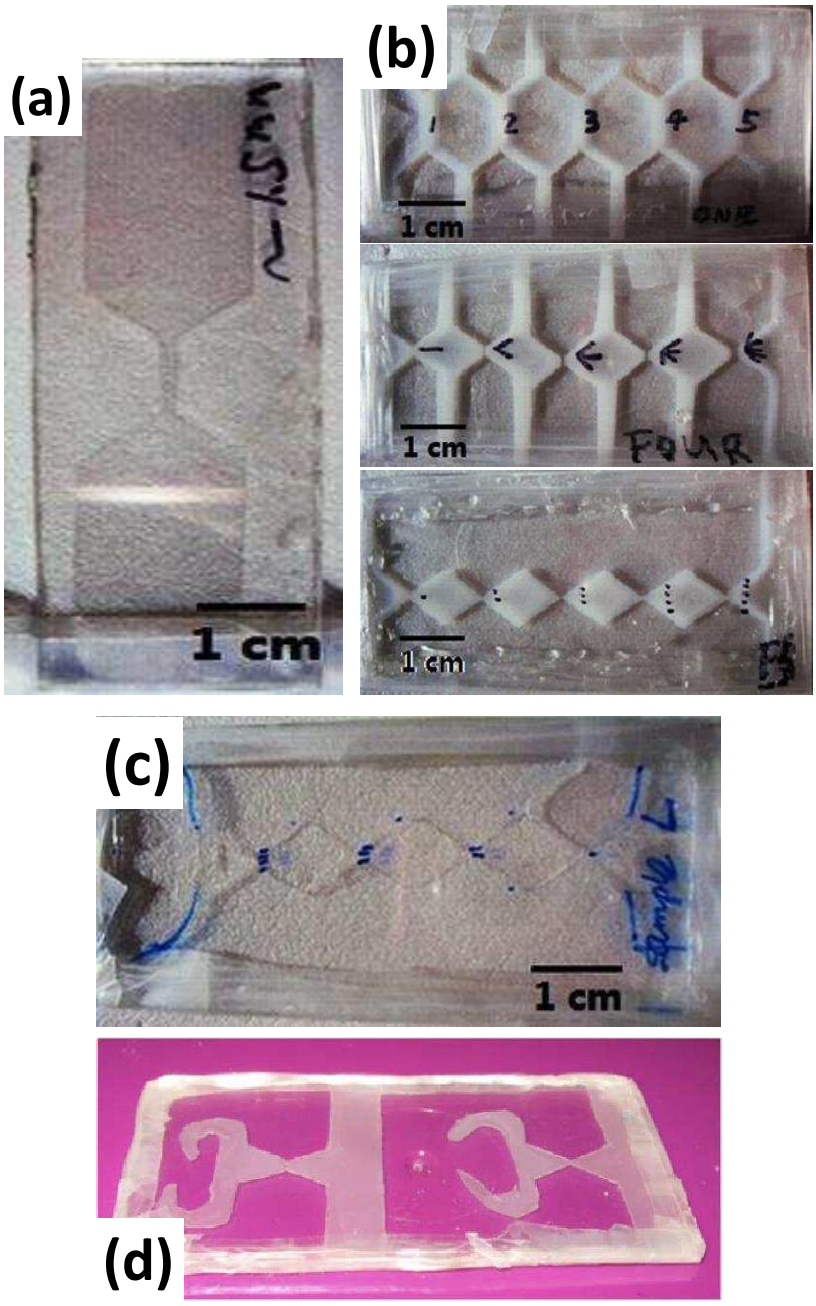

Figure 4.2: Photograph of different versions of chamber design: (a) version one: there is only one hopper chamber. Spacer material: plastic film. (b) version two: The top two slides each contains 5 hopper chambers that are not interconnected. The bottom one slide contains 5 interconnected hopper chambers. Spacer material: double sided tape. (c) version three. Spacer material: plastic film. (d) version three(Meghan Kohne's chamber). Spacer material: parafilm.

are made of double sided tape. It takes shorter time to make a chamber and the channels of hoppers are shorter, which makes the experiment more time efficient. There are 5 hopper chambers in one slide. The chamber is sealed up by high vacuum grease and parafilm. However, double sided tape can absorb liquid over time and the chamber cannot last long for reuse purpose. Should droplets flowing through the hopper clog, we need a way to unclog the system and get all of the droplets back to the entrance side of the hopper. Both version one and version two have the issue of getting air bubbles into the sample during loading droplets and also the unclogging process is difficult. We design our version three sample chambers with a side channel as shown in Fig. 4.2(c)(d) and also in the chamber schema as shown in Fig. 4.3. This allows the sample chamber to be tilted and gives a path to move droplets from one side of the hopper to the other. The "C" shape on the left side of the individual chambers shown in Fig. 4.2(c)(d) is to collect and hold any air bubble that might be present after the emulsion is added to the chamber. Fig. 4.3 is the sketch of the process of collecting air bubbles. When the chamber is flipped from position as shown in Fig. 4.3(a) to position as shown in Fig. 4.3(b), air bubbles run faster than oil droplets under gravity because air and water have bigger density difference than the oil and water. Till air bubbles get together and coalesce into a big air bubble, I flip the chamber back to a position like Fig. 4.3(c) so that the big air bubble can stay in the "C" shape hook and will not influence the oil droplets flow near the opening of hoppers.

Given the fairly large size of the droplets, we use a CCD camera and a macro-zoom lens to view our experiments, back-lighting the sample chamber. As shown

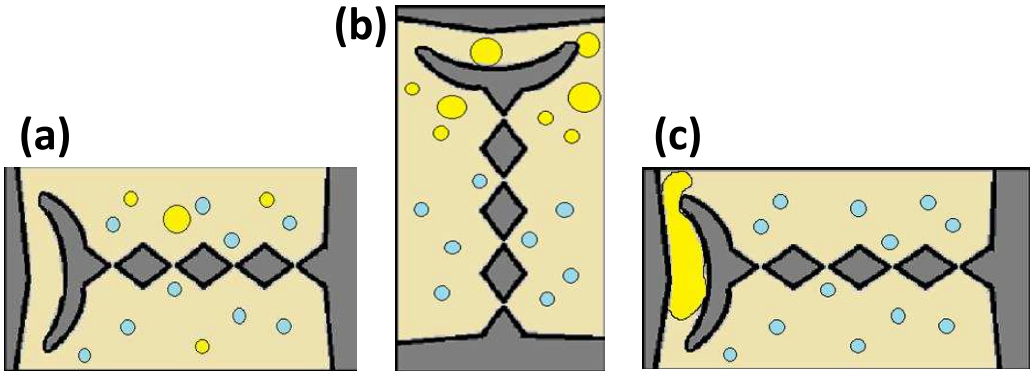

Figure 4.3: Sketch of the version three chamber and demonstration of how the "C" shape collecting air bubbles. Gray area is plastic film; yellow circles are air bubbles and blue circles represent oil droplets. (a) chamber position before air bubbles are collected; (b) chamber is flipped and to collect air bubbles and the bubbles will merge together; (c) after air bubble is collected and trapped in the "C" shape hook.

in Fig. 4.4, the light comes from a lamp covered with a paper to uniform the light source. After going through a convex lens, the light is focused on the sample and goes into a camera lens before finally producing images in the CCD camera. Some of the movies are taken at frame rate 33 ms/frame and images saved every 5 images taken, which gives the actual frame rate 165 ms/frame. Clogged hoppers can also be seen by eye, which makes it possible to collect statistics without the camera. Video microscopy is used to count the number of droplets within a sample chamber, and to get an accurate measurement of the hopper angle of each chamber.

4.3 Physics of Flowing Emulsions

The original idea of my study is intrigued by the work in Kiwing To's lab [1], which is described in Sec. 4.1. As Fig. 4.5(a) shows, Kiwing To put 200 monodisperse stainless steel disks into a 2D hopper. The thickness of disks is 3mm and their

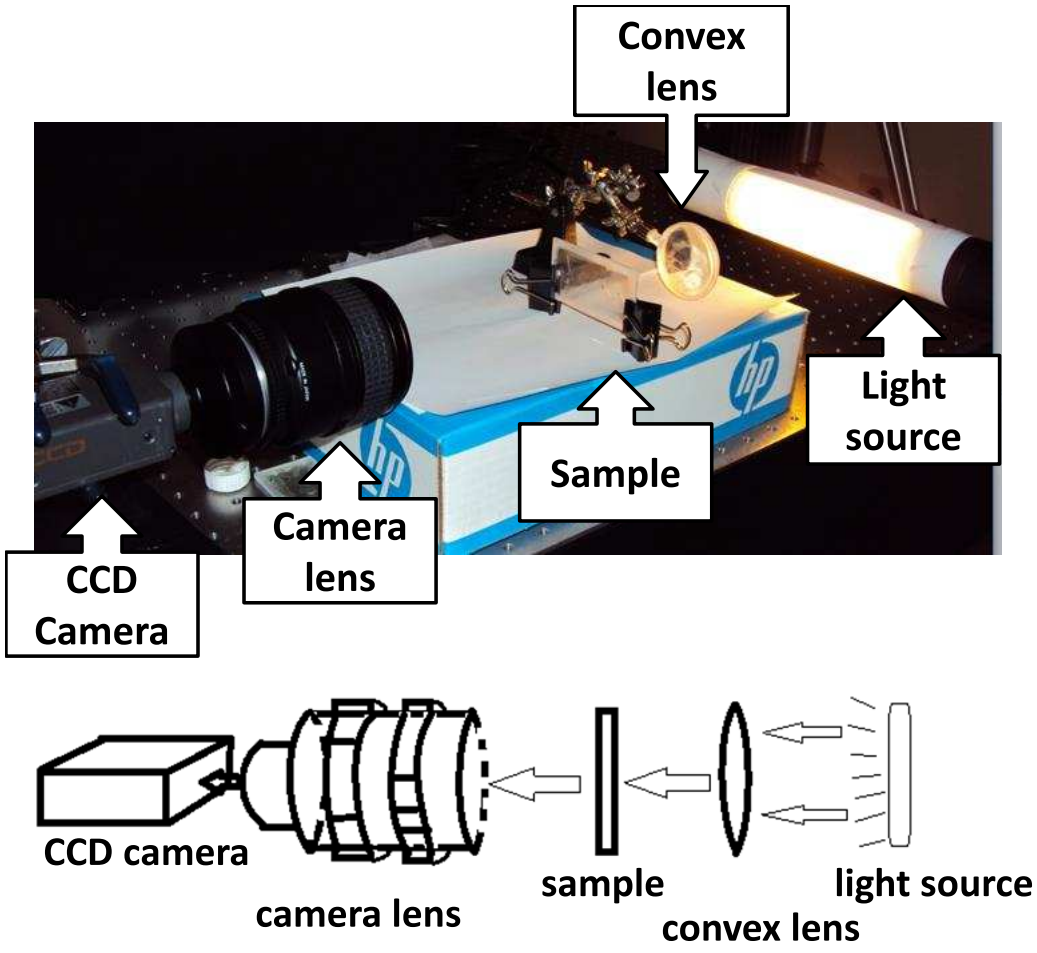

Figure 4.4: (a) Photograph of illumination apparatus; (b) Sketch of light path.

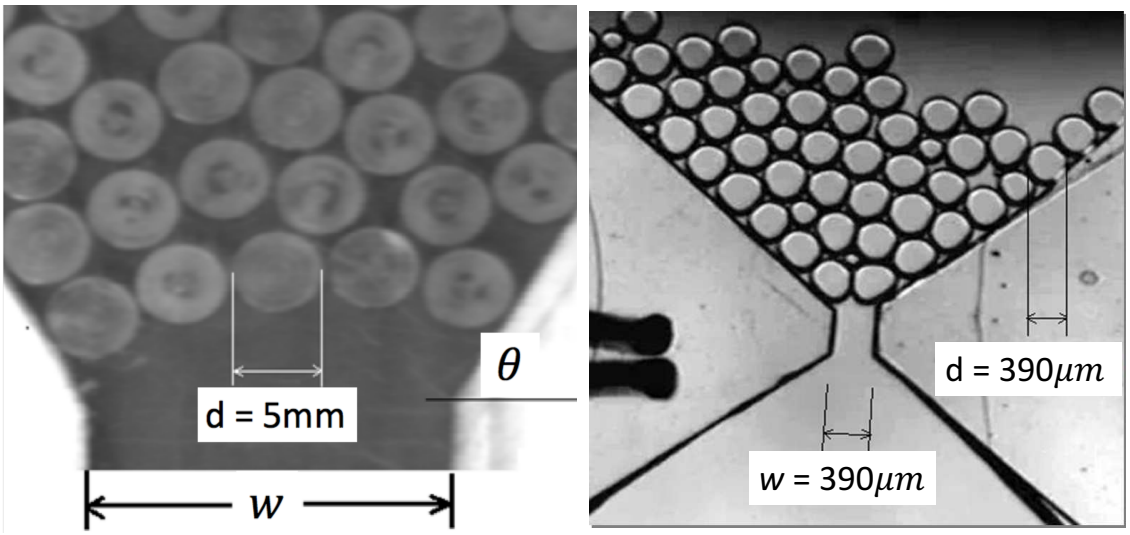

Figure 4.5: (a) Photograph of hopper with hard disks in To's experiment [1]. w is the hopper width and $d = 5$ mm is the diameter of their hard disks. (Reprinted figure with permission from [Kiwing To, Pik-Yin Lai, and H. K. Pak, Phys. Rev. Lett. 86, 71, Jan. 2001] Copyright (2001) by the American Physical Society, License number:3814270507187). (b) Image of hopper with emulsion in my experiment. Typical diameter of the droplets is about 390 μm.

diameter is 5mm. The thickness of the hopper is 4mm so that disks cannot flip over inside the hopper. While we are motivated by this experiment on granular hopper flows, there are several differences in our experiment. These differences are described in this section.

A superficial difference is that the density of the mineral oil droplets ($\rho = 0.83$ g/mL) is smaller than water ($\rho = 1.00$ g/mL), so our droplets float upward due to gravity. To make easier conceptual comparison with granular hoppers, we rotate all of our photographs so that the droplets are moving downward, for example Fig. 4.6.

A second difference is that our droplets are soft and deformable. The original work by To *et al.* used steel disks [1, 113–115], some authors use solid spheres [55, 68, 104, 110], and later work by others used slightly deformable photoelastic disks

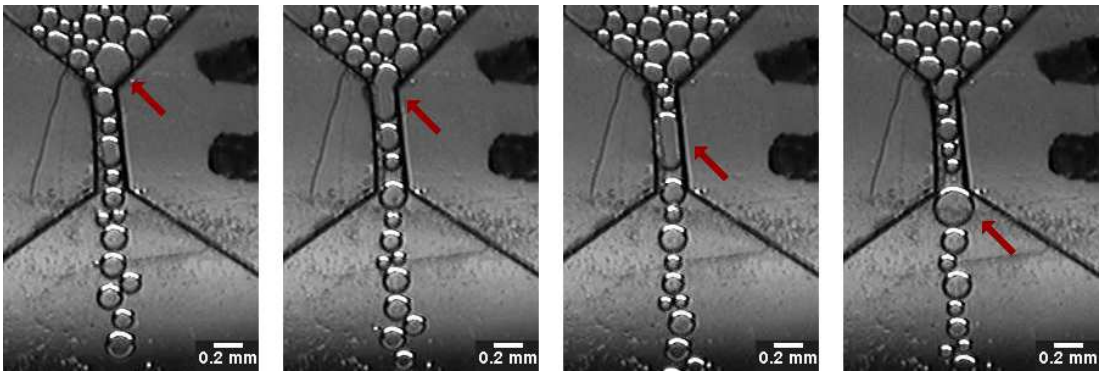

Figure 4.6: This image sequence shows how a big droplet can deform and squeeze through the hopper exit, if the surface tension is too low. The images are shown at 10 s time intervals.

[54, 111, 112]. Our droplets are significantly more deformable. In the absence of external forces, a droplet would be spherical due to surface tension. However, in our experiment, droplets could potentially decrease their gravitational potential energy by deforming to squeeze through the hopper. This is indeed what happens if the surface tension is too small, or if the droplets are too large: an example is seen in Fig. 4.6. As the gravitational energy over a length scale d scales with droplet diameter as d^4 while surface energy scales as d^2, larger droplets will prefer to deform to reduce their gravitational energy [116]. Accordingly, to study clogging in our hoppers, we use a low amount of surfactant to keep the surface tension high, and also we use smaller droplets. This prevents the problem seen in Fig. 4.6. Were we to use large droplets, they would still clog if the hopper opening was sufficiently narrow, but this would then be entirely a surface tension effect rather than a study of clogging.

A third difference between our experiments and the prior granular experiments is that our oil droplets move through a viscous background fluid (water, viscosity $\eta \approx 1$ mPa·s). The mineral oil droplets are themselves viscous ($\eta \approx 20$ mPa·s)

and experience viscous drag with the glass slides. The droplets contact the glass slides with a contact angle of 19° [14]; in other words, there is no lubricating water layer between the droplets and glass. The viscous drag on the droplets means that they move slowly, about $0.20 - 0.25$ droplet diameters d per second depending on the conditions. This is in contrast to the granular experiments where particles spill out of the hopper quite rapidly [112]. This in principal might make clogging easier, as droplets moving toward the hopper exit have less inertia. Of course, the prior 2D granular experiments have some viscous drag from air, and also experience some sliding friction against their confining walls [1, 55].

A fourth difference is that in a granular container, the pressure is independent of depth (apart from near the free surface at the top, and at the bottom near the exit). This is known as the Janssen effect [117], and is due to the frictional forces acting on the particles from the container sidewalls [51, 118, 119]. Due to our droplets not having static friction, we would not expect the Janssen effect to be present in our experiment. (Of course, some weight of the droplet pile is supported by the sloped hopper walls.) The lack of a Janssen effect was confirmed by an earlier experiment by our group, which found the internal pressure within a similar quasi-2D emulsion pile depended on depth in a tall container [14]. This also is similar to a granular hopper experiment using submerged particles [77], which did not find a Janssen effect. Accordingly, we might expect that clogging should be reduced in our experiment if large numbers of droplets exert forces on the droplets at the exit. On the other hand, the density mismatch between the oil and water is only $\Delta\rho = 0.17$ g/mL, so the gravitational forces acting on our droplets are small albeit necessary for driving the

hopper flow.

To be clear, the Janssen effect is thought to be irrelevant for understanding hopper flow. For example, one experiment removed the influence of gravity and provided strong evidence the Janssen effect is unrelated to clogging and flow rates through hoppers [74]. It is well known that granular hopper flow is independent of the amount of material in the hopper, as long as the amount of material is above some minimal threshold [49, 74, 104]. In contrast, that should not be the case in our experiments and is confirmed by the unpublished simulation work done by Eric Weeks. As the weight above the droplets at the exit decreases, the probability of clogging increases. In other words, our experiment cannot be treated as in steady state, in contrast to granular hoppers [101, 104]. For granular experiments, this allows one to focus on the amount of material between clogs, using some method of unclogging a clog [104, 110]. In contrast, our experimental protocol is based on To *et al.* where we study the probability for the hopper to completely drain for a fixed initial number of droplets [1, 113].

4.4 Results

4.4.1 Cases of No Clogging

There are two cases in our experiments that we observed no clogging.

The first case is when the droplets are very large, greater than 300μm in diameter. They can be largely deformed and squeeze through the narrow hopper slowly where the exit width w is smaller than droplets diameter. The physics is the same as

mentioned above in Sec. 4.3 that the energy reward from gravity scales with droplet size $\sim d^4$ while the energy penalty from deformation scales with droplet size $\sim d^2$. So, for large d, there is more energy reward than penalty, which makes the droplet easier to deform and flow through the hopper exit. As shown in Fig. 4.6, the big droplet, pointed by an arrow, deforms and passes through the hopper. Another example is shown in Fig. 4.7(a), comparing with the smaller droplets, which can pass the hopper without deformation. This phenomenon shows the important difference between emulsions and hard disks, as mentioned before, that emulsion droplets are easily deformable while hard disks are almost not deformable at all in our force range.

The second case is when the droplets are not very large and ratio of exit width to droplet diameter is large $w/d > 2$. Fig. 4.7(b) shows a typical image for this case. When we zoom out, we observe some interesting solid-like property of the emulsion flow. Small droplets, with diameter $100 \sim 180\mu$m, flow quickly but discontinuously like sand flow in a sand glass even though the hopper opening is big (the opening width is more than 2 times bigger than the droplets diameter). In Fig. 4.8(a), there are big clumps of droplets flowing down and at the bottom the droplets accumulate like a pile of sand, which is composed of sand particles with static friction. Fig. 4.8(b) shows more details as we zoom in. This might be related to one feature of our emulsion system that there is slight adhesion between droplets, as observed in previous work [14].

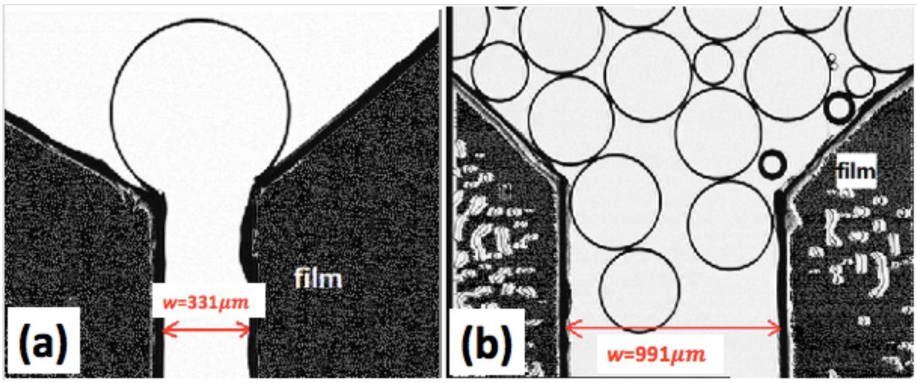

Figure 4.7: (a) A large droplet squeeze through the hopper exit; (b) Small droplets pass through the hopper without deformation.

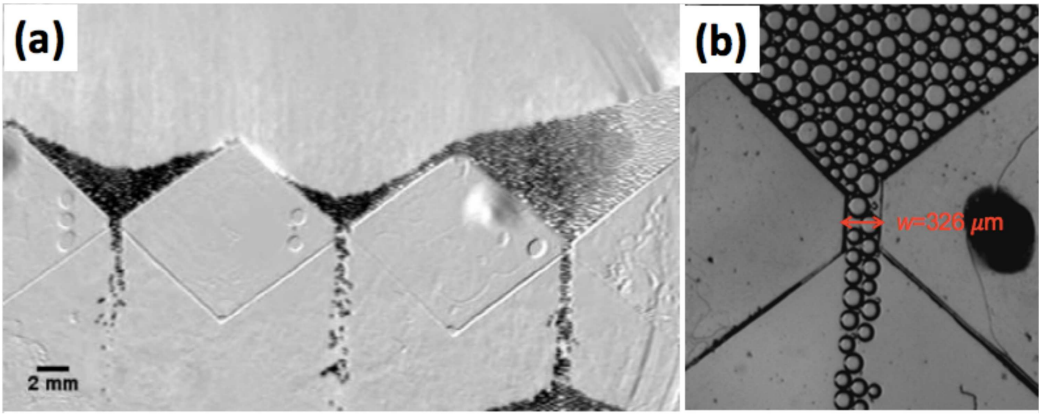

Figure 4.8: Solid like property of small droplets: small droplets flow through hopper exit like sand glass.

4.4.2 Cases of Clogging

For the clogging cases, data are collected by two persons: Meghan Kohne and Xia Hong (myself). Most of the experimental settings are the same with some small differences. The differences include:

(1) Spacer material: Meghan Kohne uses parafilm and I use plastic film for the data collected.

(2) Number of trials: Meghan Kohne has 50 trials for each clogging probability calculated while I only have 4-7 trials for each data point.

(3) Number of droplets loaded: Meghan Kohne has 750 - 950 droplets in each chamber but I use a lot fewer droplets (couple hundreds, accurate numbers are missing).

(4) The definition of clogging: Megan's definition is simply that oil droplets stop flowing and clog the hopper opening, while my definition is that there are less than 50 droplets passing the hopper and there is no droplet between the hopper opening and chamber boundary. Fig. 4.9 is the sketch of different examples. Droplets are flowing down. From left to right, the first hopper is not clogged since there are droplets flowing between hopper exit and the bottom boundary of the slide. The third hopper is clogged since there are less than 50 droplets passed the hopper (there are 6 droplets on the boundary in the sketch) and there are no droplets between the hopper exit and the boundary at the bottom in the sketch. This difference in definition of clogging could be crucial since different definition of clogging could lead to different results. For example, sometimes the droplets clog the hopper but after several seconds they start flowing again, which can be considered as either clogging event or not depending on the predefined time window of that several seconds.

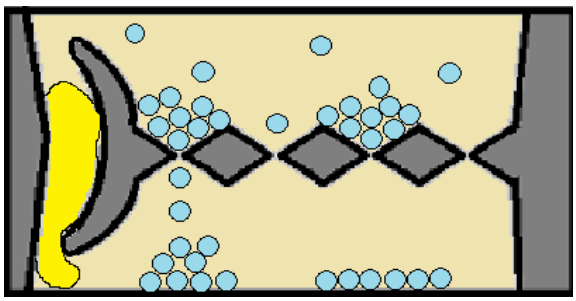

Figure 4.9: Sketch for my definition of clogging. From left to right, the first hopper is not clogged since there are droplets between hopper exit and the bottom boundary of the slide. The third hopper is clogged since there are less than 50 droplets passed the hopper (there are 6 droplets on the bottom boundary in the sketch) and there are no droplets between the hopper exit and the bottom boundary.

All Meghan Kohne's data are marked in the context and the captions of plots.

To determine clogging probabilities, we load our sample chamber with droplets and hold the slide vertically to maximize the buoyant force. We then let these droplets flow through the sample chamber and observe if a clog forms.

The probability of clogging P_{clog} as a function of the hopper exit width w (normalized by the mean droplet diameter d) is shown in Fig. 4.10 for Meghan Kohne's results and in Fig. 4.11 for my results. The most striking result is that the widths of hopper opening at which clogging occurs are quite small. At $w/d \approx 1.4$, the droplets clog for half of the experiments, and for larger hoppers, clogging is never observed. This is in stark contrast to the case of granular material composed of hard frictional disks, which clog for half of the trials at $w/d \approx 4$ as shown in Fig. 4.12 and Fig. 4.13 (no need to pay attention to the details in these figures for now) [1]. Clearly the absence of friction decreases the ability of the system to clog.

Note a caveat: the probability of clogging should be approximately constant for

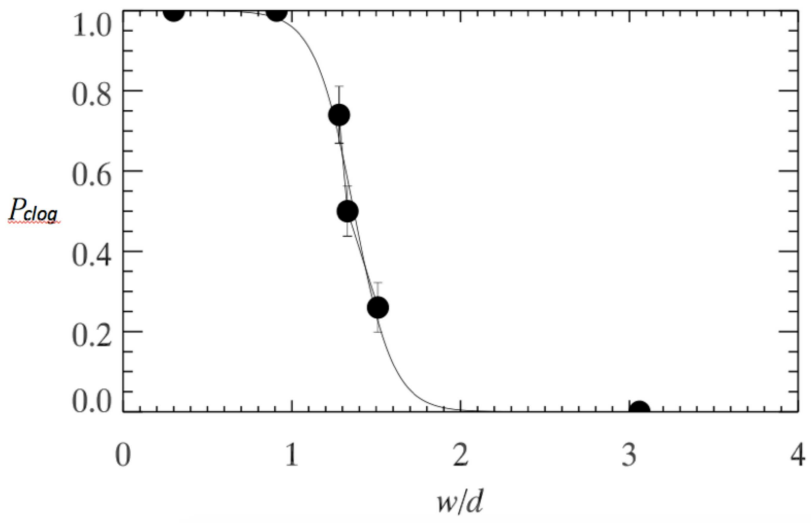

Figure 4.10: The probability of clogging as a function of w/d, which is the ratio of the hopper exit width w to the droplet diameter d. The data correspond to Table 4.1. The solid line is a fit to the sigmoidal function $P_{\text{clog}} = [1 + \exp((w/d - a)/b)]^{-1}$ with $P_{\text{clog}} = 1/2$ at $w/d = a = 1.37$ and width $b = 0.17$. The error bars are the uncertainties due to the finite number of trials ($n = 50$) for a Poisson process.

a given number of droplets flowing through the exit [55, 76, 111, 115]. With more droplets, there is more chance of observing clogging, if the probability of clogging per droplet is nonzero. We cannot perfectly control the number of droplets in our sample chamber, so the cases with more droplets will have P_{clog} larger. In Meghan Kohne's data, for the three points with $0 < P_{\text{clog}} < 1$, the number of droplets is fairly similar (see Table 4.1). In the first experiment reported by To *et al.* they used 200 particles [1], approximately a quarter of the number Meghan Kohne uses and the same number I use. Their later work showed that with more particles P_{clog} moves to larger w/d [113]. They found $P_{\text{clog}} = 1/2$ at $w/d \approx 4.0$ for 200 particles, and ≈ 4.8 for 700 particles. Janda *et al.* found qualitatively similar results in their 2D granular experiment, with $P_{\text{clog}} = 1/2$ increasing from $w/d \approx 3$ with 50 particles to $w/d \approx 5.5$

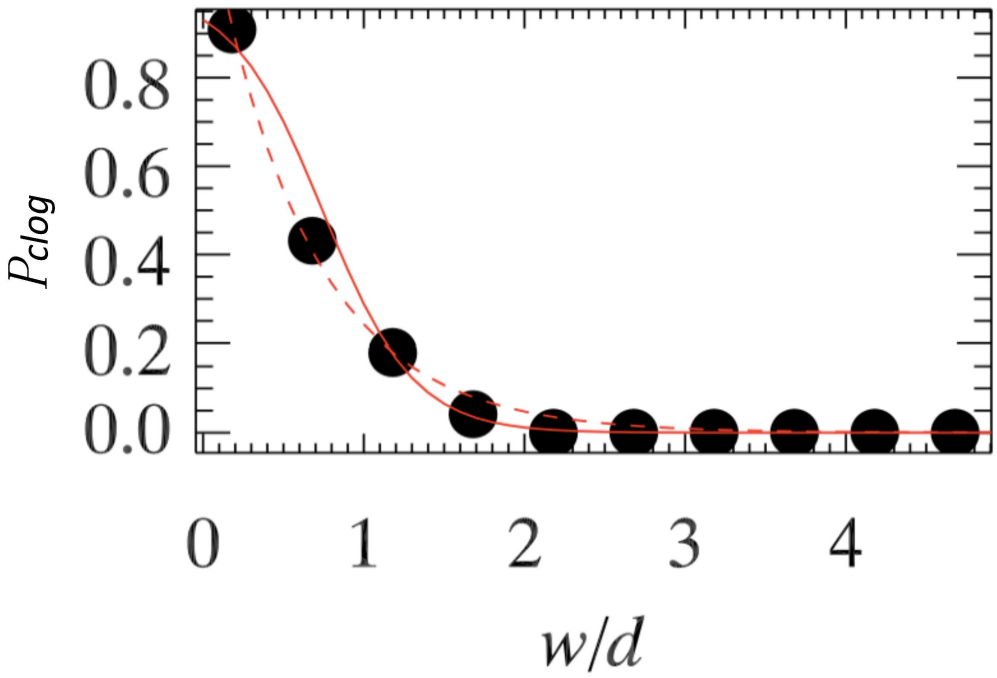

Figure 4.11: Clogging probability from Xia's data as a function of hopper width. The red solid line is a fit to the sigmoidal function $P_{\text{clog}} = [1 + \exp((w/d - a)/b)]^{-1}$ with $P_{\text{clog}} = 1/2$ at $w/d = a = 0.79$ and width $b = 0.33$. The red dash line is an exponential fit $P_{\text{clog}} = 1.23\exp(-1.62w/d)$ with $P_{\text{clog}} = 1/2$ at $w/d = 0.55$. Both fittings have their good matching over some range but our sparse data is not sufficient to tell the difference. Note that exponential cannot be true for sufficiently small w/d, where $P_{\text{clog}} > 1$.

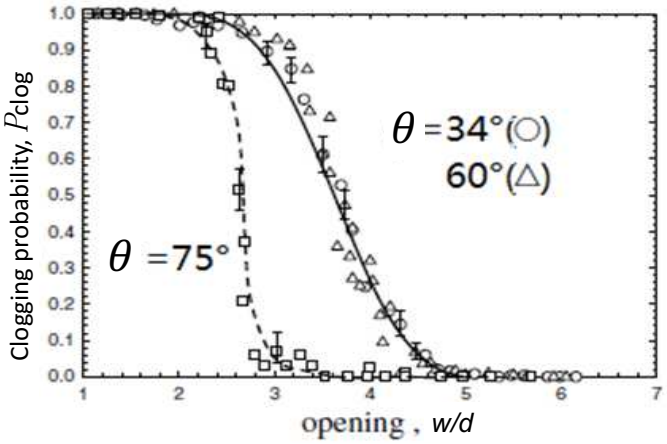

Figure 4.12: Clogging probability of granular experiment for different hopper angles [1]. The angle θ is defined as the hopper angle as shown in Fig. 4.5. (Reprinted figure with permission from [Kiwing To, Pik-Yin Lai, and H. K. Pak,Phys. Rev. Lett. 86, 71, Jan. 2001] Copyright (2001) by the American Physical Society, License number:3814270507187)

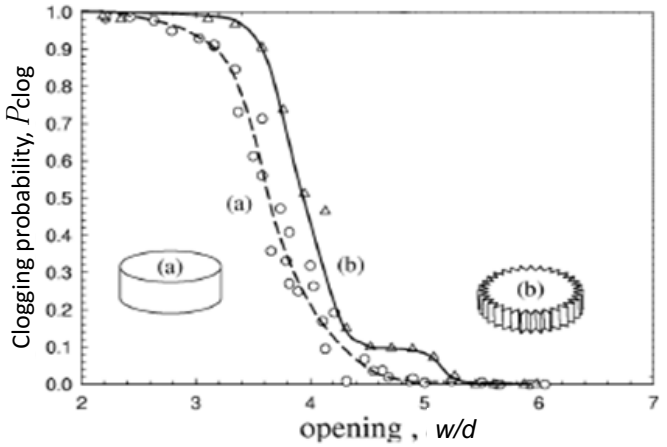

Figure 4.13: Clogging probability of granular experiment for different friction coefficients [1]. (a) represents hard disks with lower friction coefficient and (b) are disks with 25 V-shape grooves of 0.2 mm deep at its circular edge to have a lot higher friction coefficient. (Reprinted figure with permission from [Kiwing To, Pik-Yin Lai, and H. K. Pak,Phys. Rev. Lett. 86, 71, Jan. 2001] Copyright (2001) by the American Physical Society, License number:3814270507187)

w/d	d	N	θ	P_{clog}
0.30	237 μm	867	32°	1.00
0.91	202 μm	947	35°	1.00
1.28	250 μm	771	33°	0.74
1.33	280 μm	786	35°	0.50
1.51	285 μm	764	33°	0.26
3.06	280 μm	923	34°	0.00

Table 4.1: Details of Meghan Kohne's six experiments that measured clogging probabilities. w is the hopper exit width, d is the mean droplet diameter, N is the number of droplets, θ is the hopper angle, and P_{clog} is the probability of clogging based on 50 trials. The uncertainty of d is ± 5 μm, and the uncertainty of w/d is ± 0.03.

with 50000 particles [55]. Fitting Meghan Kohne's data to a sigmoidal function as shown in Fig. 4.10, we have a width ≈ 0.2. Fitting my data to a sigmoidal function as shown in red solid line in Fig. 4.11, we have a width ≈ 0.33, which is similar with To's widths ≈ 0.3 [1]. The discrepancy between Meghan Kohne's and my results are probably due to our different number of droplets and different definition of clogging. These possibilities include:

(1) the time window that I choose is basically for a droplet flowing from hopper exit to the upper boundary. However, this time window could be too small. For example, if the droplets start to pass through the hopper exit again, I could overestimate the clogging probability and thus gives higher width at $P_{\text{clog}} = 1/2$.

(2) The second possibility could be that the number of trials of my experiments are too small and thus the uncertainty could be large for the width calculation.

(3) The third speculation is due to the imperfect construction of hopper chambers and this hopper mismatch could increase clogging probability as explained in Sec. 4.4.3.

It is not clear that the sigmoidal fit we use is correct; To *et al.* used a different

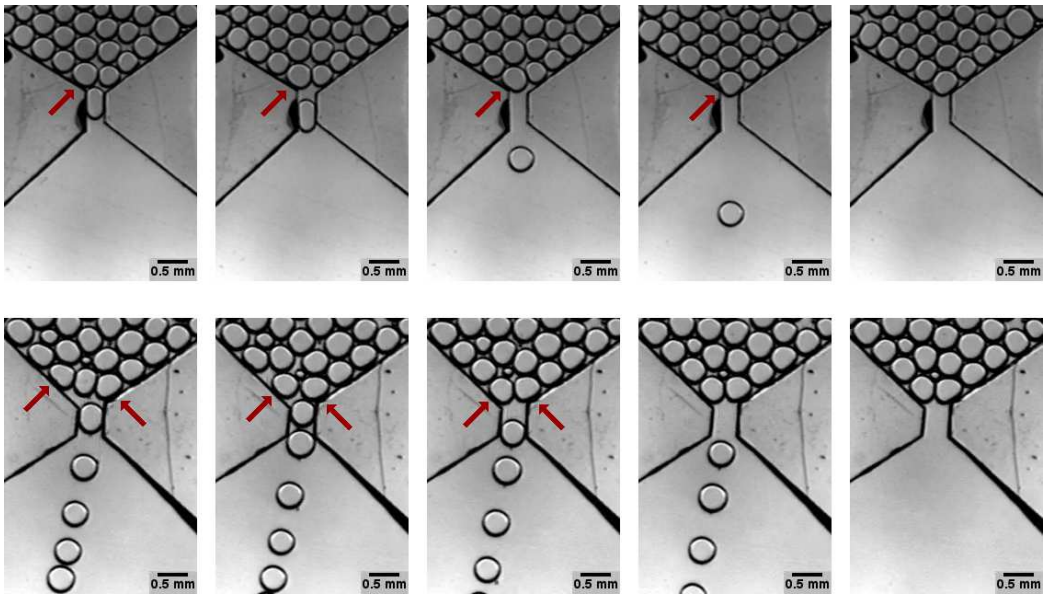

Figure 4.14: These images show two examples of clogging. The top row shows a situation where one droplet clogs at the hopper exit ($w/d = 0.81$). The bottom row shows a situation where two droplets form a small arch at the hopper exit ($w/d = 1.00$). The arrows indicate the droplet(s) that will clog the opening. For the top row, the images are each 10 s apart, except for the final image which is 50 s later. For the bottom row, the images are each 5 s apart, except for the final image which is 30 s later.

fit, and their data with gear-shaped particles had a decidedly non-sigmoidal shoulder [1], as shown in Fig. 4.13. Likewise Janda *et al.* used a different fit [55]. I also try exponential fit as shown in red dash line in Fig. 4.11. The fitting looks good but our sparse data are not sufficient to distinguish subtle differences in these fits, so we stick with the simple sigmoidal fit.

Fig. 4.14 shows two examples of clogged samples. The top case shows $w/d \approx 0.8$ and a situation where the influence of surface tension is weak enough that one droplet can deform and slip through. However, after that first droplet, the remainder clog. The bottom case shows a small "arch" of two particles that clog at $w/d \approx$

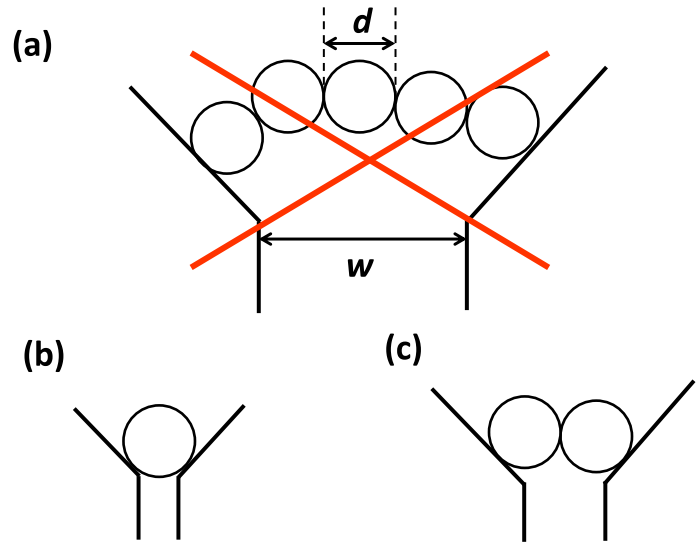

Figure 4.15: (a) Arch formation at the hopper exit in granular experiment [1].(b) and (c): two clogging cases without big arches formation at the hopper exit in emulsion system. (b) is corresponding to the top images and (c) is corresponding to the bottom images in Fig. 4.14.

1.0. Comparing with granular experiment that is shown in Fig. 4.15 (a) where big arch formation is the mechanism of clogging, this type of big "arch" has never been observed in our emulsion system. There always be only one or two droplets clogging at the hopper exit, as shown in Fig. 4.15(b) and (c).

4.4.3 Crystalline Effect

One interesting phenomena of clogging might be related to crystalline ordering effect. As shown in the top right image in Fig. 4.14, there are several droplets close to the hopper exit having the same size, which lead to a local crystalline structure. This could introduce more physics related to breaking a crystal. We also think that the asymmetry of the construction at the hopper exit could be a reason for crystallization

and the crystal structure makes clogging easier. As shown in Fig. 4.16, droplets can go through the middle hopper without clogging, while they clog at the opening of the first and third hoppers (from left to right). The detail constructions of these three hoppers are also shown in Fig. 4.16. The opening widths of these three hoppers are fairly similar($\approx 630\ \mu$m) but the right most hopper is mismatched more seriously than the other two. This gives us a sign that hopper mismatch leads to higher clogging probability. One speculation could be that the crystallization helps the droplets to form crystals at the hopper exit and thus more difficult for them to flow. If this is the case, the location and direction of the force line could be important during the process of breaking down a crystal. I propose the possible mechanism in Fig. 4.17. In specific, if the force chain is parallel to the boundary of a crystal, it is more difficult to break the crystal as shown in Fig. 4.17 (a). On the contrary, if the force chain is again the wall and goes across inside the sample, it could be easier to break the crystal as shown in Fig. 4.17 (b). However, this explanation is just a hypothesis that need further experiments to verify.

4.5 Discussion and Conclusion

We find that in our system of soft frictionless droplets, the probability of clogging in hopper flow is greatly reduced from prior published experiments that studied hard frictional particles [1, 55, 113]. In our experiments, we only see clogging with exit apertures significantly smaller than previously seen with hard frictional particles [49–51, 77, 102, 103]. We cannot separate the roles of softness and lack of friction for our particles merely from the experimental data. Our result of reduced clogging

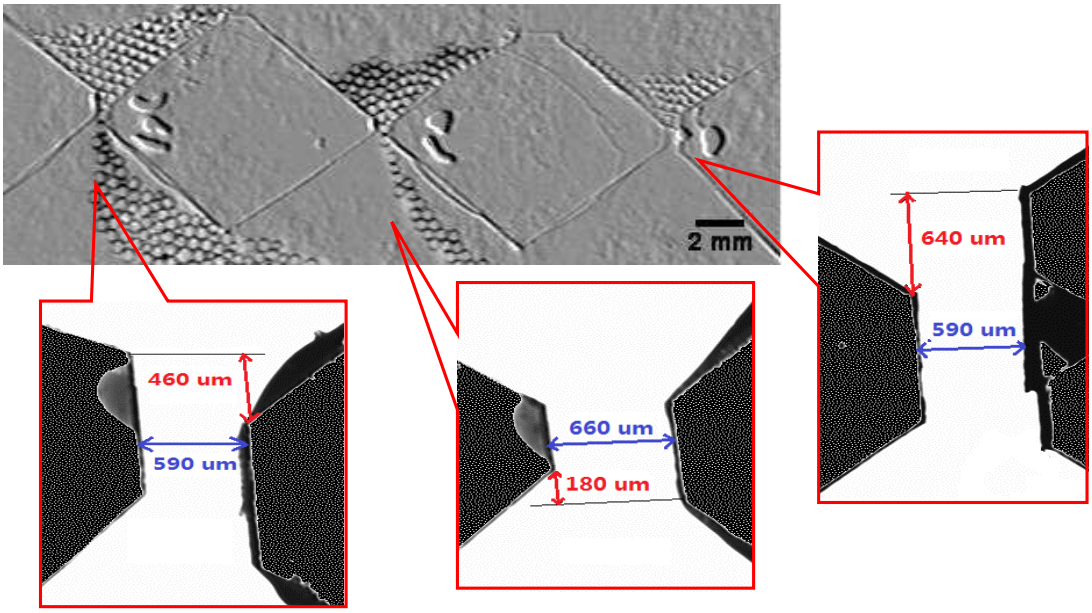

Figure 4.16: Constructions of three hoppers showing the effect of hopper mismatch. All three hoppers have similar hopper width ≈ 630 μm as shown in blue. But they have mismatch in different degrees, as shown in red. The middle hopper has the best symmetry. The right most hopper is mismatched to the largest degree and the droplets stop flowing.

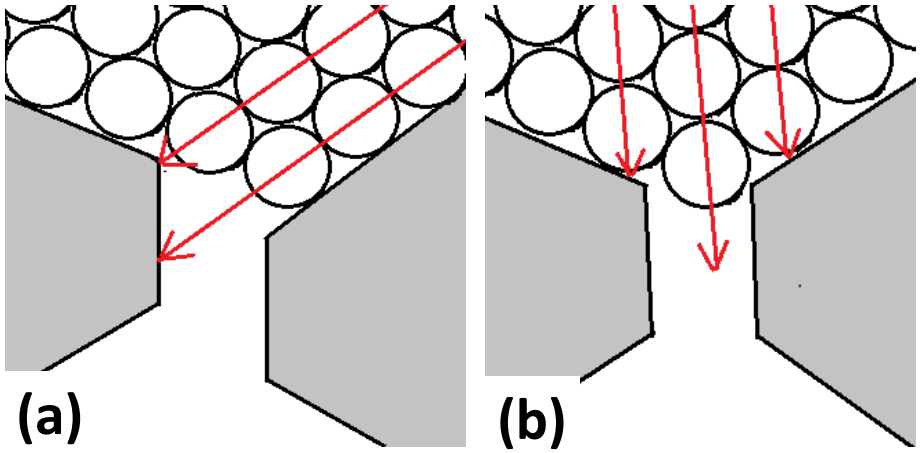

Figure 4.17: Force chain is (a) parallel to the boundary and (b) against the boundary and across inside the crystal.

qualitatively matches the trend seen by To *et al.* who found a lower clogging probability for smooth-surface disks compared to gear-shaped disks as shown in Fig. 4.13 [1]. In our experiment, our droplets cannot sustain long arches. This is despite the reduced influence of gravity due to buoyancy of the droplets and their slower motion due to viscous forces. However, the simulation work done by Eric Weeks shows that even frictionless droplets can form large arches when gravity is even smaller, which is effectively equivalent to increasing the stiffness of the droplets. The key is that, for an emulsion the surface tension must be high, or the gravity must be weak, to be able to form large arches that can clog the hopper. In our experiment, gravity is still high comparing with the surface tension, and essentially breaks large arches due to a mechanism similar to what is seen in Fig. 4.6, albeit with subtler droplet deformations.

The results with reduced gravity are the opposite of those seen in prior work that found reducing gravity prevented clogging [68]. In that work, the conclusion was that reducing the load on the arches at the exit would allow vibrations or other noise to destroy the arch [68, 120]. That is, the weight of the grains above the exit applies a compatible load that strengthens the arch formed from hard granular materials. In contrast, our soft particles are deformed by this load and thus the load can strengthen the arch (at low loads) or break the arch (at high loads). More significantly, we have no source of incompatible forces that disrupt a stable arch once formed, unlike the prior work [68]. For smaller droplets for which Brownian motion might play a role, it is possible that decreasing gravity would decrease clogging, the opposite of our present results for non-Brownian droplets.

Our results also contrast with centrifuge experiments of Dorbolo *et al.*, which found that clogging was uninfluenced by gravity [121]. These experiments do not have added vibrations, so provide a complementary view to Ref. [68]. The difference between these experiments and our work is likely explainable by their use of glass and steel beads. For glass beads, estimating their modulus as $E = 70$ GPa, density as $\rho = 2.6$ g/cm^3, and using their radius $R = 200$ μm, one can use the Hertzian contact model to estimate the deformation of a spherical particle due to the gravitational weight of the particles above. Assuming the imposed weight is approximately 10 times larger than the weight of an individual sphere, the deformation d of a glass bead under the maximum imposed gravity ($20g$) would be approximately $d/R = 10^{-5}$ for Ref. [121]. For our simulations under the same assumptions about the imposed weight, the expected deformation of droplets in the clogging arch is $d/R \approx 40g/F_0$, so 4×10^{-3} for our lowest value of g/F_0 (defining d as the overlap between two droplets). The simulation work has the $w/d \approx 3$ for the lowest $g/F_0 \approx 10^{-4}$. This suggests that we have not yet reached the hard particle limit yet, so it is not surprising to think that the experiments of Ref. [121] are in a low-gravity limit where gravity is unimportant for clogging. This suggests that there are opportunities to explore clogging using softer granular particles where gravity should have an observable influence on clogging.

Additionally, in the experiment, we find some interesting crystal effect near the mismatched hopper exit, which seems like a possible reason for an increase in clogging probability. However, this needs further study to draw any conclusion.

Overall, our results demonstrate that the flow of soft particles is qualitatively different from the case of hard particles. This potentially has implications for other

situations where particles have soft long-range interactions such as magnetic particles [109], merging traffic [122], and perhaps flowing bacteria [123].

Ideas for further study:

(1) Change hopper angle θ to see if the clogging probability changes in a similar way as observed in To's experiment (as shown in Fig. 4.12).

(2) Change the hopper shape. For example, change the flat straight boundary to a curved boundary, either concave or convex.

(3) Currently we hold the sample vertically at 90°. Tilt the sample at an angle less than 90° to use partial gravitational potential energy. This way we can use experimental result to verify the simulation results.

(4) Change the viscosity of the background fluid. For example, add glycerol into water to increase its viscosity.

(5) Make hopper chambers in a better control way and study the crystal effect as mentioned in Sec. 4.4.3 using monodisperse sample.

(6) The time window used to define clogging is crucial and it might be interesting to study its effect on the clogging probability results.

(7) For the emulsion flow like sand glass as shown in Fig. 4.8, more analysis on the flow rate could be done.

Chapter 5

Avalanches of Rearrangements in 2D Emulsion Hopper Flow

5.1 Introduction

Many slowly strained materials exhibit intermittent flow behavior: long still periods punctuated by rapid avalanches where material flows [35, 58–61]. Examples include diverse phenomena such as earthquakes [62, 63], general deformations of solids [64], stick-slip friction due to granular layers [65, 66], Barkhausen noise in magnetic materials [67], and sheep herded through constrictions [68]. More commonly, avalanches are seen in slow flows of athermal soft materials such as emulsions [58], bubble rafts [36], foams [60, 69–72], and granular materials [55, 73–77]. These soft materials typically have amorphous structure, necessitating that flow and rearrangements are disordered on a microscopic scale. The slow flow speed is a key feature: for example, a rotating drum experiment with sand inside demonstrated avalanches at

low rotation rates and smooth flow at high rotation rates [124]. For granular materials, static friction can prevent the material from flowing and can lead to avalanches. In systems composed of fluids such as foams and emulsions, stresses are supported not by static friction but rather surface tension, which resists the deformation of the bubbles or droplets.

Hopper flow is a useful case study for these types of flowing particulate materials. In this geometry (Fig. 5.1), the material starts in a wide channel but then exits the chamber through a narrow orifice. This is of industrial interest for storage of granular materials [51, 125] and has been long studied scientifically. For example, an early paper in 1929 examined hopper flow of various granular materials and observed that flow halted when the exit orifice diameter was less than about 4 particle diameters [50], which has been observed many times since [1, 49, 102, 111]. Subsequent work found that for small exit orifices, the flow rate fluctuates a fair bit as small arches form and break near the exit [52, 53]. For larger exit orifices, the flow rate is smooth and generally considered to be a simple function of the orifice size and various material parameters [49, 51, 102].

In this chapter, we present an experimental study of hopper flow using a quasi-two-dimensional emulsion. Details of preparing the emulsion system are in Chap. 2. The area fractions are all above jamming [69] ranging from $\phi = 0.83 - 0.99$, such that the droplets touch each other and are in many cases highly deformed by their neighbors. Our exit orifices are all small (3-5 droplet diameters across). We drive the flow with a pump, and given that our droplets are deformable, they cannot permanently jam at the exit. We see a range of flow behaviors. At the lowest flow rates, the flow pauses for

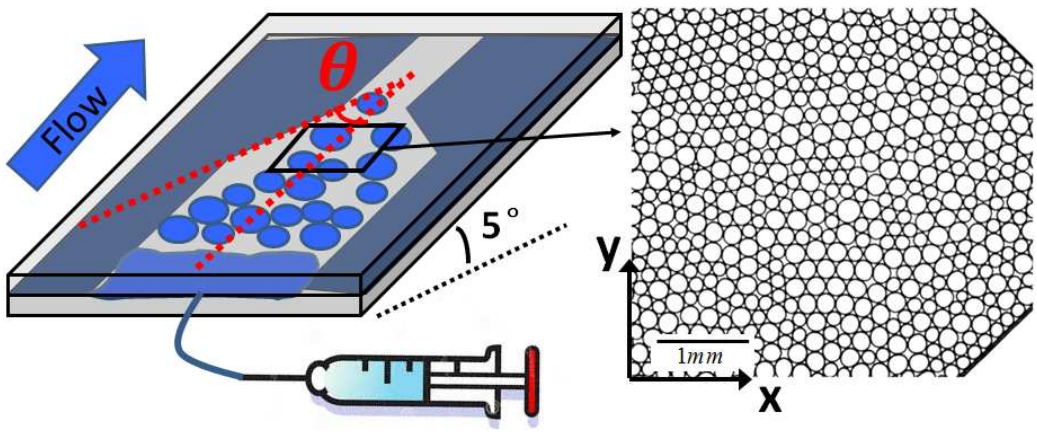

Figure 5.1: Schema of our sample chamber (left) and raw image of the emulsion flowing in the $+x$-direction (right).

long periods of time broken up by large avalanches of rearrangements. At the highest flow rates, rearrangement events are always occurring and droplets exit continuously. Intriguingly, the transition between the two flow behaviors occurs fairly smoothly as the flow rate is increased, and at moderate flow rates we see an intermediate type of flow behavior. Despite the range of area fractions we study, the area fraction does not seem to control the flow behavior.

5.2 Experimental Method

5.2.1 Samples and Sample Chambers

Our emulsions are mineral oil droplets in water using Fairy detergent (mass fraction 0.025) as a surfactant to prevent coalescence of the droplets [14, 87]. The droplets are produced using a standard co-flow micro-fluidic technique [81]. The radius polydispersity of our droplets made this way is 1% (standard deviation divided by mean).

To prevent droplets from organizing into crystalline arrays, for each experiment we make a bidisperse emulsion by mixing together two separate batches of monodisperse droplets at a volume ratio of about 1:1. While each individual batch of monodisperse droplets has a low polydispersity, there is some variability between batches. The mean diameter of the large droplets is 270 ± 50 μm and of the small droplets is 200 ± 40 μm, and the diameter ratios of the bidisperse mixtures we form are in the range $d_L/d_S = 1.5 \pm 0.2$.

In our experiment, we confine droplets between two 25 mm $\times$ 75 mm glass slides. The slides are separated by pieces of 100 μm transparency film sealed with epoxy. These pieces of film act as spacers and thus creating a gap between the slides. This gap ranges from 115 to 140 μm in different experiments. This range is mainly due to the different amount of epoxy applied when making each chamber. Nonetheless, within a given sample chamber, this gap is constant with variation less than 1.8% within any given sample chamber so the slides are parallel (the corresponding maximum angle between two slides is less than 1°). Sample chambers for which this was not true were discarded. While the gap thickness varies from experiment to experiment, our prior work found that the thickness was unimportant as far as the contact forces droplets exert on one another when they contact [14]. In all cases, the diameters of the oil droplets are chosen to be larger than the gap of the sample chamber. Thus, the droplets are squeezed between the two glass slides without overlapping to achieve a quasi-2D system.

The left panel in Fig. 5.1 shows the schema of the chamber. The pieces of film are cut to form a symmetric hopper channel with angle $\theta = 54 \pm 5°$ (see Fig. 5.1) and

opening width $0.7-1$ mm. The sample chamber is tilted at an angle $5\pm1^\circ$ relative to the horizontal, to use the buoyant force of the droplets to balance the viscous friction between droplets and glass slides. The buoyant force is due to the density difference between water and mineral oil ($\rho_{\text{water}} = 1.00$ g/cm^3, $\rho_{\text{oil}} = 0.83$ g/cm^3). First we load the emulsion into the sample chamber, and then behind the emulsion we add pure mineral oil. A syringe pump injects additional mineral oil into the chamber at constant flux rate to push the emulsion through the chamber and thus funnel the droplets through the hopper exit.

We use a microscope with a $1.6\times$ objective lens to image the system, focusing on the chamber mid-plane where the 2D droplet images are clearest. A CCD camera records the images in the region close to (0.5-2 mm away from) the hopper opening. Depending on the mean speed of the flow in a given experiment, the camera frame rate is between 0.2 and 2 images/second. This is sufficient to track the trajectory of each individual droplet using standard software[96], even at the maximum velocity $0.06\langle D\rangle$/s, where $\langle D\rangle$ is the mean diameter of the droplets. The right panel in Fig. 5.1 shows a typical raw image, in which we record hundreds of droplets within the field of view.

5.2.2 Control Parameters

One of our main control parameters is the area fraction ϕ occupied by oil droplets, as measured from our image analysis. ϕ is somewhat controllable by what we put into the sample chamber: ahead of time, we prepare bulk emulsion samples at different 3D volume fractions, and can add a sample at a higher or lower concentration. However,

due to difficulties loading the samples, it is not always certain that the final area fraction is equal to the bulk volume fraction. All our reported ϕ in this chapter are the measured values from the image analysis. We take a total of 45 data sets wit area fraction $0.83 \leq \phi \leq 0.99$ and pumping flux rate $0.0001 \leq F \leq 0.02$ ml/hr. Details of each experiment are listed in Table. 5.1 including measured area fraction ϕ, pumping flux rate F, hopper exit width, hopper angle, gap thickness, etc. From the post-processed images, we observe that ϕ has only minimal fluctuations during an experiment, with a relative standard deviation no more than 0.5%. These fluctuations are primarily due to the finite field of view, with ϕ changing when droplets flow in and out. In flowing suspensions of solid particles there can be a self-filtration effect [126], but we see no evidence of this (which would be signaled by a monotonic increase of ϕ). Additionally, we look for water flow relative to the emulsion droplets [127, 128] by adding tracer particles to the water for a few cases. In every case, the water flows at the same rate as the oil droplets. For example, in some situations, the oil droplets cease flowing for a period of time, and during those times the water is also seen to cease flowing. There is an additional possible systematic uncertainty for ϕ as the apparent size of each droplet depends on the illumination settings of the microscope. We keep these settings constant between each experiment.

The other main control parameter for our experiments is the flux rate F. For each experiment, F is set by a syringe pump and thus is constant at the pump. However, the observed flow velocity fluctuates. This is likely due to some compliance in the sample chamber, allowing sample to flow in slightly without having to flow out, and building up pressure until it is released by droplets flowing out. To simplify

the discussion, rather than focusing on flux, we use the experimentally measured quantity of the mean strain rate $\langle\dot{\gamma}\rangle$. $\langle\dot{\gamma}\rangle$ is defined and calculated as follow. x and y are defined using the coordinate system on the right panel in Fig. 5.1. For each droplet, we determine the trajectory of its center of mass, $[x(t), y(t)]$. Using a short time interval, we also determine its instantaneous velocity (v_x, v_y). For a given droplet, we consider the motion of it and its neighbors (defined as those droplets connected by a Delaunay triangulation of all the droplets). Using these data, the instantaneous strain rate of this droplet j is averaged over all neighbors:

$$\dot{\gamma}_j = |\langle \frac{v_x(j) - v_x(i)}{y_j - y_i} \rangle_i|, \tag{5.1}$$

where the subscript i indicates the ith neighbor of the reference droplet j, and the average is taken over all of the neighbors. The strain rate can be interpreted as the spacial gradient in y direction of the velocity in x direction; the gradients of the y velocity are smaller and accordingly we neglect them. The mean strain rate $\langle\dot{\gamma}\rangle$ of each data set is calculated by averaging over all droplets and all time.

5.3 Results and Discussion

We observe a wide range of flow behaviors as we vary F and ϕ for different experiments. For large F, droplets flow continuously and smoothly (referred as *smooth flow* cases in this chapter). For small F, we see avalanche-like flow (referred as *avalanche* cases). For intermediate flux rates F, we observe *intermediate cases* between these two flow patterns. As will be discussed below, we do not see any clear dependence of these flow patterns on the area fraction ϕ.

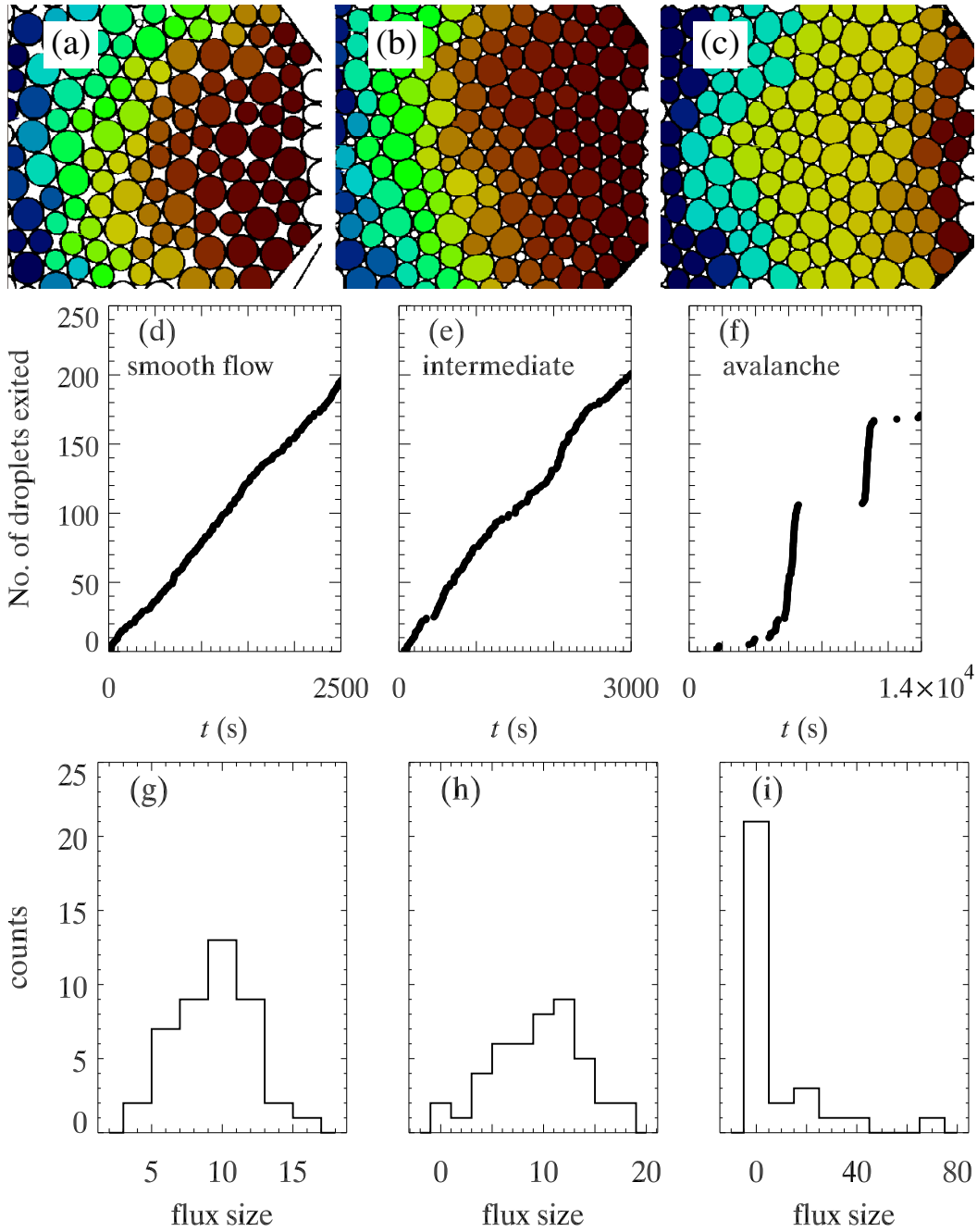

Figure 5.2: Description of the three flow behaviors. (a-c) Images of the samples at a particular time, with the color indicating the time when the droplet exits. The red droplets exit earlier and blue droplets exit later. The time ranges for the colors are (a) 1250 s, (b) 3000 s, and (c) 14000 s. (d-f) The number of droplets that have exited the hopper as a function of time. (g-i) Histograms of the number of droplets exiting the hopper within a short time window T, chosen such that the mean of the histogram is 10 droplets. The values of T are (g) 58 s, (h) 118 s, and (i) 529 s. The flow conditions are: (a,d,g) smooth flow, $\phi = 0.87$, $\langle\dot{\gamma}\rangle = 0.065$ s^{-1}. (b,e,h) Intermediate, $\phi = 0.96$, $\langle\dot{\gamma}\rangle = 0.02$ s^{-1}. (c,f,i) Avalanche, $\phi = 0.96$, $\langle\dot{\gamma}\rangle = 0.01$ s^{-1}.

We summarize these three flow behaviors in Fig. 5.2. The three pictures in Fig. 5.2(a)-(c) use color to show the time each droplet exits the hopper opening to the right. Red droplets exit the earliest, and blue the latest. The left picture is a smooth flow case, which shows a smooth gradient in color. The right one shows an avalanche case, where droplets have distinct groups of colors indicating that droplets exit the hopper in bursts. Note that the color scale of each plot corresponds to a different amount of time, as specified in the caption.

Figs. 5.2(d)-(f) quantify these pictures by showing the cumulative number of droplets that have exited the hopper as a function of time for our three flow cases. In the smooth flow case (d), the data form a smooth curve with a well-defined slope, showing that droplets exit the hopper continuously at a fairly constant rate. The intermediate case (e) shows fluctuations in the rate, although it is still fairly continuous. In avalanche case (f), there are stretches of time where no droplets exit, followed by discrete sudden flow events where many droplets exit within a short period of time, indicated by the vertical portions of the data in (f). Specifically, the first vertical line at $t \approx 6000$ s relates to all of the yellow droplets in (c) that exit at nearly the same time. Again, the existence of avalanches despite the constant flux set by the syringe pump shows that there is some compliance in the chamber, such that the pressure builds up before an avalanche.

Fig. 5.2(g)-(i) show the histograms of exiting flux. The exiting flux size is the number of droplets exiting during a time window T, with T chosen to make the mean flux size to be 10. The smooth flow case (g) has a Gaussian shape while the avalanche case (i) has a few rare but large events. To quantify this, the skewness

values for these distributions are (g) 0.15, (h) -0.03, and (i) 2.2 for smooth flow, intermediate, and avalanche cases respectively. Not surprisingly, the avalanche case has a large positive skewness, and this is generally true that all avalanche flow cases have positively skewed distributions. Given that the avalanche cases have very few events overall, our skewness data are noisy and we cannot resolve any clear trend in the skewness as a function of our control parameters. The general picture shown in Fig. 5.2(g)-(i) is clear, though, that avalanche cases have distributions with positive skewness and there is a trend toward more symmetric distributions with skewness ≈ 0 as F increases.

To better quantify the difference of these flow behaviors, we introduce a method focusing on the temporal behavior of the flow. In avalanche cases, discrete sudden flow events are separated by time intervals where droplets barely move and no droplets exit the hopper. Accordingly, we define the time between two successive droplets exiting the hopper as the interval Δt. As shown in Fig. 5.3, we set t_1 as the time when the black droplet exits the hopper, t_2 as the time when the next droplet (in red) exits, and then $\Delta t = t_2 - t_1$.

It is apparent in the plots in Fig. 5.2(d-f) that the distributions of Δt are different for the smooth flow and avalanche cases. In smooth flow, the values of Δt are small and do not fluctuate much. In the avalanche case, Δt is sometimes small (vertical portions, where many droplets exit over a short time interval) and sometimes large (horizontal stretches, where a long time passes between one droplet exiting and the next). Figure 5.4 shows the probability distribution functions for Δt for the same three data sets shown in Fig. 5.2. The smooth flow case shown in Fig. 5.4(a) is

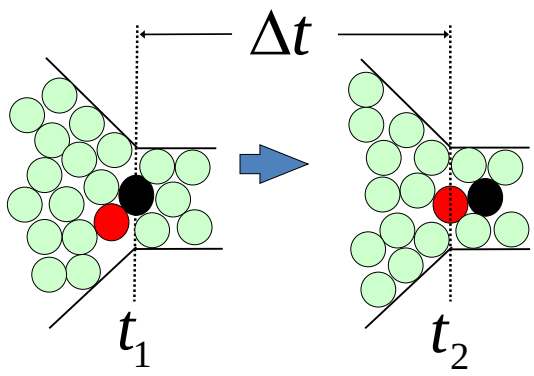

Figure 5.3: Schema of the definition of interval Δt. The left figure is at time t_1 when the black droplet exits the hopper. The right figure is at time t_2 when the red droplet exits the hopper.

well fit to an exponential, as shown by the dashed red line; note this is a semi-log plot. The exponential fit $P(\Delta t) \sim e^{-\Delta t/\tau}$ defines the mean time between events τ, and the fit suggests that the time between events follows a Poisson process, where events occur continuously and independently with a constant mean rate. The avalanche case shown in panel (f) is well fit to a power law, as shown by the dashed red line; note this is a log-log plot. The fit in this case is given by $P(\Delta t) \sim \Delta t^{-\alpha}$ with $\alpha = 1.6$, and the power law regime covers more than 2 decades in Δt and more than 4 decades in probability. The tails correspond to the long periods of time where droplets barely move. The intermediate case can be fit with either an exponential in panel (c) or a power law in panel (d); neither fit is perfect. The exponential fit (c) fails for the largest Δt while the power law (d) is not adequate to describe the small Δt region. Although, these failures may be related to the portion of data used for the fit: it is equally possible this distribution is a power law with an exponential cutoff at large Δt.

If we normalize the interval Δt by the observed mean interval $\langle \Delta t \rangle$ and plot

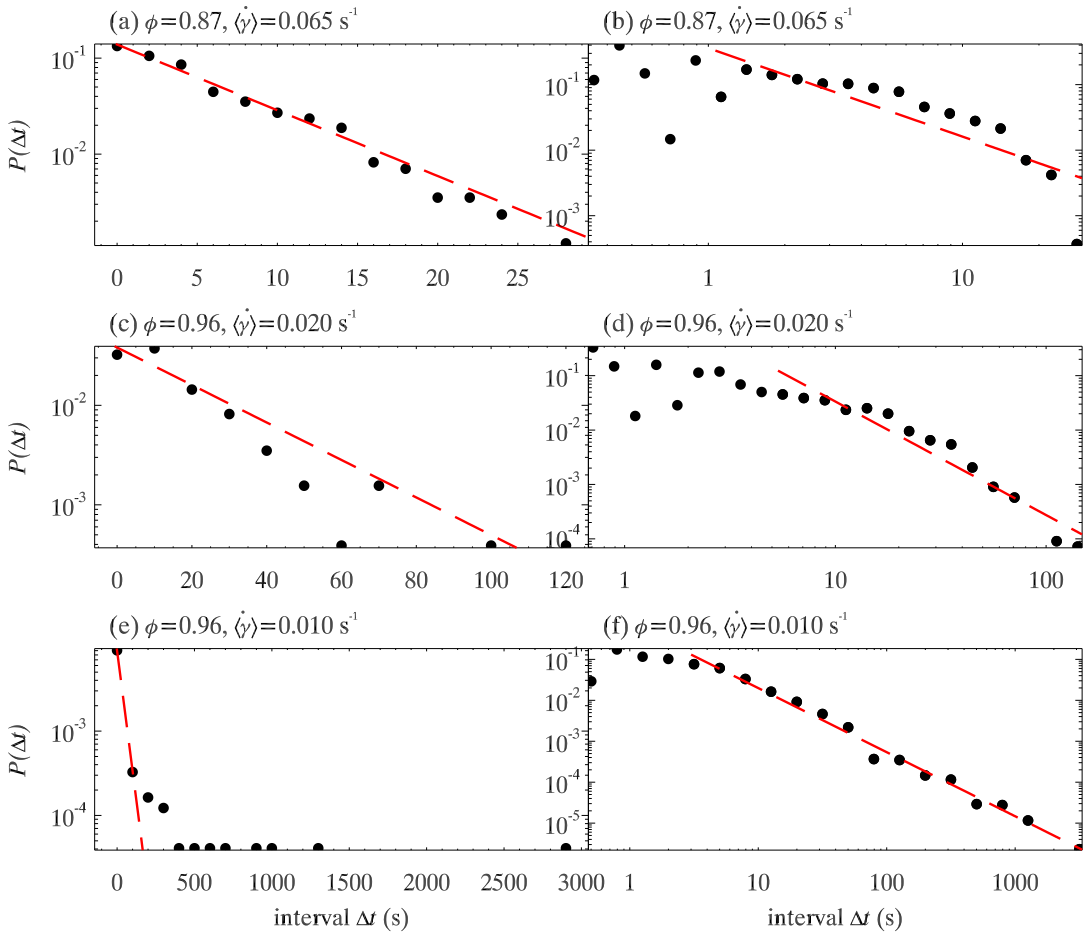

Figure 5.4: Typical examples of three types of probability distribution functions of interval Δt(s). The left column (a,c,e) are plots in log-linear scale and the corresponding red dash lines are exponential fits; The right column (b,d,f) are plots in log-log scale and the corresponding red dash lines are power law fits. Each row is for the same experiment and the three experiments are corresponding to that in Fig. 5.3. The area fraction ϕ and mean strain rate $\langle\dot{\gamma}\rangle$ are as indicated in each panel.
In (a) the line shows an exponential fit $P(\Delta t)\sim e^{-\Delta t/\tau}$ with $\tau = 6.3$ s; In (b) the power-law fit does not really work. In (c) the read dash line is an exponential fit with $\tau = 12.7$ s and in (d) the straight line is a power-law fit $P(\Delta t)\sim\Delta t^{-\alpha}$ with $\alpha = 2.1$. In (e) the line is an exponential fit but it is obviously not working; while in (f) the red dash line is a power-law fit with $\alpha = 1.6$.

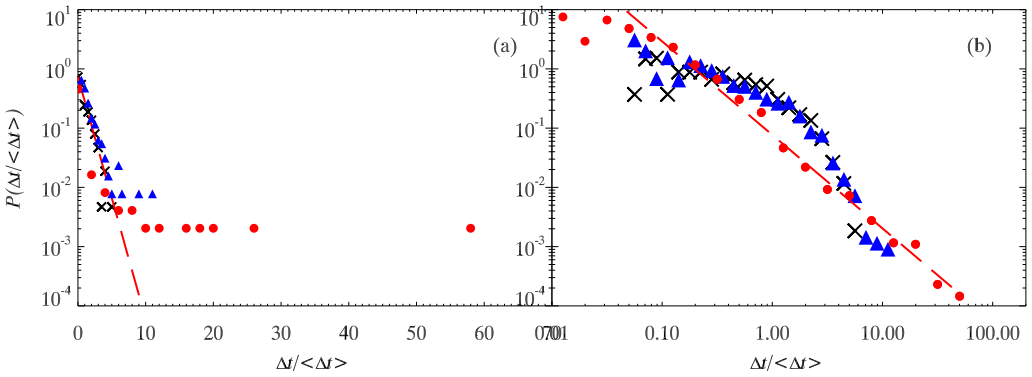

Figure 5.5: Typical examples of three types of probability distribution functions of $\Delta t/\langle\Delta t\rangle$. Red circle: corresponding to the power law in Fig. 5.4; blue triangle: intermediate case; black cross: exponential fitting. (a) is a semi-log plot and the red dash line is the same exponential fitting as that in Fig. 5.4(a) for smooth flow case; (b) is a log-log plot and the red dash line is the same power-law fitting as that in Fig. 5.4(f).

the probability distribution function of $\Delta t/\langle\Delta t\rangle$ for these three cases, we can have a clearer comparison between them. In Fig. 5.5, (a) is a semi-log plot, where the exponential fit works pretty well for the smooth flow case (black cross) and the other two cases are deviate from the straight dash line. Especially for the avalanche case (red dot), there are data points $\Delta t/\langle\Delta t\rangle$ >50, which is not observed in the smooth flow case. (b) is on a log-log scale, where the power-law fit is for the avalanche case (red circle) and the other two cases are obviously different from the straight dash line. Therefore, the smooth flow and avalanche cases have two distinctively different probability distribution functions of $\Delta t/\langle\Delta t\rangle$, while the intermediate case is difficult to use either exponential or power-law for a good fit.

When we expand this plot to all the data, as shown in Fig. 5.6, some data definitely deviate from the exponential fitting in (a) and the others clearly deviate from power-law fitting in (b). The two fitting curves (red dash lines) are the same as that in

Fig. 5.5 correspondingly. It is challenging to separate the data sets in this scaled plot because of the noise. As we will discuss later that even for all the power-law cases, the exponent is different and thus it is very hard to separate different cases in this plot. Therefore, I use judgement on which fitting is the best for the shape of the probability distribution function of Δt for each one of the 45 experiments by eyes. There are cases that are obviously exponential or power-law like Fig. 5.4(a) and Fig. 5.4(c), for example. I would be 100 percent confident to classify them into exponential or power-law categories. But there are cases that are around the boarder of power-law and intermediate cases. Roughly speaking, if there are more than 50% of the data points in the probability distribution plot are aline with the fitting curve, it will be classified to be one of the two cases: exponential or power-law. Take a hard-to-tell example, Fig. 5.4(c) have 3-4 data points way off the fitting line and thus hard to say it is exponential. And, (d) have roughly half data points way off the fitting line and thus barely make it a power-law case. Therefore, it would belongs to the intermediate case. Admittedly, there is artificial error using this approach but this is one method to our best knowledge to classify different cases. Of course, the transition seems fairly smooth with all the intermediate cases filling the gap between two distinct flow behavior.

In our experiments we have varied both ϕ and flux rate. For each experiment, we use the shape of $P(\Delta t)$ to describe its flow behavior. I put two graphs Fig. 5.7 and Fig. 5.8 here to show the phase diagram of fitting patterns. Fig. 5.7 is in terms of area fraction ϕ and mean velocity of the droplets ($\langle D \rangle$/min). The mean velocity is a direct reflection of the control parameter flux rate F. However, it is not dimensionless

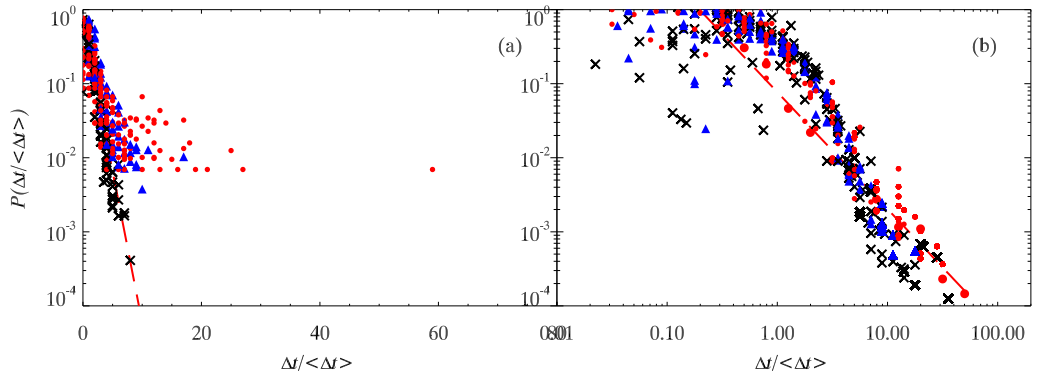

Figure 5.6: Probability distribution functions of $\Delta t/\langle\Delta t\rangle$. Red circle: power law; blue triangle: intermediate case; black cross: exponential fitting. (a) is a semi-log plot and the red dash line is the same exponential fitting as that in Fig. 5.5(a); (b) is a log-log plot and the red dash line is the same power-law fitting as that in Fig. 5.5(b).

and has dependence on length scale. To further reduce the dimension, I tried to use mean strain rate $\langle\dot{\gamma}\rangle$ (1/s) instead of mean velocity. And, $\langle\dot{\gamma}\rangle$ also has more physical meaning that will be discussed in Sec. 5.4. Therefore, the discussion will focus on Fig. 5.8.

There is no obvious trend with ϕ, but more clearly a transition from avalanche flow (red circles) to avalanche flow (black cross) with increasing $\langle\dot{\gamma}\rangle$. Note that the judgment about the best fitting function is done by eye. The quality of each fit depends on which range of data is used for the fit, and while we have tried several ways to approach the fitting procedure more systematically, none seem satisfactory for the intermediate cases, and none affect the appearance of Fig. 5.8 in any substantial way. As mentioned above, I have tried to our best knowledge to keep the classification criteria consistent across different experiments. Even with the same set of data, choosing different range for the fitting will give us different fitting parameters. This is why we have the error bars in Fig. 5.9.

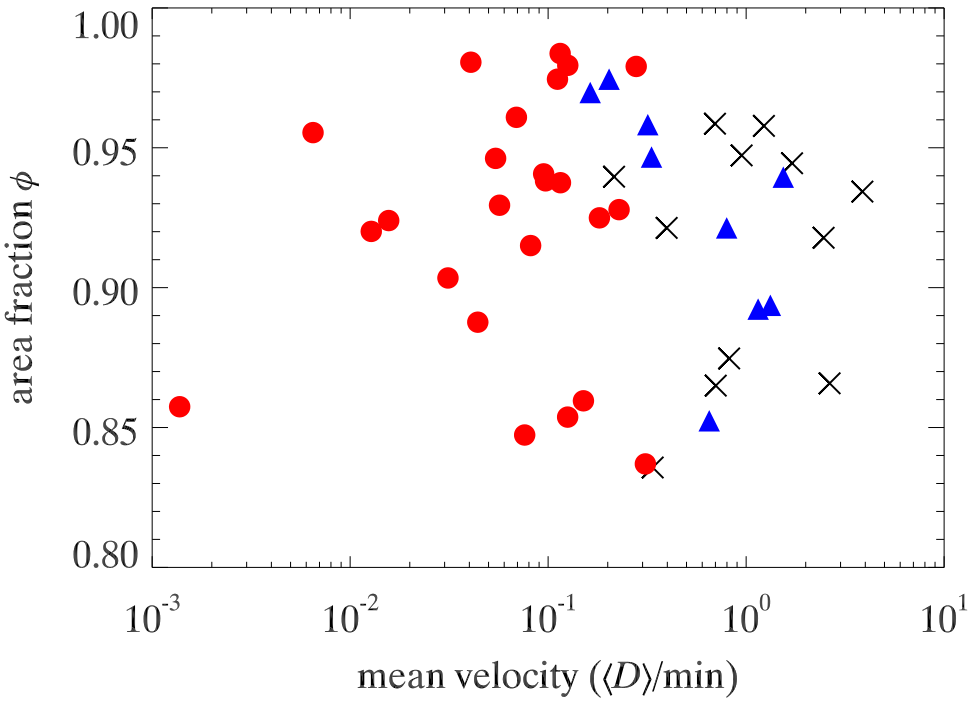

Figure 5.7: Phase diagram of fitting patterns of $P(\Delta t)$ in terms of area fraction ϕ and mean velocity ($\langle D \rangle$/min). Red circle: power law; blue triangle: intermediate; black cross: exponential.

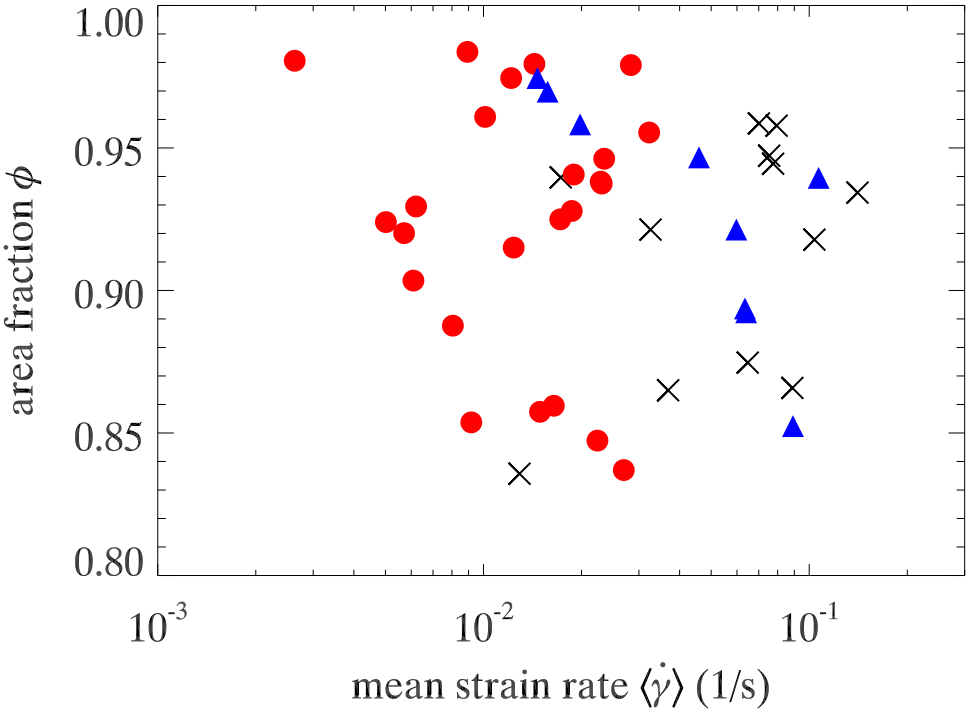

Figure 5.8: Phase diagram of fitting patterns of $P(\Delta t)$ in terms of area fraction ϕ and mean strain rate $\langle\dot{\gamma}\rangle$. Red circle: power law; blue triangle: intermediate; black cross: exponential.

The phase diagram of Fig. 5.8 is perhaps unsatisfying as the intermediate cases (blue triangles) are mixed in with the other two cases. However, by ignoring ϕ and focusing only on the flow rate dependence, the data become more unified. In particular, Fig. 5.9(a) shows the relation between the power law exponent of $P(\Delta t)$ and $\langle\dot{\gamma}\rangle$. The power exponent α increases as the mean strain rate increases. Even when the power law fit is not perfect (triangles), the data still follow the general trend started by the well-fit power law cases (circles). Smaller values of α indicate a broader distribution, where the large Δt events are more significant: these are the avalanche cases with long pauses between short bursts when many droplets exit. This is similar to previous experimental studies of sheared granular materials, where they have power law distributions of various stick-slip event properties including forces, energy, and avalanche sizes [15, 28, 75, 92, 129, 130].

To consider the exponential cases, we note that the exponential fitting parameter τ corresponds to the mean interval. Accordingly, in Fig. 5.9(b) we compute $\langle\Delta t\rangle$ for every experiment (no matter the distribution shape) and see that this decreases as mean strain rate $\langle\dot{\gamma}\rangle$ increases. This is plausible since the strain rate is bigger for higher flow velocity and thus droplets exit faster, which leads to small mean interval. Note that for those cases in Fig. 5.9(a) with $\alpha < 2$, it is problematic to define $\langle\Delta t\rangle$ since the mean of a power law distribution with $\alpha < 2$ is infinite. Thus, our finite values of $\langle\Delta t\rangle$ merely reflect the finite amount of data. It is plausible that the power law distributions may well have some cutoff at very large Δt. To an extent, the relationship shown in Fig. 5.9(b) is trivial by dimensional analysis: $\langle\Delta t\rangle$ and $\langle\dot{\gamma}\rangle^{-1}$ have dimensions of time. The dashed red line in Fig. 5.9(b) is a power law

fit with exponent -1.2, fairly close to the -1 suggested by dimensional analysis. The different exponent, and the reason the data do not completely collapse, is that the two quantities are different averages: in general $\langle x \rangle \neq \langle x^{-1} \rangle^{-1}$ and in specific $\langle \Delta t \rangle$ focuses on droplets exiting whereas $\langle \dot{\gamma} \rangle$ focuses on the behavior of all of the droplets everywhere, averaged over both time and space.

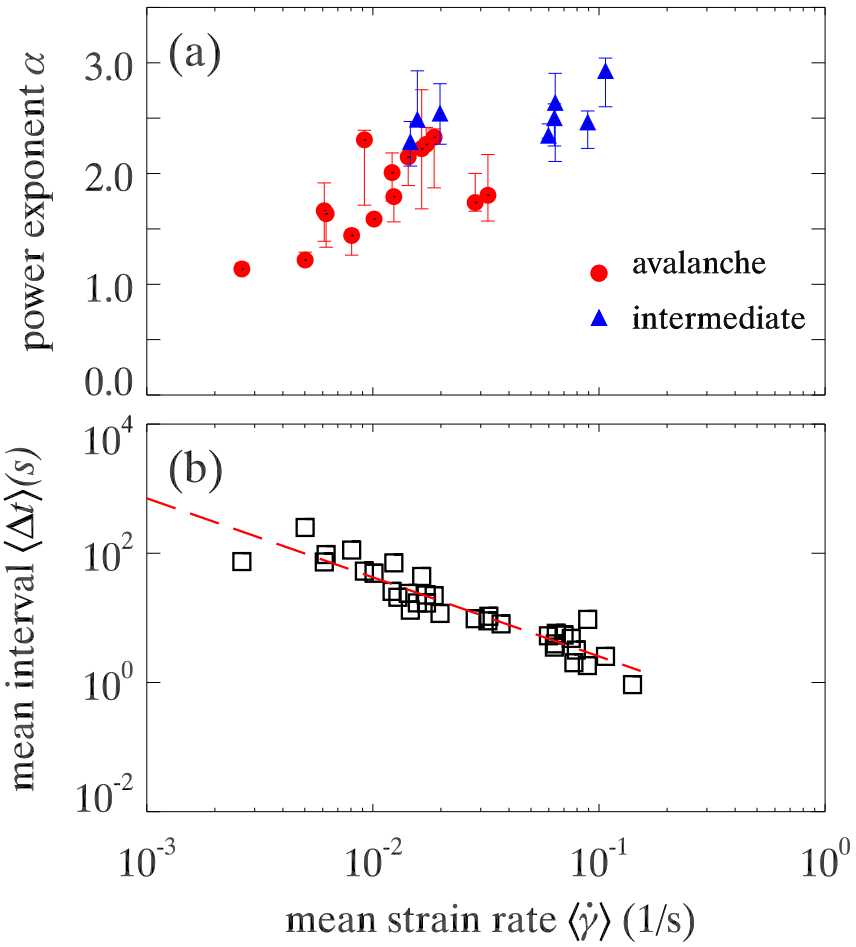

Figure 5.9: (a) The power law exponent α as a function of mean strain rate $\langle \dot{\gamma} \rangle$. For the power law fits, only data in the tail are used for the fit. Different choices of the minimum Δt used for the fit give rise to different values of α, reflected in the error bars shown here. (b) Mean interval $\langle \Delta t \rangle$ as a function of $\langle \dot{\gamma} \rangle$. The dashed line is a fit with slope of -1.2.

Table. 5.1 is a list of experimental parameters and measured variables for each of the 45 experiments.

- ϕ is the measured area fraction.

- F (ml/hr) is the pumping flux rate.

- $\langle\dot{\gamma}\rangle$ (1/s) is the measured mean strain rate.

- $\langle\Delta t\rangle$ (s) is the mean interval, where Δt is defined in Fig. 5.3.

- α is the power law fitting exponent for the interval distribution, same as that in Fig. 5.9 (a). Some of the data sets do not have fitting exponent because they are exponential distribution corresponding to the smooth flow cases.

- $w(\mu\text{m})$ is the hopper exist width.

- θ is the hopper angle indicated in Fig. 5.1. Given that the hopper shape spacer is cut manually, the imperfection leads to the slight difference in the two angles and thus there are two angles in the table for this column.

- $h(\mu\text{m})$ is the gap thickness of the chamber.

One chamber is missing and thus no hopper size data in the table.

5.4 Conclusions

We have demonstrated that in a single experimental geometry, we see behaviors changing from clear avalanches to smooth continuous flows as we increase the mean flow rate by a factor of 100. We quantify these behaviors by examining the distributions of times Δt between subsequent droplets exiting the hopper. Intriguingly, the transition in the flow behaviors is somewhat smooth as we increase the flow rate: the power law exponent characterizing the tails of $P(\Delta t)$ smoothly varies as the flow rate

increases past the point where a power law no longer adequately describes the data. One possibility is that at any flow rate, the distribution $P(\Delta t)$ may be describable by a power law with an exponential cutoff, and this cutoff may smoothly move to smaller Δt as the flow rate increases. However, the data we have for the intermediate cases [such as shown in Fig. 5.4(b)] are hard to interpret in the tails, and so it is difficult to resolve this question. The rate dependence of our observations is consistent with prior studies of athermally sheared 2D amorphous solids which demonstrated rate dependence [32, 47, 73, 131–134]. A recent simulation [135] based on Durian's 2D bubble model [69] predicted a similar trend for the flow behavior as strain rate increases. However, this study also found a dependence of the transition on area fraction, which we do not see. It is possible this is due to different flow geometries (a simple shear flow in the simulation, as compared to our hopper flow). The dependence on velocity is also displayed in experimental studies of sheared granular materials, where friction plays a key role [65, 66]. For hopper flow in granular experiments, the presence of static friction can make jamming and clogging obvious, where stress-supporting solid arches form across the exit [1]. In addition to static friction, such experiments are also driven by a constant force (gravity), whereas in our experiments the syringe pump increases the pressure until flow occurs, and so no arches can persist indefinitely.

The transition from avalanche to smooth flow happens around $\langle\dot{\gamma}\rangle \approx 0.02$ s^{-1}, indicated in Fig. 5.8. While we use mean strain rate to indicate each data set, actually the strain rate is spatially inhomogeneous. Within the imaged field of view, $\dot{\gamma}$ near the hopper exit can be 5 to 14 times bigger than the mean strain rate $\langle\dot{\gamma}\rangle$. Thus at the hopper exit using this local $\dot{\gamma}$, the transition point is $\dot{\gamma} \approx 0.1$ s^{-1} to 0.28 s^{-1}. The

inverse of this gives us a time scale $\tau_\gamma = 1/\dot{\gamma}$ about 3.6 to 10 seconds. τ_γ is the time for the system to strain by 1, which microscopically can be viewed as the time for one droplet to slide past a neighboring droplet. In a 2D system, the simplest topological rearrangement is the neighbor exchange of a group of four droplets, known as a T1 event [72, 87]: two droplets that are neighbors move apart, and between them two droplets that were not neighbors before move together and become neighbors. The time scale of a T1 event τ_{T1} in our system is a few seconds [87]. This is determined from the mean structural relaxation time based on the change of local stress field around a T1 event [24]. So, for fast flow rates in our experiment, a rearrangement event near the hopper exit which allows one droplet to exit may not be fully completed before the next rearrangement happens, allowing for substantial cross-talk between given events [87]. At slower flow rates, individual events can be less correlated, allowing fewer droplets to exit at a time, until the stress builds up and is released in a large avalanche event where many rearrangements happen nearly simultaneously. In our intermediate cases, it may be that in some moments rearrangement events occur close enough in space and time to influence and enhance each other, whereas in other moments events are more individual; some evidence of this has been seen in simulations of 2D foam flow [136] and other systems [132].

One possible concern is around whether there is random pinning of droplets here and there, which resist the flow and leads to avalanche. By looking at time averaged raw image, no droplet is anchoring on the plates (data not shown in the dissertation). This is at least saying that if even there is pinning or adhesion of the droplets to plates, the pinning force is not strong enough to hold back the flow and in fact the

contact forces greatly exceed the pinning force.

In summary, we see that the flow of an emulsion through a hopper can vary from avalanche-like to continuous. The transition between these behaviors is not abrupt, but rather a continuous function of the flow rate. At the lowest flow rates, the power law exponent we observe approaches $\alpha = 1$, showing that the flow has extremely long quiescent intervals in between the avalanches. The decrease of the power law exponent with decreasing flow rate [Fig. 5.9(a)] suggests that even with these slow flows, we are not in a quasi-static limit, in agreement with a prior study of slowly sheared bubble rafts [137]. In this simple limit where the strain rate approaches zero, the flow is not simple, but rather dominated by the rare intermittent avalanches.

Furthermore, shear banding is a common phenomenon observed in various shear flow of materials with granularity.[32, 41, 47, 133, 138–142] Based on the velocity profile (no data shown in this chapter), no shear localization observed in our system though, which is similar to a bubble raft experiment [37]. The reason could be its high inhomogeneity in the strain rate field with the hopper shape geometry that brings more complexity (comparing with simple shear or Couette cell) and the lack of friction that leads to different energy dissipation mechanism (comparing with granular materials). These differences could shed light on the importance of local stress field. Therefore, essentially all of the results point to the need for measurements of the interaction between droplets. Future experiment work is planned that will use the developed technique in our lab [14] to measure the forces with a high level of accuracy, which is comparable to the stress measurement in granular systems with photoelastic disks. With force information, the connection between the topological rearrangements

of individual droplets and the macroscopic flow properties of emulsions would be better understood.

	ϕ	F(ml/hr)	$\langle\dot{\gamma}\rangle$(1/s)	$\langle\Delta t\rangle$(s)	α	$w(\mu$m)	θ	$h(\mu$m)
1	0.93	0.02	0.14	0.93	-	-	-	-
2	0.94	0.01	0.077	2.02	-	-	-	-
3	0.94	0.005	0.017	16.94	-	-	-	-
4	0.89	0.01	0.063	3.53	2.50	857	54.6°,54.7°	124.9
5	0.87	0.02	0.089	1.83	-	857	54.6°,54.7°	124.9
6	0.86	0.005	0.037	8.06	-	857	54.6°,54.7°	124.9
7	0.89	0.01	0.064	3.96	2.64	857	54.6°,54.7°	124.9
8	0.87	0.005	0.065	5.78	-	857	54.6°,54.7°	124.9
9	0.92	0.02	-0.10	1.70	-	857	54.6°,54.7°	124.9
10	0.94	0.01	0.11	2.53	2.93	857	54.6°,54.7°	124.9
11	0.92	0.005	0.060	5.27	2.35	857	54.6°,54.7°	124.9
12	0.95	-0.01	0.075	4.81	-	857	53.8°,56.7°	124.9
13	0.96	0.001	0.032	9.00	1.80	873	51.1°,57.3°	141.6
14	0.96	0.001	0.010	49.04	1.59	873	51.1°,57.3°	141.6
15	0.96	0.005	0.070	5.43	-	873	51.1°,57.3°	141.6
16	0.96	0.002	0.020	11.70	2.55	873	51.1°,57.3°	141.6
17	0.96	0.01	0.079	3.17	-	873	51.1°,57.3°	141.6
18	0.92	0.002	0.033	10.58	-	873	51.1°,57.3°	141.6
19	0.92	0.001	0.017	22.62	2.26	873	51.1°,57.3°	141.6
20	0.98	0.002	0.014	23.95	2.15	1123	47.9°,49.7°	132.2
21	0.98	0.001	0.0026	74.49	1.14	1123	47.9°,49.7°	132.2
22	0.98	0.001	-0.0089	25.19	1.87	1123	47.9°,49.7°	132.2
23	0.97	0.003	0.016	17.02	2.49	1123	47.9°,49.7°	132.2
24	0.97	0.002	0.012	25.68	2.01	1123	47.9°,49.7°	132.2
25	0.97	0.004	0.015	13.16	2.29	1123	47.9°,49.7°	132.2
26	0.98	0.005	0.028	9.714	1.74	1123	47.9°,49.7°	132.2
27	0.94	0.002	-0.023	30.51	1.60	776	59.5°,55.6°	130.9
28	0.95	0.001	-0.023	45.25	1.64	776	59.5°,55.6°	130.9
29	0.95	0.01	-0.046	7.70	2.53	776	59.5°,55.6°	130.9
30	0.94	0.004	-0.023	22.73	1.60	776	59.5°,55.6°	130.9
31	0.94	0.002	-0.019	28.58	1.88	776	59.5°,55.6°	130.9
32	0.86	0.001	-0.015	72.46	1.86	776	59.5°,55.6°	130.9
33	0.85	0.001	-0.022	46.50	1.49	776	59.5°,55.6°	130.9
34	0.84	0.01	-0.027	11.30	2.07	776	59.5°,55.6°	130.9
35	0.84	0.005	0.013	20.83	-	776	59.5°,55.6°	130.9
36	0.86	0.001	0.016	43.81	2.22	776	56.3°,58.3°	147.3
37	0.85	0.0005	0.0092	52.91	2.30	776	56.3°,58.3°	147.3
38	0.85	0.01	0.089	9.47	2.47	776	56.3°,58.3°	147.3
39	0.90	0.0002	0.0061	73.49	1.66	776	56.3°,58.3°	147.3
40	0.92	0.0001	0.012	71.08	1.79	776	56.3°,58.3°	147.3
41	0.93	0.001	0.0062	95.52	1.64	776	56.3°,58.3°	147.3
42	0.92	0.0005	0.0057	368.78	0.97	571	50.9°,51.2°	131.6
43	0.92	0.0002	0.0050	251.04	1.22	571	56.3°,58.3°	131.6
44	0.93	0.002	0.019	22.11	2.33	571	56.3°,58.3°	131.6
45	0.89	0.001	0.0081	112.29	1.44	571	56.3°,58.3°	131.6

Table 5.1: Details of the 45 experiments in this chapter. Description in text.

Chapter 6

Dynamic Response to Local Perturbations

6.1 Introduction

The flow of amorphous materials have shown rich dynamics in various geometries including sand, foam, emulsion and granular materials [87, 142]. In emulsion system, where there is no static friction, the response of the system to a local perturbation is interesting but unknown. Our perturbation is introduced by injecting an inflating droplet into a quasi-two-dimensional emulsion. The flow fields of our system have nice macroscopically smooth profiles, which is the same as the flow profile of a simple incompressible fluid, though jammed amorphous materials usually do not show ordinary flow dynamics as simple fluid does [1, 2, 44, 143, 144]. However, for amorphous materials, microscopically the flow fields could be disordered with the phenomena observed by prior work like shear transformation zones, non-affine rearrangements,

and dynamical heterogeneities [46, 47, 87, 143–148]. We examine this in a simple geometry where the mean flow is quite well defined but where we observe fluctuations due to the discreteness of the particles. The well defined mean flow is not always true for our system if we use different geometries. For example, if we use emulsion pipe flow, the mean flow will not always be plug flow but depends on area fraction ϕ. Surprisingly, we do not see dependence of the dynamic response on the ordering of the system. It does not matter if it is strongly disordered (bidisperse) or weakly disordered (monodisperse with crystal grains and defects).

The study in this chapter is originally motivated by a previous work on the response of a granular material to local perturbations [2]. Their key finding is that the spatial ordering of the particles is a key factor in the force response. As shown in Fig. 6.1(b), a point force is applied on top of a 2D granular packing of photoelastic pentagons and the bright region shows the force chains due to both gravity and the applied external force. Fig. 6.1(c) is the force response to the point force, which is obtained by taking away the background forces due to gravity. The factor of spatial ordering and the idea of local perturbation to amorphous materials are interesting. A similar but different model system, emulsion, is well developed in our lab. These lead to the idea of producing local perturbation in emulsion system and the question how our system would respond. However, there are several main difference between our experiments including:

(1) They use granular materials with static friction while I use emulsion that are deformable and frictionless.

(2) They use point force applied on the side of the sample as the source of local

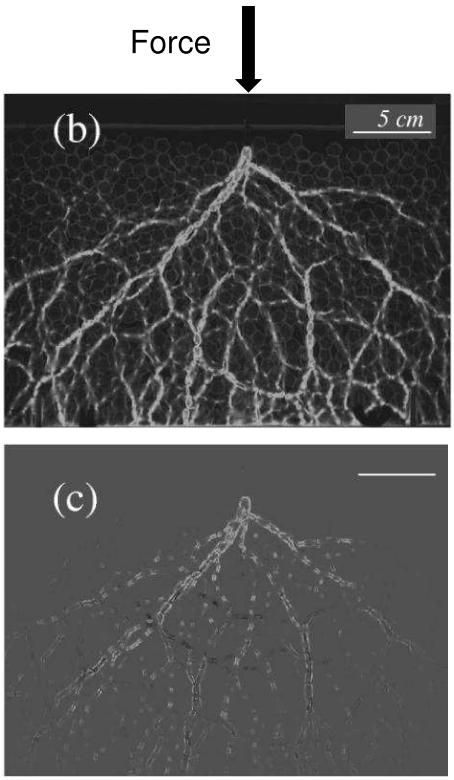

Figure 6.1: Images for 2D photoelastic pentagons showing (b) The combined force response to gravity and a point source. (c) The response to only the point force. (Reprinted figure with permission from [Junfei Geng *et al.*, Phys. Rev. Lett. 87, 035506, July 2001.] Copyright (2001) by the American Physical Society. License Number: 3814460774089)

perturbation while I use an inflating droplet inside the sample.

(3) Their particles are not moving during the force exertion and my droplets are moving during the inflation. So, their main analysis is focused on the force distribution and propagation. And, my study is about dynamic response.

In this chapter, we experimentally study the dynamic response of a quasi-two-dimensional emulsion to an inflating droplet. Our area fractions range from $\phi =$

$0.77 - 0.99$, such that the droplets are in most cases in contact with one another and are in many cases highly deformed. As will be shown, there is no dependence of the average flow behavior on distance to the inflating droplet, or on polydispersity or packing fraction of the emulsions. However, the fluctuation of velocity increases as the packing fraction gets further above jamming regardless of the polydispersity of emulsions.

6.2 Experimental Methods

6.2.1 Samples

Our mineral oil droplets are produced using a standard co-flow micro-fluidic technique (details are mentioned in Sec. 2.1 and Sec. 2.2). We are interested to see how ordered and disordered structure might make a difference, so we pick two distinct types of samples to study. One is composed of monodisperse droplets that can pack into crystalline regions and the other type is bidisperse packing, which has two different sizes of droplets to prevent them from organizing into crystalline arrays. The mean 2D diameter of the monodisperse droplets is $\langle d \rangle = 138 \pm 2$ μm. For each bidisperse packing, we mix together two separate batches of monodisperse droplets at a number ratio of small droplets to big droplets $= 2.3 \pm 0.4$. The mean 2D diameter of large droplets is 198 ± 6 μm and that of small droplets is 138 ± 4 μm, which gives the diameter ratio of the bidisperse mixtures $d_L/d_S = 1.44 \pm 0.07$. To nondimensionalize lengths in this chapter, we use the 2D mean diameter $\langle d \rangle$ (138 μm for the monodisperse sample, and 156 μm for the bidisperse sample).

In our experiment, we confine droplets between two 25 mm × 75 mm glass slides that are separated by pieces of 100 μm thick transparency film sealed with epoxy (method details are in Sec. 2.3). These pieces of film act as spacers creating a thin gap of thickness 114±1 μm. The same sample chamber is reused for different experiments. The gap thickness is measured within about 1 cm^2 area where the data is taken and within that region almost no thickness variation is found. The small variation in the gap spacing, less than 1%, ensures that the slides are parallel. The diameters of the oil droplets are chosen to be larger than the gap of the sample chamber. Thus, the droplets are squeezed between the two glass slides without overlapping to achieve a quasi-2D system.

The left panel in Fig. 6.3 shows the schema of the chamber. The droplets are confined in one direction and open in the other direction. The overall area of the open chamber that can be filled with emulsion is 7 mm × 25 mm, which is indicated as the area between two black dash line in Fig. 6.2. A micro-pipette is inserted into the emulsion from the side of the chamber with the tip diameter about 40 μm, which is much smaller than a typical droplet size. Smaller tip size, 20 μm for example, will lead to high pressure that is built up before the inflating droplet comes into the sample and also cause the inflating droplet to break off from the tip easily. In order to make roughly 40 μm tip size, the borosilicate glass with inner diameter 0.86mm works the best (Sutter Instrument B150-86-10) with the pipette puller that we commonly use (more details in Sec. 2.1). A closed chamber is also tried with the purpose to achieve greater symmetry in boundary condition but it fails due to some technical difficulty. In specific, while sealing the chamber with epoxy after loading droplets

into the chamber, it is easy to disturb the emulsion sample due to the compliance in the system. The droplets around the tip would come in and out the micro-pipette and their size will change due to the shear at the tip caused by the pressure change. Fig. 6.4 is an example of the failed closed chamber. The micro-pipette is at the bottom of the image and the area near the micro-pipette tip is full of small droplets with uncontrolled sizes. Similarly, this issue also exists with moving the sample chamber. So, it is very important to avoid disturbance while placing the chamber on microscope. Another disadvantage of closed chamber is the lack of reusability compare to the open chamber, which we can reload new batches of emulsion after each experiment.

The density of the water and mineral oil are different ($\rho_{\text{water}} = 1.00$ g/cm^3, $\rho_{\text{oil}} = 0.83$ g/cm^3) but the chamber is horizontal and thus buoyant force does not play a role in this experiment. First we load the emulsion into the sample chamber and let it equilibrate. Note that the micro-pipette needs to be filled with exactly the right amount of oil before we load the sample so that no air bubbles would be trapped in the system. Then, a syringe pump injects pure mineral oil through the micro-pipette into the emulsion to form an inflating droplet. The choice of mineral oil to form the inflating droplet is made after trying injecting air bubble or silicon oil. Due to its large compressibility, the air bubble could be compressed in the tiny micro-pipette tip and then quickly expands its volume once being injected into the emulsion, which is too fast for achieving a quasi-static system. The silicon oil that I tried (Brookfield 10cps) has lower viscosity ($\eta_s \approx 10$ mPa$\cdot$s) than mineral oil ($\eta_m \approx 69$ mPa$\cdot$s), which might be the reason for mineral oil to be a better option.

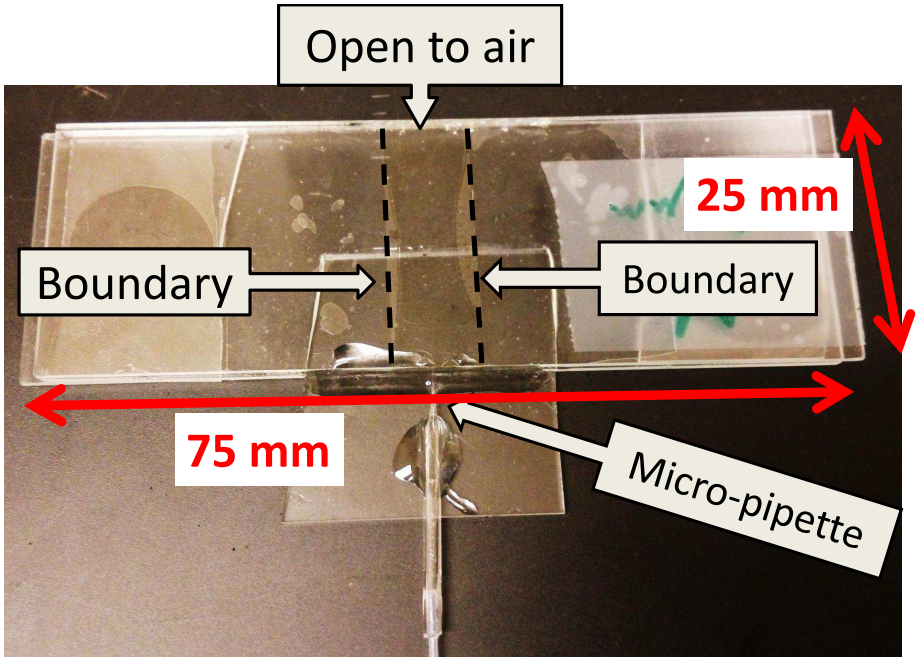

Figure 6.2: Photograph of experimental chamber and attached pippete. The chamber to fill emulsion sample is the area between the two black dash lines, which is open to the air. The glass slides dimensions are 75 mm $\times$ 25 mm. The chamber area is 7 mm $\times$ 25 mm. The micro-pipette for injecting the inflating droplet is inserted into the chamber from the bottom in the photo.

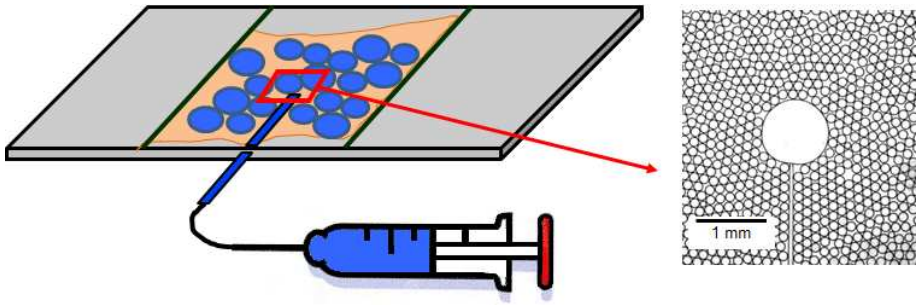

Figure 6.3: Schema of experimental setup. Blue circles in the chamber are oil droplets confined between two slides to achieve quasi-2D. The air-water interface is shown in the left panel too. The micro-pipette is inserted from the side of the chamber, which can be found at the bottom of the raw image in the right panel. The raw image is a monodisperse packing with area fraction $\phi = 0.85$.

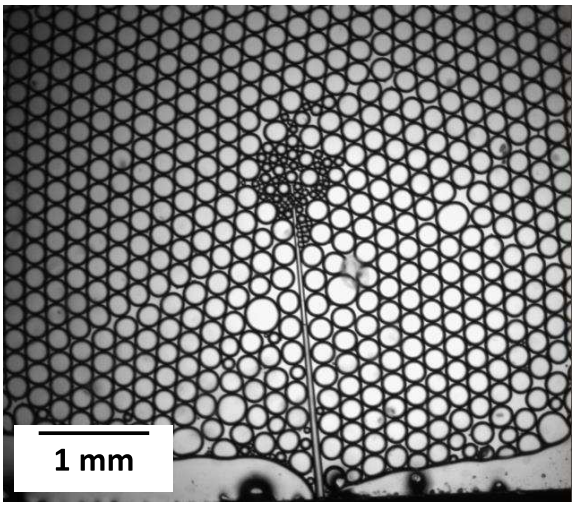

Figure 6.4: Failed example of closed chamber filled with monodisperse emulsion. The micro-pipette is inserted from the bottom side in the image. The messy small droplets with random sizes near micro-pipette tip are caused by the technical difficulty in sealing the chamber due to the compliance in the system.

We use Hamilton glass syringe 25 μL (model 1702 RN SYR) and inject the mineral oil at constant flux rate 5 μL/hr. We try to keep the pump rate as low as possible to create the quasi-static or rate-independent regime during the inflation process. Experimentally, the reason of not using even smaller pump rate is that the syringe pump has a finite pump step size of its step motor. A too small pump rate would cause the pumping to be not continuous, which could cause the inflating droplet to break off and detach from the micro-pipette tip. This is also why we use a small volume syringe (25 μL) so the inner diameter of the syringe is sufficiently small and the pumping could be smoother. A simple dimension analysis supports our choice of the flux rate as follows: A typical droplet size $V \sim \pi r^2 h \sim \pi \cdot 10^{-3}$ μL, where $r \approx 100$ μm is the droplet radius and $h \approx 100$ μm is the chamber gap thickness. If we aim for 5 seconds as the time for the inflating droplet to grow to a typical droplet

size, the flux rate $\approx \pi \cdot 10^{-3}$ μL/5s ≈ 2 μL/hr.

We use a microscope (Leica DM IRB) with a 1.6× objective lens and 0.35× lens in the camera connector to image the system, focusing on the region around the inflating droplet. A CCD camera (Mightex 5MP monochrome CMOS camera BCE-B050-U) records the images at frame rate between 2.8 and 3.8 images/second. This is sufficient to track the trajectory of each individual droplet using standard software[96]. More details about imaging can be found in Sec. 2.4 and details about the emulsion tracking in Sec. 3.2. The right panel in Fig. 6.3 shows a typical raw image of monodisperse packing, in which we record hundreds of droplets within the field of view. The positional uncertainty of each droplet is ± 4 μm, corresponding to about $\pm 0.03\langle d \rangle$.

6.2.2 Control Parameters

The two control parameters for our experiments are the area fraction ϕ and the polydispersity of the packing. ϕ is the fraction of the area occupied by oil droplets. I use two types of samples, monodisperse and bidisperse because they can make good comparison between ordered and disordered systems. Monodisperse packing is the example of ordered systems and bidisperse packing is the representative of disordered systems. Fig. 6.5 shows the raw images of monodisperse and bidisperse emulsions. We do rough control of ϕ by loading different sets of emulsion into the chamber before the syringe pump starts pushing. The droplets are condensed for high area fraction by using gravity before it is being loaded (see Fig. 2.6 in Sec. 2.2) and they can be diluted for lower area fraction by adding water with surfactant. Then we measure ϕ

based on the images (details in Sec. 3.1). Although the chamber is open to the air in one direction, the droplets are not able to pop out of water and expand to that direction to decrease ϕ when the inflating droplet is growing. This is because of the surface tension at the air-water interface that prevents this. Therefore, ϕ has no time dependence during the inflation process, which is the same as a similar system with different geometry where droplets flow with water without changing ϕ (the study described in Chap. 5). We take a total of 13 data sets with $0.77 \leq \phi \leq 0.99$, in which 4 data sets are monodisperse and 9 data sets are bidisperse. There is a possible systematic uncertainty for ϕ as the apparent size of each droplet depends on the illumination settings of the microscope (more details in Sec. 3.1); we estimate this systematic uncertainty is 4% at most [149]. There is an additional 1% random uncertainty due to random errors in our image analysis. We keep the microscope illumination settings constant between each experiment to minimize these random errors.

To quantify the difference in ordered structure within our samples, we use the structural order parameter ψ_6, which is defined as

$$\psi_6 = \frac{1}{n}|\sum_{i=1}^{n} e^{i6\theta_i}|, \tag{6.1}$$

where n is the number of neighbors for certain droplet and θ_i is the angle pointing from the center of the droplet to the neighboring droplet i, as shown by the segments in the top panel in Fig. 6.6. The segments are the lines connecting a certain droplet and its neighbors. θ_1 in red and θ_2 in blue are shown as examples of the angles. The bottom panel of Fig. 6.6 shows examples of local structures with different ordering including perfect hexagonal structure, which gives $\psi_6 = 1$, and other structures with

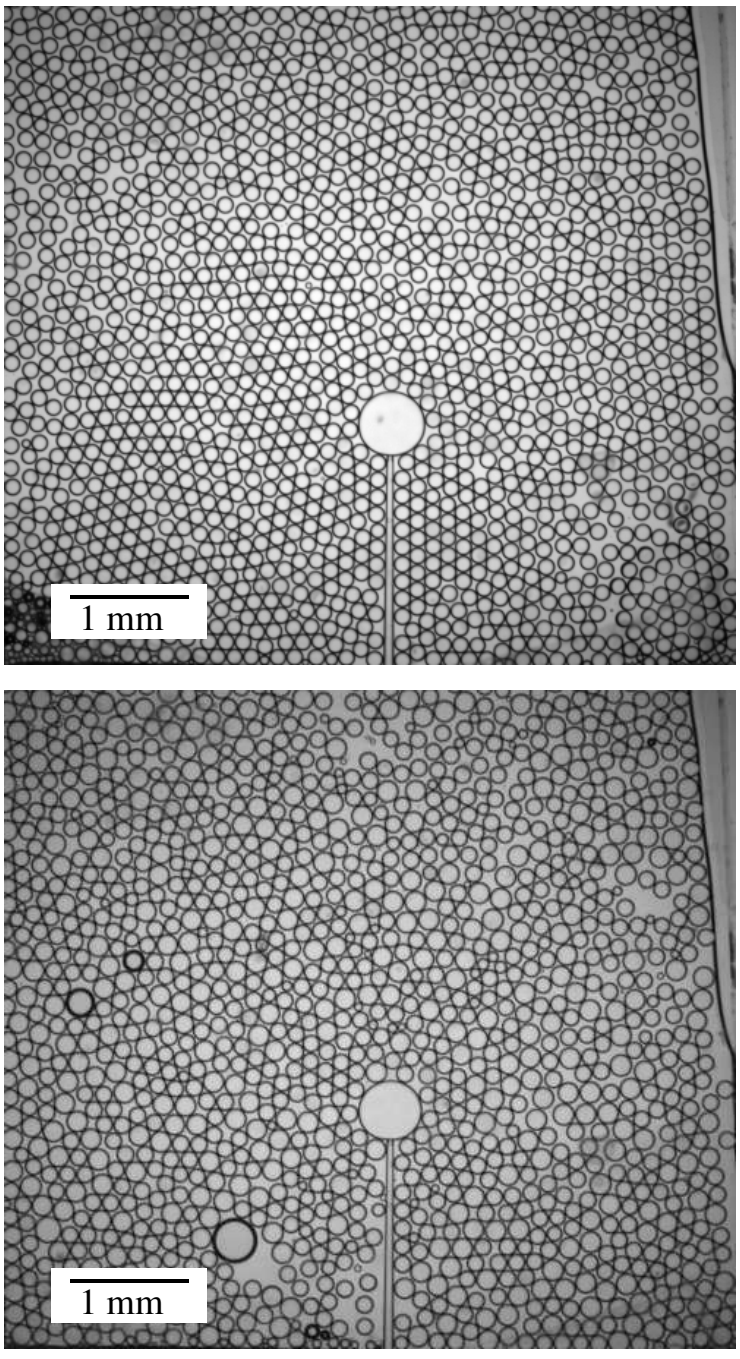

Figure 6.5: Top: Monodisperse packing with area fraction $\phi = 0.85$; Bottom: Bidisperse packing with area fraction $\phi = 0.84$. Note that these images are the moments during the growth of the inflating droplet.

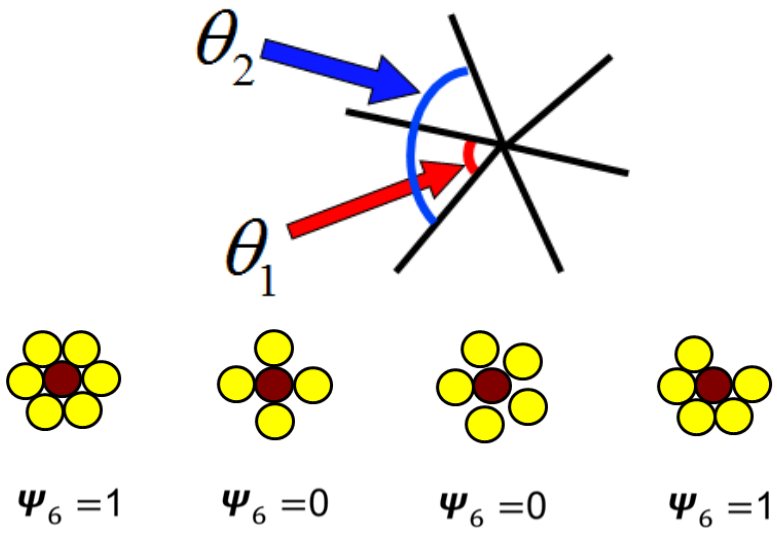

Figure 6.6: Top panel: Schema of definition for ψ_6. Bottom panel: Examples of local structures (from left to right): perfect hexagonal structure has $\psi_6 = 1$, symmetric structure with four neighbors has $\psi_6 = 0$, symmetric structure with five neighbors has $\psi_6 = 0$, perfect hexagonal structure with one neighbor missing has $\psi_6 = 1$.

$\psi_6 = 0$. Note that ψ_6 is an order parameter indicating how close the local pattern to a hexagonal structure. We compute ψ_6 for each droplet and average this over all droplets in a sample and over all time. Fig. 6.16 shows that the mean ψ_6 is correlated to mean ϕ obviously for monodisperse packings (circles) but much less clear for bidisperse packings (triangles). For the monodisperse samples, samples with larger ϕ have larger continuous crystalline domains; some medium-sized crystalline regions are seen in Fig. 6.5(top) for example. More details will be included in Sec. 6.3.3.

6.3 Results and Discussion

6.3.1 Mean Flow

For each droplet, we can define its distance to the instantaneous center of the inflating droplet as r. We also measure the instantaneous velocity $\vec{v}$ of every droplet. Both $r(t)$ and $\vec{v}(r,t)$ are time-dependent for each droplet. Fig. 6.7 shows the definition schema of $r(t)$ and $\vec{v}(r,t)$. A typical case for a certain droplet would be like this: $r(t)$ gets bigger while the droplet is moving further away from the center of the inflating droplet and the velocity of this droplet $\vec{v}(r,t)$ gets smaller due to the constant pump rate mentioned above. The instantaneous velocity $\vec{v}$ can be decomposed to radial component v_r and angular component v_θ, with the expectation that on average $v_\theta = 0$ by symmetry.

Due to the incompressibility of mineral oil and water, the mean flow of the droplets should be

$$\bar{v}_r(r,t) = \frac{A}{2\pi h r} = \frac{C}{r}, \bar{v}_\theta(r,t) = 0 \tag{6.2}$$

based on the simple fluid model and the conservation of fluid, where A is set by the pump rate and h is the gap thickness of the chamber. This is aligned with what we observed in the experiments (data not shown). The imposed flux rate in all the data sets are set to be $A = 5$ μL/hr and the chamber thickness is $h = 114$ μm. We can calculate the value of the constant $C = 0.102 \langle d \rangle^2/s$ for monodisperse and $C = 0.0814 \langle d \rangle^2/s$ for bidisperse samples, where $\langle d \rangle$ is the mean 2D diameter of droplets (not including the inflating droplet). So, accordingly the mean flow will be in the units of $\langle d \rangle/s$ and the distance r is in the units of $\langle d \rangle$. This pre-computed value of C

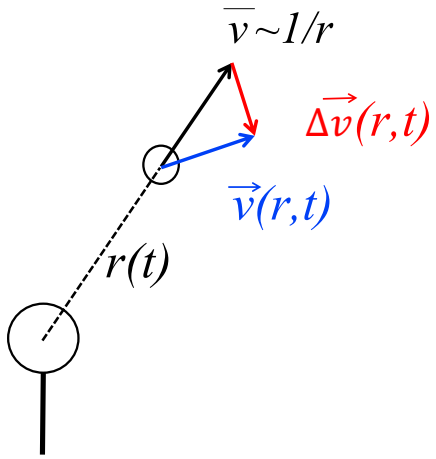

Figure 6.7: Schema for definition of distance $r(t)$, velocity $\vec{v}(r,t)$, mean background velocity $\bar{v}(r)$ and deviation $\Delta\vec{v}(r,t)$. The big circle indicates the inflating droplet and the small circle is a certain droplet in the emulsion sample. r is the distance of the droplet to the center of the inflating droplet. The blue vector is the instantaneous velocity of the droplet $\vec{v}$. The black vector is the mean background velocity $\bar{v}(r)$, which is proportional to $1/r$. The red vector $\Delta\vec{v}$ is the deviation in velocity, which is obtained by subtracting the velocity (blue arrow) by the mean background velocity (black arrow).

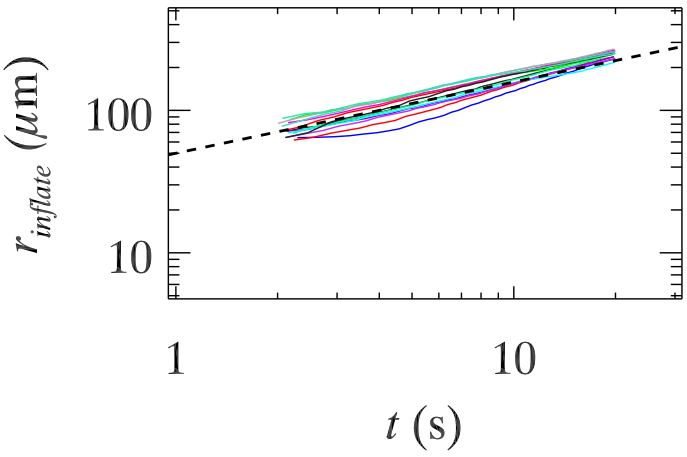

Figure 6.8: The radius of inflating droplet as a function of time $r_{\text{inflate}} \sim \sqrt{t}$. The black dash line has slope of 1/2. Different color indicates different experiment. This plot indicates that the growth of inflating droplet verifies that the flux rate is constant.

are consistent with their observed value within some error. For example, we observed $C = 0.111\ \langle d \rangle^2/s$ for the monodisperse and $C = 0.0926\ \langle d \rangle^2/s$ for the bidisperse packing of the example data sets that are shown in Fig. 6.5. C varies slightly from experiment to experiment and also it differs a little from the pre-computed value. Likely it is due to some compliance in the sample chamber and the plumbing system. Although the variation in C exists between experiments, the flux rate A is pretty stable by measuring the growth of the inflating droplet for each experiment. As shown in Fig. 6.8, the radius of the inflating droplets is proportional to the square root of time $r_{\text{inflate}} \sim \sqrt{t}$. In log-log scale, the dash line has the slope of 1/2.

There is one asymmetry in the experiment, namely, that the inflating droplet does not inflate evenly from its center but rather the oil is injected into one side of the droplet (Fig. 6.3). Because of this, droplets behind this inflating droplet (next to the micro-pipette) move very little, and droplets directly in front move the fastest. In

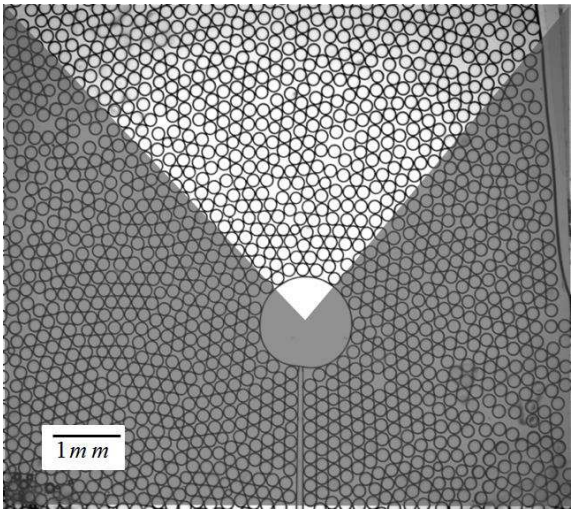

Figure 6.9: Schema for cropping the data. Our data analysis is done using data from the highlighted quadrant in front of the inflating droplet, except where specified. This quadrant is defined at each time based on the instantaneous center of the inflating droplet.

this case, the center of the system ($r = 0$) slowly changes over time. We could move into the moving reference frame centered on the center of the inflating droplet, where $r = 0$, but the problem is that the laboratory reference frame has a real meaning: droplets feel a viscous force from the glass plates when they move, and do not when they are motionless. So this would be a qualitative difference between the front and back of the injection micro-pipette. Accordingly, the majority of our data analysis will be done with the droplets in the quadrant in front of the inflating droplet, as the brighter region indicated in Fig. 6.9. As these droplets have the largest velocities, our signal to noise ratio is best in this region.

Since the mean flow shows no time dependence, we can show the time-averaged mean flow for each data set. Fig. 6.10 (a) and (b) show the mean flow rate averaged over all droplets, while (c) and (d) are only for the cropped region in front of the

micro-pipette as mentioned above. As can be seen by comparing the left panels to the right panels, the flow in the front region (right panels) is faster than the flow averaged over all angles (left panels). While the different colors in Fig. 6.10 indicate different area fractions ϕ, as expected the magnitude of the mean velocity $\bar{v}_r(r) = C/r$ does not depend systematically on ϕ. In fact, it should be ϕ-independent, but slightly differences are seen, especially at large r. Reasons are discussed as following.

Basically, the slight difference between experiments are mainly due to the systematic difference in flux rate. The bigger fluctuation in mean flow $\bar{v}_r(r)$ at large r, where the velocities are slow and hard to measure, is due to the limitation of resolution and insufficient droplets to have statistical results. To check the noise level of velocity, a plot of mean flow rate $\bar{v}_r(r)$ as a function of r is shown in Fig. 6.11. As r gets really large, $r = 40\langle d\rangle$ for example, droplets are not moving and the velocity is the noise level, which is shown by the red dash line in Fig. 6.11. The noise level in velocity in this typical example is $0.004\langle d\rangle/s$. The mean velocity resolution is $0.009\langle d\rangle/s$ with minimum $0.004\langle d\rangle/s$ and maximum $0.015\langle d\rangle/s$. Correspondingly, the velocity starts to hit the resolution limit around $r \approx 10 - 20\langle d\rangle$, which can be told in both Fig. 6.10 and Fig. 6.11. Another reason to not consider droplets that are too far away from the inflating droplet is the side wall effect. The boundary can limit the motion of the droplets. For example, the droplets on the top right corner in Fig. 6.9 are difficult to move in $\hat{r}$ direction. Also, referring back to Fig. 6.10, I do not include data at large r. And, there is almost no data at $r \sim \langle d\rangle$ since the inflating droplet quickly expands past that point. So, the only data at $1.5\langle d\rangle < r < 20\langle d\rangle$ is shown in Fig. 6.10.

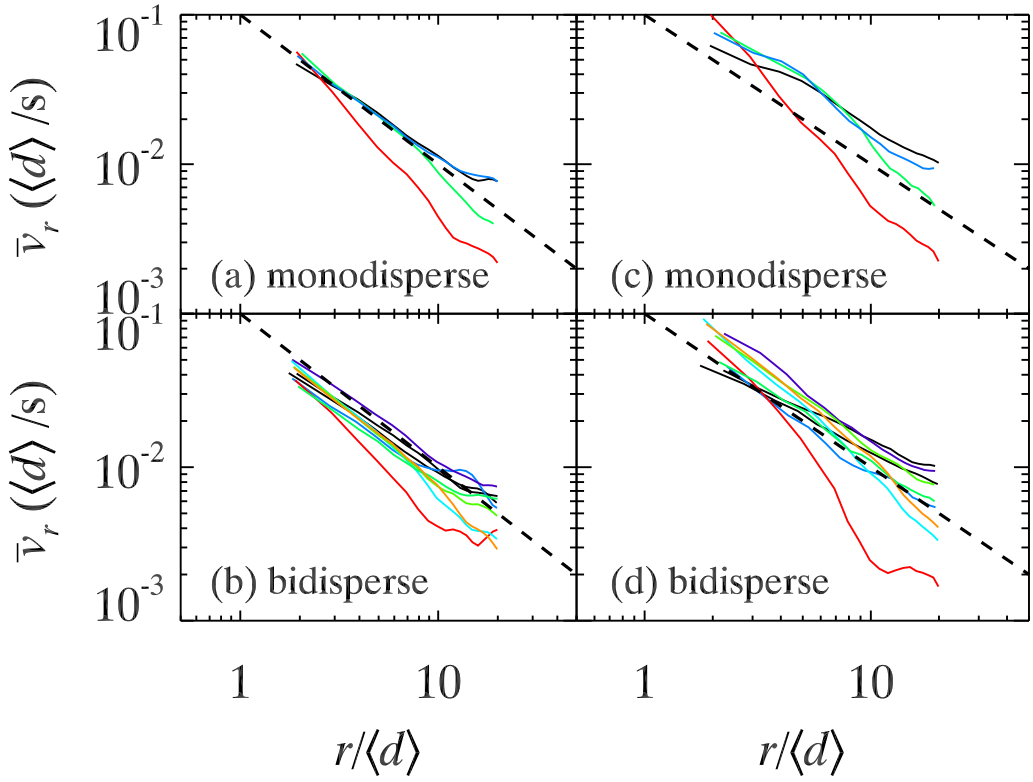

Figure 6.10: Mean radial velocity $\bar{v}_r$ as a function of its distance r to the center of inflating droplet for different packings. Color is random but indicates different experiment with different area fractions. Top two plots (a) and (c): monodisperse packings; Bottom two plots (b) and (d): bidisperse packings. Left two plots (a) and (b): data averaged over the whole region; Right two plots (c) and (d): data averaged over the cropped region alone (in front of the micro-pipette); see Fig. 6.9. The black dash lines are the magnitude of the mean velocity calculated based on Eqn. 6.2 with slope $= -1$. There is not enough data for a suitable measurement at $r < 1.5\langle d \rangle$ as the inflating droplet grows quickly past this radius. For $r > 10\langle d \rangle$, the droplet motions are approaching our measurement limits and so the data are noisier.

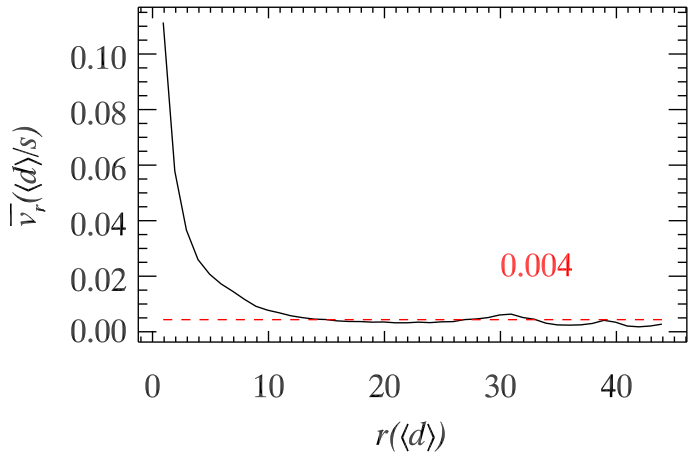

Figure 6.11: Mean background flow rate $\bar{v}_r$ as a function of the distance r to the center of inflating droplet, which should follow $\bar{v}_r(r) = C/r$. The red dash line indicates the resolution of velocity. The value is $0.004\langle d \rangle/s$ for this specific data example with $\phi = 0.79$.

6.3.2 Velocity Fluctuation

While the mean flow is well-defined by Eqn. 6.2, observations of the raw movies indicate that at any given moment the droplet motion is spatially heterogeneous. Accordingly, we define the fluctuating component of the velocity as the deviation from the mean flow

$$\Delta v_r(r,t) = v_r(r,t) - \bar{v}_r(r), \tag{6.3}$$

$$\Delta v_\theta(r,t) = v_\theta(r,t), \tag{6.4}$$

with overall magnitude $\Delta v(r,t)$, as shown in the schema Fig. 6.7. As we are in a rate-independent regime, we anticipate that the local fluctuations in velocity to be proportional to the local mean velocity, so accordingly we normalize the deviation by

the background velocity as the local fluctuation $\Delta v/\bar{v}$.

Fig. 6.12 shows the fluctuation $\Delta v/\bar{v}$ as a function of r. Here the fluctuation is averaged over all the droplets with same r. For both monodisperse and bidisperse packing, given that the curves are mostly independent of r, we see that indeed the local fluctuations are proportional to the local mean velocity. Note that the slight increase of fluctuation at large r is due to the limit of resolution mentioned above. Those droplets are far from the inflating droplet and thus move slowly compare to the pixel size. So, we cut the data when droplets have $r > 20\langle d\rangle$ and it applies to all the following plots in this Chapter. Different color is randomly chosen but they are indicating different experiment with different area fraction ϕ. Both plots show the qualitative ϕ dependence: the level of fluctuation does not collapse for different ϕ. It is notable that the ratio $\Delta v/\bar{v}$ is generally larger than 1, indicating that the fluctuations are typically more significant than the mean flow.

To better visualize the dependence of the velocity fluctuations on ϕ, we use a single averaged value to indicate each data set. In Fig. 6.13, the top panel shows the mean fluctuation (averaged over a range of $1.5/\langle d\rangle < r < 20\langle d\rangle$) for each data set $\langle \Delta v/\bar{v}\rangle$ as a function of ϕ. The brackets $\langle\ \rangle$ indicates the mean operation that is over different r. The red circles indicate monodisperse samples and the black triangles are for bidisperse samples. It is clear to see the increase in mean fluctuation when ϕ increases within a large range $0.77 - 0.99$ for both ordered and disordered systems. The mean fluctuations are more significant at the largest area fractions. The biggest mean fluctuation is about three times bigger than the smallest mean fluctuation. This is perhaps unexpected, as typically one associates spatial heterogeneity at lower

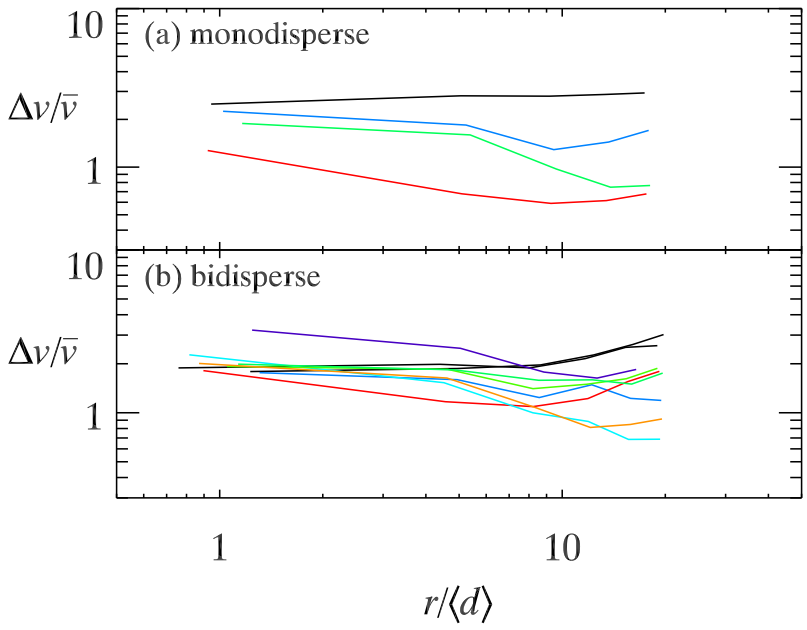

Figure 6.12: The fluctuating component of the velocity normalized by the mean velocity, plotted as a function of the distance r to the center of the inflating droplet for different packing fraction ϕ. Top: monodisperse packing; Bottom: bidisperse packing. Color indicates different ϕ but is randomly picked. Top curves have larger ϕ, as will be shown in the top panel in Fig. 6.13.

area fractions closer to jamming where droplets contact fewer neighbors [14, 24–31]. The other unexpected result is that the within the noise, the symbols agree between the monodisperse and bidisperse cases. A third result is that, as mentioned above, since the mean fluctuation is normalized by the mean velocity, the value of $\langle \Delta v/\bar{v} \rangle$ is between 0.9 and 2.8, which indicates that the mean fluctuations are as big as or several times bigger than the mean velocity.

To better understand the fluctuations, we consider the radial and angular components, Δv_r and Δv_θ. We average these over time and r (within the forward direction as in Fig. 6.9) and plot their ratio as a function of ϕ in Fig. 6.13(b). The bottom panel shows the ratio of mean radial component and mean angular component of the fluctuation. Note that the origin of the polar coordinates here is the center of the inflating droplet. Same as the top panel, red circles are monodisperse samples and black triangles are bidisperse samples. For both ordered and disordered systems, the ratio is bigger than one, which means that radial component is always larger than angular component.

Observing the movies, these large radial fluctuations are due to chains of droplets that are pushed away from the inflating droplet, so that even far away from the surface of the inflating droplet, droplets in that chain have large velocities. Examples are shown in Fig. 6.14. We emphasize that averaged over many droplets, the mean flow is quite simple (Eqn. 6.2, Fig. 6.10). Nonetheless, the instantaneous flow is more like that shown in Fig. 6.14, where only a subset of droplets are being displaced. Similarly, the fingering pattern is also shown by velocity in Fig. 6.20 and fluctuation (normalized by mean background velocity) in Fig. 6.21.

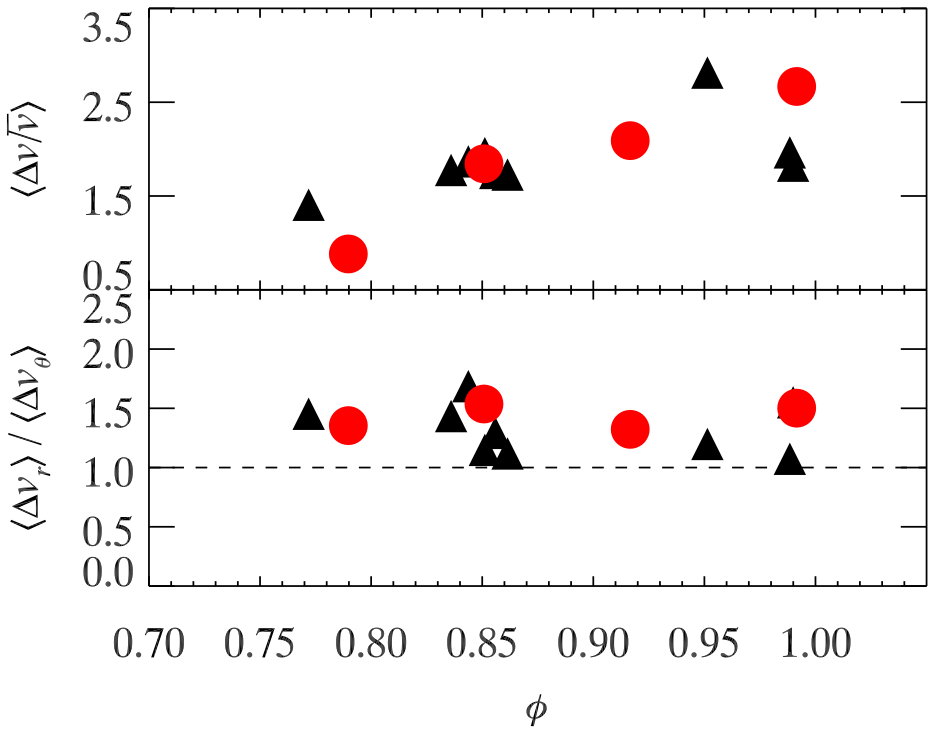

Figure 6.13: (a) The mean velocity fluctuation magnitude (normalized by the mean velocity) as a function of ϕ. (b) The ratio of the mean radial component and mean angular component of the velocity fluctuations as a function of ϕ. Red circles: monodisperse samples; black triangles: bidisperse samples. The black dash line is where the ratio $\langle \Delta v_r \rangle / \langle \Delta v_\theta \rangle = 1$.

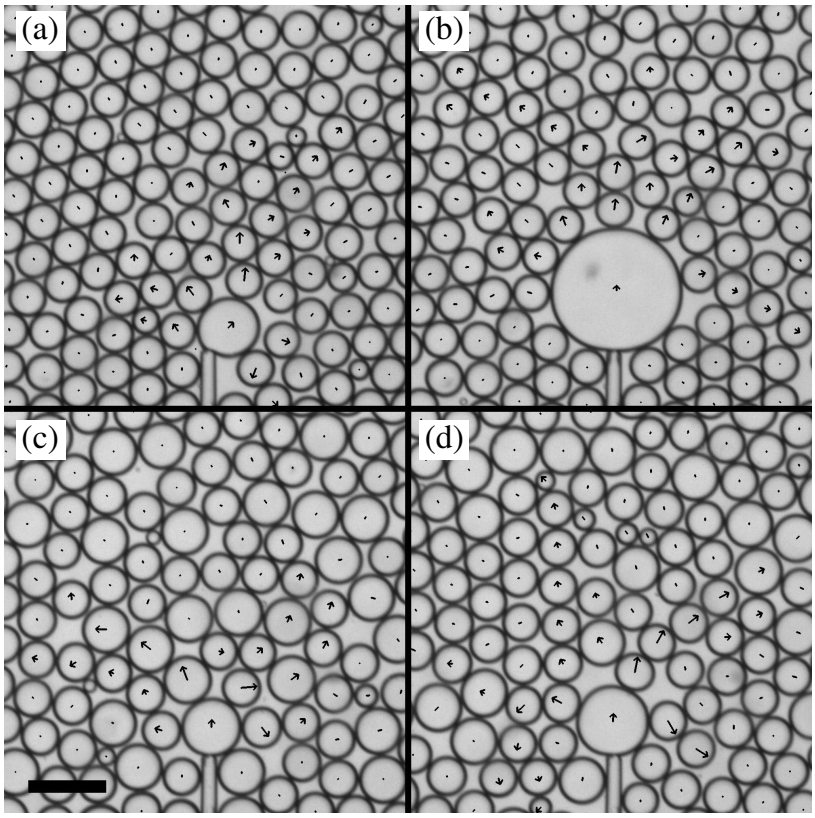

Figure 6.14: Images showing displacement vectors of droplets over 3 s. Vectors that are at least 20 μm are drawn as arrows. The scale bar is 100 μm. (a) Monodisperse sample, $\phi = 0.92$, 5 s after starting the inflation. (b) Monodisperse sample, $\phi = 0.85$, 27 s after starting the inflation. (c) Bidisperse sample, $\phi = 0.86$, 7 s after starting the inflation. (d) Bidisperse sample, $\phi = 0.84$, 7 s after starting the inflation.

6.3.3 Local Structure

The structural order parameter ψ_6, defined in Eqn. 6.1, are very different for the four monodisperse packings shown in Fig. 6.13. The fluctuations collapse nicely as a function of ϕ but there is no agreement in the plot of fluctuation as a function of ψ_6, as shown in the top panel in Fig. 6.15. This means that the packing fraction has large impact on the fluctuation. However, the structural ordering is not the leading factor for different dynamic response in our system. This is in contrast to the granular work [2] mentioned in Sec. 6.1. The relation between mean ψ_6 and ϕ is shown in Fig. 6.16. Monodisperse packings (red circles) show strong correlation between packing fraction and the spatial ordering. When more droplets with same size are condensed together in two dimension, the most efficient packing is to form hexagonal crystals and thus increase ψ_6 for the system. For bidisperse samples, the ordering is still slightly increased as ϕ increases but the signal is not as strong as monodisperse packings.

The mean ψ_6 mentioned above is for the whole sample in each experiment. It is interesting to see very different local structures for different packings, especially for the four monodisperse samples with different packing fractions. Monodisperse examples with high ϕ and low ϕ are shown in Fig. 6.17. Top two images (a) $\phi = 0.99$ and (b) $\phi = 0.79$ are raw images, on top of which color circles indicate the value of ψ_6 for each droplet. Red circles indicate high ordering with big ψ_6. In the condensed sample (a), there are more big crystal regions where droplets are strongly ordered. And, in the dilute sample (b), there are small crystal regions where droplets are weakly ordered. Correspondingly, the bottom two plots (c) and (d) in Fig. 6.17 are

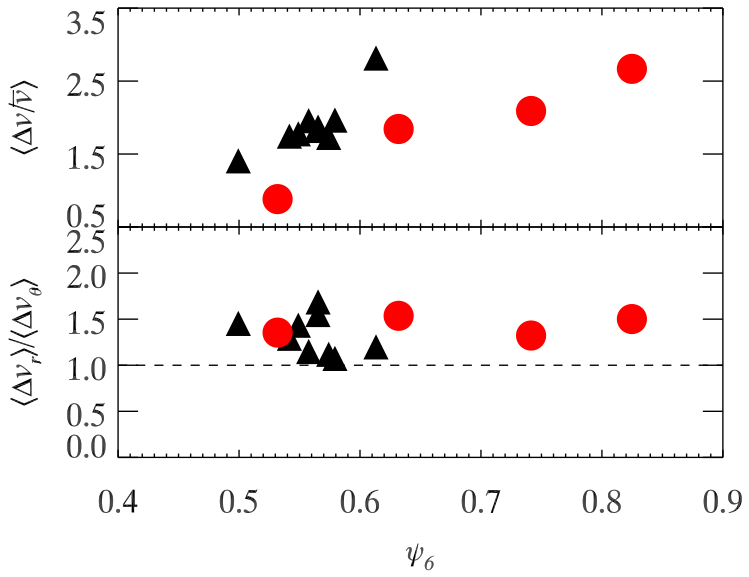

Figure 6.15: Top: mean velocity fluctuation as a function of ψ_6. Bottom: ratio of mean radial component and mean angular component of velocity fluctuation as a function of ψ_6. Red circles: monodisperse; Black triangles: bidisperse. The black dash line is where the ratio $\langle \Delta v_r \rangle / \langle \Delta v_\theta \rangle = 1$.

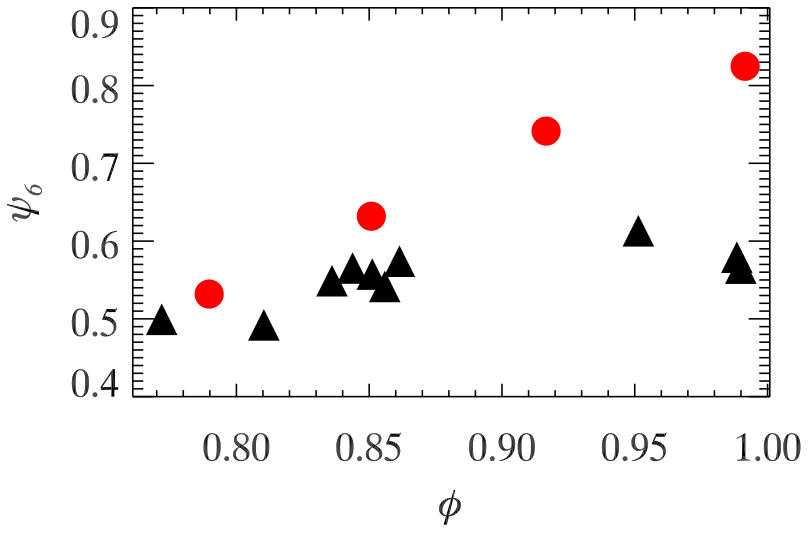

Figure 6.16: Mean ψ_6 as a function of ϕ for all data sets. Red circles: monodisperse; Black triangles: bidisperse.

the probability density function of local ψ_6. In (c), there is a substantial portion of the droplets having $\psi_6 \approx 1$, which means that they are in hexagonal crystals. In (d), the local ψ_6 distribution is fairly uniform.

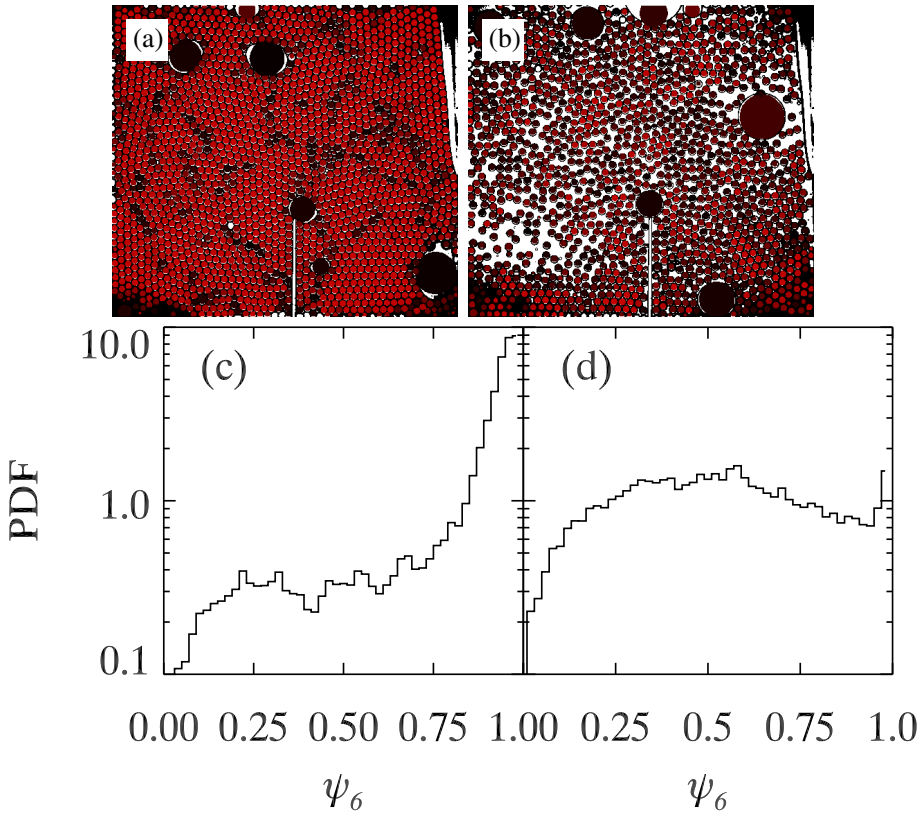

Figure 6.17: (a) and (b): local ψ_6 for two monodisperse examples with different packing fractions (a)$\phi = 0.99$ and (b) $\phi = 0.79$. Color indicates the value of ψ_6 for the droplets. More red-ish color, bigger ψ_6. (c) and (d) are the probability density function of local ψ_6 for (a) and (b) respectively.

Given the very different local structures shown in Fig. 6.17, it is straightforward to consider the spatial distribution of big local fluctuations in velocity and its relation with the local packing structure. Fig. 6.18 shows four examples including biggest ϕ and smallest ϕ for both monodisperse and bidisperse packings. The red arrows are the normalized velocity deviations for the droplets with top 1/3 biggest fluctuation

as a snapshot picked at a random time. We see the cooperative motion in (a) and strongly localized big fluctuation in (c). The distribution of red arrows in (b) and (d) are pretty random. (a) and (b) are bidisperse; (c) and (d) are monodisperse. We do not see much difference between different ordering in terms of the localization of big fluctuations. (a) and (c) are condensed packings with big ϕ; (b) and (d) are dilute samples with low ϕ. It is clear that the spatial distribution of red arrows are obviously more localized for condensed packings than dilute packings. Similar as what we mentioned above, ϕ is the leading factor to the big fluctuation distribution, but not ordering parameter ψ_6.

The next question would be more detailed about the fluctuation. One guess is that local rearrangements contribute to the big fluctuation. One way to quantify the local events is based on neighbor change between droplets. We can use Delaunay triangulation, which is a tessellation of the entire space into triangles, to build up bonds between neighbors of droplets. The edge of the triangles are the bonds (more details in Sec. 3.3). The bonds could break and rebuild over time when the droplets have non-affine local motion. We define bond breaking density as the number of bond breaking events divided by the number of droplets in that area. I use the entire length as the time window, within which the inflating droplet grows to 8 to 10 times bigger than average droplet size. Fig. 6.19 shows the bond breaking density as a function of its distance to the edge of the inflating droplet. This distance is calculated as $r - r_{\text{inflate}}$ in terms of $\langle d \rangle$, where r_{inflate} is the radius of the inflating droplet. The data points are average values over all data sets. The red line is an exponential fit $y = 3.68 \exp(-0.39x) + 0.98$, which gives decay constant $= 2.6\langle d \rangle$. Note that using

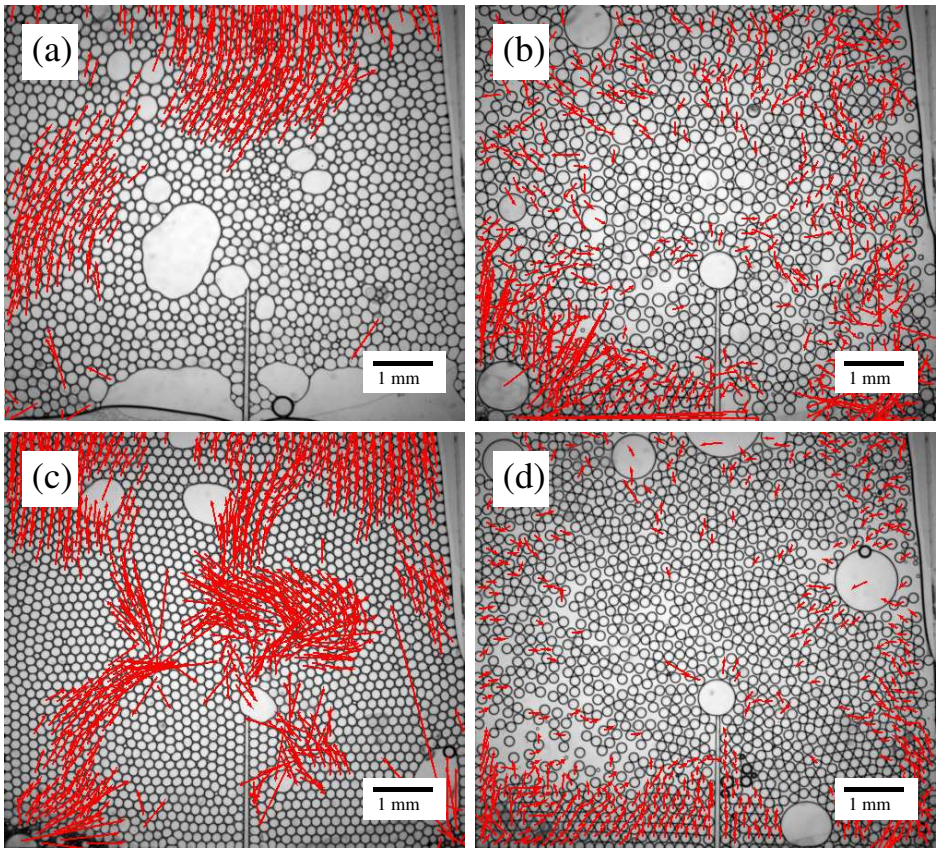

Figure 6.18: Top 1/3 biggest normalized deviation shown by red arrows at a random time. The direction of arrow is the direction of fluctuation and the length of the arrow is the magnitude of the normalized deviation. (a) Condensed bidisperse packing: $\phi = 0.99$, $\psi_6 = 0.57$; (b) Dilute bidisperse packing: $\phi = 0.77$, $\psi_6 = 0.50$; (c) Condensed monodisperse packing: $\phi = 0.99$, $\psi_6 = 0.82$; (d) Dilute monodisperse packing: $\phi = 0.79$, $\psi_6 = 0.53$.

number density of bond breaking events is different from using magnitude of the fluctuation. We already have that on average fluctuation is proportional to the mean flow rate, which is proportional to $1/r$, as shown in Fig. 6.12. However, Fig. 6.19 shows that there more bond breaking events close to the inflating droplets and the exponential decay has a length about 3 diameters of the emulsion droplets. There is no qualitative difference observed between monodisperse and bidisperse packings, or

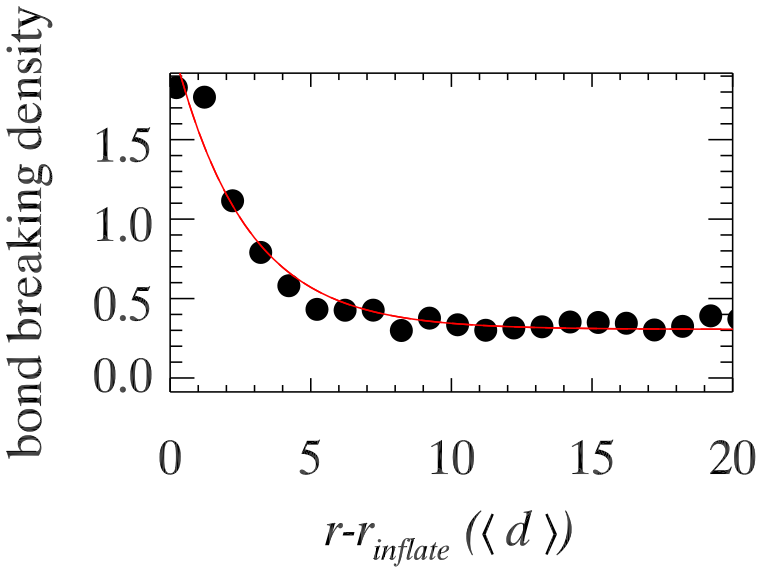

Figure 6.19: Bond breaking density (number of bond breaking events per unit droplet) as a function of its distance to the edge of the inflating droplet. Data are averaged over all data sets. The distance is in terms of $\langle d \rangle$, mean diameter of the emulsion droplets. The red line is an exponential fit $y = 3.68\exp(-0.39x) + 0.98$ with a decay constant $2.6\langle d \rangle$

dilute and condensed packings.

Recently, I repeat the experiments in the same settings but with slightly different magnification settings with the purpose to get more details of the dynamics near the micro-pipette tip. Fig. 6.20 shows the velocity of each droplet for monodisperse (a) and bidisperse (b) samples. Red indicates high velocity and blue indicates low velocity. In monodisperse packing, the droplets with big velocity seems have higher linearity. The droplets with biggest velocity are aligned in a straight line pointing from the inflating droplet to top left direction, shown as the red-ish and yellow-ish droplets in Fig. 6.20(a). However, there is less directionality shown in bidisperse packing in

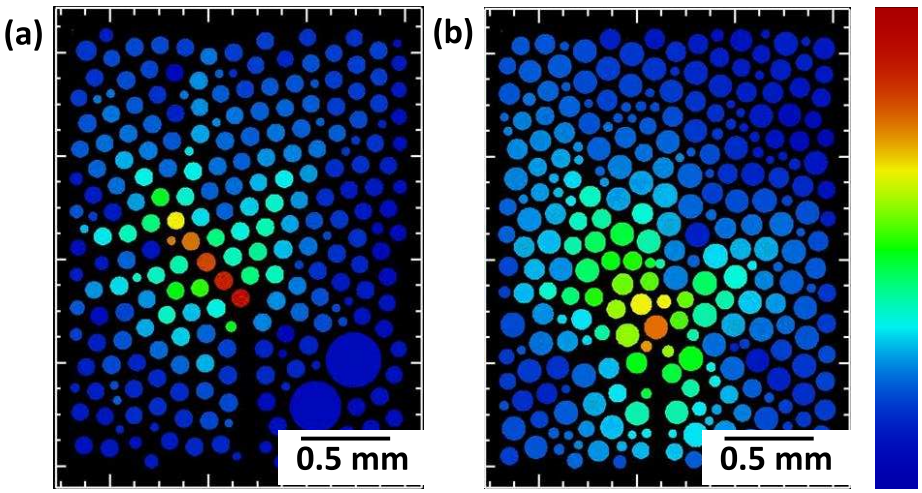

Figure 6.20: Velocity for each droplet at a random time for (a) monodisperse packing, $\phi = 0.83$ and (b) bidisperse, $\phi = 0.96$. Red indicates big velocity and blue indicates small velocity.

Fig. 6.20(b), where the fast droplets are in all directions as shown in orange or greenish circles. This is similar when we look at the normalized fluctuation of the same two examples, as shown in Fig. 6.21. It is another sign showing the interesting relation between local structure and the motion of droplets. One idea that might be related is about the fragility in soft materials [120]. A "fragile" media is defined as unable to support certain types of incremental loading without plastic rearrangements. Using local ψ_6, we can get the difference in ψ_6 between the droplet and its neighbors and see if this difference is related to the fragility, in which way we can predict the dynamics based on the local structural information.

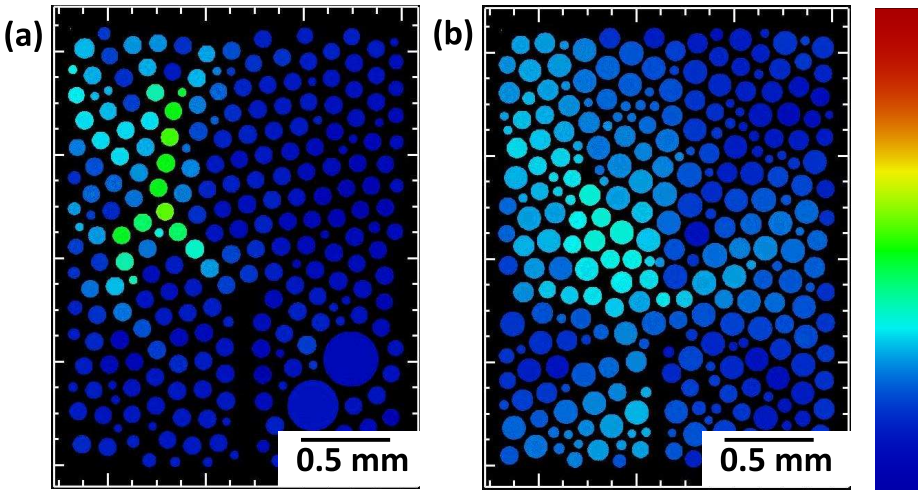

Figure 6.21: Normalized fluctuation for each droplet at a random time for (a) monodisperse packing, $\phi = 0.83$ and (b) bidisperse, $\phi = 0.96$. Red indicates big velocity and blue indicates small velocity.

6.4 Conclusion and Outlook

We have demonstrated in this Chapter that in a quasi-two-dimensional emulsion system, the average flow can be described by simple fluid model but the fluctuation in dynamic response to a local perturbation increases as packing fraction gets further above jamming. No dependence on polydispersity is observed. As the system is more jammed, droplets might need to have more local rearrangements in order to move, which leads to higher velocity fluctuation. Some preliminary exploration on local structure show interesting features including local ordering parameter ψ_6 and non-affine motion quantified by bond breaking events. For condensed packings, droplets might need to move cooperatively in bidisperse sample and rearrangements are likely happening at the defects in monodisperse packing. There is no statistical analysis on the local details, so further study is required to draw any conclusion.

Some ideas for further study:

(1) In space, we can study the heterogeneity of the dynamic response. For example, dynamic correlation in space.

(2) In time, we can study how the force evolves based on force analysis.

(3) If more experiments could be done focusing on the initial growth of the inflating droplet, we can compare our force result with that in granular materials [2]. Specifically, higher frame rate can be achieved using Greypoint camera (9 frames/second) and more details in forces can be captured. Before the emulsion sample start to have any bond breaking events or local rearrangements, we can study the force response of the system to the inflating droplet, which provides the point force and thus Green's function can be examined.

(4) Jamming point ϕ_J can be determined if we have more data sets close to jamming. Based on the main findings shown in Fig. 6.13, we can scale the fluctuation as a function of $\phi - \phi_J$, which is the distance of ϕ to the jamming point. By fitting, we can get the scaling $\langle \Delta v/\bar{v} \rangle \sim (\phi - \phi_J)^{\alpha}$. Universal non-trivial power-law scaling behavior exist in various soft materials including foam, emulsion, granular material, etc.: the kinetic and dynamic response scale with distance to jamming [13–20, 23, 26, 150–152]. A very similar experiment with granular materials by inflating an intruder inside the packing has shown different regimes of mechanical response to shear around the jamming transition [153].

(5) The flux rate can be controlled to produce different range of strain rate. A recent simulation work, which is based on Durian's 2D bubble model [69], has shown the dependence of the response on strain rate and area fraction [135]. They find that

the fluctuations in the local dissipation vary from nearly Gaussian and homogeneous at low densities and fast flows, to strongly intermittent for large densities and slow flows.

(6) We have force measurement technique developed in the lab on the scale of each contact between droplets with a few percentage accuracy. So, more analysis could be done on force network including the linearity of the force chain, the relation between the force and the motion of the droplets, non-locality feature [154], and rate dependence of force networks, as has been done in sheared granular materials [73]. Some IDL code are available to obtain the angles between force chains.

(7) There are other approaches to produce local perturbation. One example is to reverse the growth of the inflating droplet by sucking it back into the micro-pipette, which might have some technical difficulty. Another method we tried is using ferro-fluid. As Fig. 6.22 shown, the black droplets are filled with ferro-fluid. We can use magnets to control the ferro-fluid droplet like moving it around by dragging it through the emulsion, as the slow drag in granular media [155, 156], or vibrating the ferro-fluid droplet at different magnitude and frequency.

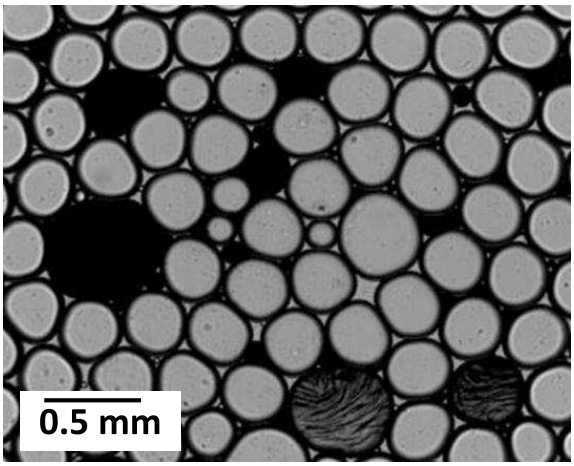

Figure 6.22: Ferro-fluid droplet controlled by magnets as local perturbation in emulsion. Black droplets are ferro-fluid droplets.

Chapter 7

Summary

7.1 Summary of Thesis

Soft materials have and will continue to have a variety of applications because of its "versatility" of being in the state between a liquid and a solid. This field has been attracting our attention for decades due to its rich phenomena and the unknown underlying physics. More specifically, approaching it by studying the dynamics of lab model systems, such as colloids, grains, foams and emulsions, is the most accessible perspective because the scale of them could be both small enough to study Brownian motion and big enough to ignore thermal energy or even to be visualized by eyes. This dissertation is using oil-in-water emulsion confined between glass slides to achieve quasi-2D as the experimental model. Choosing emulsion is not only because of the well-developed microfluid technique in the lab to produce droplets in a precisely controllable way but also because of its unique features by nature to explore less-studied ideas like frictionless particles and the influence of particle softness. To study

its flow property, a wide range of drivers are used including gravity, oil pumping and local poking by inflating oil droplet into the sample. The big goal is to better understand the physics of jamming transition, which in other words is to understand what is responsible for the transition of a soft material from a liquid like state to solid like state. And, this dissertation is probing this problem by studying the flow property of emulsion from a dynamics perspective.

In this field, there are several well recognized existing models to describe the flow property. For example, the archetypal Herschel-Bulkley constitutive relation is a generalized model for non-Newtonian fluid [157]. It relates the shear rate of the flow to the shear stress in a nonlinear way, which can capture many cases especially good in the case of pressure-driven channel flow. However, it cannot capture the cases in my dissertation, where the flow of emulsion demonstrates discrete avalanches involving many jamming and unjamming local events. Another example would be the jamming phase diagram proposed by A. Liu [6], where the three parameters controlling the jamming transition is density, temperature, and shear stress. However, the softness, for example, is not considered. Therefore, by studying the dynamics of emulsion is to provide a complementary view on the flow property of complex fluid and to better complete the jamming phase diagram.

In Chap. 4, I use gravity to drive the emulsion flow in a hopper geometry. Using different sizes of the hopper exits, a probability of clogging curve is fitted by a sigmoidal curve as a function of the hopper exit size. The clogging is only observed at a narrow hopper exit and no long arch formation in our emulsion system. This is different from what has been seen in granular hopper flow [1], where hard disks have

friction and the clogging can happen at a much larger hopper exit. Though their simple model shows that friction is not necessarily required to form long arch at the hopper exit, it is still unclear if the lack of friction or the softness in our system is responsible for the discrepancy between our observation and that in granular material. Later simulation work by Eric Weeks in our lab shows that the softness is playing the key role. In the simulation, gravity is tuned comparing to the forces between droplets, which is qualitatively the same as tuning the softness of the droplets. Long arch formation at large hopper exit is observed with low gravity, or hard droplets with high surface tension, which is a supporting evidence to explain the observation in my experiment. Within my emulsion system, forming long arch to clog the hopper exit is not seen and this is not because of the lack of friction but because of the large gravity to overcome the penalty in surface energy while the droplets deform themselves to flow through the hopper. Overall, our observation in the clogging during the flow of soft particles is qualitatively different from the cases of granular materials and softness plays a key role for the difference. This potentially has implications for other systems with soft interactions like flow of soft blood cells through tiny capillary, merging traffic and perhaps flowing bacteria. Further in the field of jamming transition it can provide a more complete view to the jamming transition phase diagram by adding another important dimension of softness.

In Chap. 5, I use oil pumping to drive the droplets flow through the hopper. Since changing the droplets concentration is the simplest approach to tune the response of a soft material and the oil pumping is controlled by syringe pump with great precision, the two parameters that I controlled in the experiment are area fraction and flow

rate. The gravity is removed in this case and the pumping is continuous and thus no "permanent" clogging would happen. There are various qualitatively different flowing behaviors observed. At the lowest flow rates, the droplets exit the hopper via intermittent avalanches and at the highest flow rates, the droplets exit continuously. The transition between these two is fairly smooth function of mean strain rate of the sample but there is no dependence of the flow behavior on the area fraction. The avalanches are characterized by a power law distribution of the time interval between droplets exiting the hopper, with long intervals between the avalanches. The power law exponent is decreasing with decreasing flow rate, which means my experiment is not in a quasi-static limit. Even the strain rate is approaching zero, the flow is not simple but rather dominated by the rare intermittent avalanches. The inverse of the critical strain rate for the transition from avalanche to continuous flow is about 4-10 seconds, which is in line with the time scale for the local structural relaxation time, a few second [87]. This suggests a potential physics to explain the two explicitly different types of flow behavior. At fast flow rates, local plastic events are more correlated and the droplets might exit the hopper before the plastic event is fully completed. The slow flow rates allow the events to complete and they are less correlated, which allows the pressure to build up and release in a large avalanche event with many rearrangements happening simultaneously. There are some evidence in our system with prior work [87] and also in 2D foam system [136]. Avalanche has been studied in some contexts and smooth flow in others. The suggestions from my experiments about correlated rearrangement mentioned above helps connect these two previously extreme cases. In Chap. 6, I use an open chamber with confinement in one direc-

tion and inject an inflating oil droplet into the center of the emulsion and study the dynamics of the system. The geometry is different from the constricting hopper chamber in the previous projects. The injecting volume is increasing at a constant speed. The two control parameters for different samples are polydispersity and area fraction. Macroscopically, the average flow can be described by simple fluid model but microscopically the movements of droplets are disordered due to the discreteness of the particles. The fluctuation in dynamic responses to the local perturbation increases as the area fraction gets further above the critical jamming point. Surprisingly, no dependence on polydispersity is observed. One of the potential reasons could be that at high area fraction droplets need to have more local rearrangements in order to move. And, they would be responsible for the higher velocity fluctuation. More data collecting and more analysis needs to be done to verify this explanation. Essentially it is a rare situation where disordered and moderately ordered samples have quite similar responses. And, this experiment helps show the connection between the smooth average response, which is continuum-like flow, and the reality of discrete rearrangements underlying the average response.

7.2 Impact and Outlook

By experimentally study the flow behavior of quasi-2D emulsion stated in this dissertation, we are able to provide a more complete view on the dynamics of soft materials. Given that a wide range of experiments in different systems are existing, it is exciting to see both the common characteristics and the remarkable differences in the emulsion system with its key features including the lack of friction and deforma-

bility. In Chap. 4, we found the discrepancy in the clogging probability, or the critical size of the hopper exit, in emulsion system versus prior work in granular hopper flow. This leads to the further findings in the simulation work of Weeks that introduces the critical role of stiffness in clogging with long arch formation at the hopper exit. This is a stretch on the range of gravity because in all the experiments with hard disks, gravity is too small to have significant influence on clogging. Therefore, the role of softness will be considered in the future study for systems with soft particles. Additionally, Chap. 5 shows the hopper flow driven by pressure. The key finding is the interesting avalanche-like flow behavior in the system composed of deformable particles. This suggests that the flow of jammed materials is not universal. The fact that it is controlled by strain rate but not packing fraction also sheds some light on understanding the relation between internal structural relaxation and the macroscopic flow behavior. Overall, the study that I have conducted opens the way to a more general understanding of the dynamics of soft materials. This could also provide some insights on the physics behind jamming transition and further surface potential application value in the system of soft particles.

Although we have been observed many interesting dynamic responses in all different kinds of emulsion systems, including prior experimental and theoretical work [44, 58, 158–161] from literature, from the work previously done in our lab [14, 80, 87] and that in this dissertation, there are still tons of physics questions that is unclear and new directions to explore. This provides numerous possibilities for future experiments. They can include but certainly not limit to:

(1) One of the most accessible directions to go is using existing force measurement

technique to measure the contact forces between droplets and relate it to the dynamics.

(2) Adjust softness of droplets to explore wider range of dynamics of the flow. For the experiment, the softness could be changed by changing the surfactant concentration, the type of surfactant or changing the droplet size.

(3) Change the solution to be viscous fluid and study the difference in the dynamics in order to further understand the role of local structural relaxation and its relation to avalanches.

(4) Similar to the idea in Chap. 6 with the common goal of creating local perturbation but in a even smaller magnitude, one can measure the dynamics response in a less collective behavior. I tried a new method to provide the local perturbation through driving magnetic droplet around inside the emulsion. Without constantly inflating a droplet and pushing other oil droplets away, the plastic deformation seems much more localized. However, more controlled experiments need to be done and it would be very interesting to see if there is any dependence on the dragging rate or packing fraction.

To summarize the overall impact of my dissertation, it is a demonstration that the physics of jamming and clogging is much different with soft particles. While they still exhibit features of hard particles in terms of jamming and clogging, the details of some of these features are changed in nontrivial ways. One might hope that other sorts of soft materials like sticky soft particles, anisotropic soft particles, highly polydisperse particles, etc. may also lead to new and interesting physics, so that this

dissertation will be one of several new and interesting directions taking us away from hard particle systems.

Bibliography

[1] K. To, P.-Y. Lai, and H. K. Pak, Jamming of granular flow in a Two-Dimensional hopper, *Phys. Rev. Lett.*, **86**, 71–74 (2001).

[2] J. Geng, D. Howell, E. Longhi, R. P. Behringer, G. Reydellet, L. Vanel, E. Clément, and S. Luding, Footprints in sand: The response of a granular material to local perturbations, *Phys. Rev. Lett.*, **87**, 035506 (2001).

[3] S. Maruyama and M. Tokuyama, *Statistical physics of complex fluids* (Tohoku University Press) (2007), ISBN 9784861630682.

[4] R. A. L. Jones, *Soft Condensed Matter* (Oxford University Press Canada) (2002).

[5] P. W. Anderson, Through the glass lightly, *Science*, **267**, 1611 (1995).

[6] A. J. Liu and S. R. Nagel, Jamming is not just cool any more, *Nature*, **396**, 21–22 (1998).

[7] V. Trappe, V. Prasad, L. Cipelletti, P. N. Segre, and D. A. Weitz, Jamming phase diagram for attractive particles, *Nature*, **411**, 772–775 (2001).

[8] A. J. Liu and S. R. Nagel, The jamming transition and the marginally jammed solid, *Ann. Rev. Cond. Mat. Phys.*, **1**, 347–369 (2010).

[9] M. Dennin, Discontinuous jamming transitions in soft materials: coexistence of flowing and jammed states, *J. Phys.: Cond. Matt.r*, **20**, 283103+ (2008).

[10] S. Henkes, C. S. O'Hern, and B. Chakraborty, Entropy and temperature of a static granular assembly: An abinitio approach, *Phys. Rev. Lett.*, **99**, 038002+ (2007).

[11] D. Bi and B. Chakraborty, Rheology of granular materials: dynamics in a stress landscape, *Philosophical Transactions of the Royal Society of London A: Mathematical, Physical and Engineering Sciences*, **367**, 5073–5090 (2009).

[12] P. Chaudhuri, L. Berthier, and S. Sastry, Jamming transitions in amorphous packings of frictionless spheres occur over a continuous range of volume fractions, *Phys. Rev. Lett.*, **104**, 165701+ (2010).

[13] D. J. Durian, Foam mechanics at the bubble scale, *Phys. Rev. Lett.*, **75**, 4780–4783 (1995).

[14] K. W. Desmond, P. J. Young, D. Chen, and E. R. Weeks, Experimental study of forces between quasi-two-dimensional emulsion droplets near jamming, *Soft Matter*, **9**, 3424–3436 (2013).

[15] K. A. Dahmen, Y. Ben-Zion, and J. T. Uhl, A simple analytic theory for the statistics of avalanches in sheared granular materials, *Nat Phys*, **7**, 554–557 (2011).

[16] C. S. O'Hern, L. E. Silbert, A. J. Liu, and S. R. Nagel, Jamming at zero temperature and zero applied stress: The epitome of disorder, *Phys. Rev. E*, **68**, 011306 (2003).

[17] H. A. Makse, N. Gland, D. L. Johnson, and L. M. Schwartz, Why effective medium theory fails in granular materials, *Phys. Rev. Lett.*, **83**, 5070–5073 (1999).

[18] W. Ellenbroek, E. Somfai, M. van Hecke, and W. van Saarloos, Critical scaling in linear response of frictionless granular packings near jamming, *Phys. Rev. Lett.*, **97**, 258001+ (2006).

[19] W. G. Ellenbroek, M. van Hecke, and W. van Saarloos, Jammed frictionless disks: Connecting local and global response, *Phys. Rev. E*, **80**, 061307+ (2009).

[20] P. Olsson and S. Teitel, Critical scaling of shear viscosity at the jamming transition, *Phys. Rev. Lett.*, **99**, 178001+ (2007).

[21] G. Katgert and M. van Hecke, Jamming and geometry of two-dimensional foams, *Europhys. Lett.*, **92**, 34002+ (2010).

[22] T. S. Majmudar, M. Sperl, S. Luding, and R. P. Behringer, Jamming transition in granular systems, *Phys. Rev. Lett.*, **98**, 058001+ (2007).

[23] M. van Hecke, Jamming of soft particles: geometry, mechanics, scaling and isostaticity, *J. Phys.: Cond. Matt.r*, **22**, 033101 (2010).

[24] K. W. Desmond and E. R. Weeks, Experimental measurements of stress redistribution in flowing emulsions (2013).

[25] R. Yamamoto and A. Onuki, Dynamics of highly supercooled liquids: Heterogeneity, rheology, and diffusion, *Phys. Rev. E*, **58**, 3515–3529 (1998).

[26] G. Katgert, B. P. Tighe, and M. van Hecke, The jamming perspective on wet foams (2011).

[27] M. D. Ediger, Spatially heterogeneous dynamics in supercooled liquids, *Ann. Rev. Phys. Chem.*, **51**, 99–128 (2000).

[28] R. Candelier, O. Dauchot, and G. Biroli, The building blocks of dynamical heterogeneities in dense granular media, *Phys. Rev. Lett.*, **102**, 088001+ (2009).

[29] O. Dauchot, G. Marty, and G. Biroli, Dynamical heterogeneity close to the jamming transition in a sheared granular material, *Phys. Rev. Lett.*, **95**, 265701+ (2005).

[30] A. S. Keys, A. R. Abate, S. C. Glotzer, and D. J. Durian, Measurement of growing dynamical length scales and prediction of the jamming transition in a granular material, *Nature Phys.*, **3**, 260–264 (2007).

[31] H. C. Andersen, Molecular dynamics studies of heterogeneous dynamics and dynamic crossover in supercooled atomic liquids, *Proc. Nat. Acad. Sci. of the United States of America*, **102**, 6686–6691 (2005).

[32] D. Howell, R. P. Behringer, and C. Veje, Stress fluctuations in a 2D granular couette experiment: A continuous transition, *Phys. Rev. Lett.*, **82**, 5241–5244 (1999).

[33] D. M. Mueth, Measurements of particle dynamics in slow, dense granular couette flow, *Phys. Rev. E*, **67**, 011304+ (2003).

[34] B. Miller, C. O'Hern, and R. Behringer, Stress fluctuations for continuously sheared granular materials, *Phys. Rev. Lett.*, **77**, 3110–3113 (1996).

[35] M. Dennin and C. M. Knobler, Experimental studies of bubble dynamics in a slowly driven monolayer foam, *Phys. Rev. Lett.*, **78**, 2485–2488 (1997).

[36] M. Dennin, Statistics of bubble rearrangements in a slowly sheared two-dimensional foam, *Phys. Rev. E*, **70**, 041406+ (2004).

[37] J. Lauridsen, G. Chanan, and M. Dennin, Velocity profiles in slowly sheared bubble rafts, *Phys. Rev. Lett.*, **93**, 018303+ (2004).

[38] C. Heussinger and J.-L. Barrat, Jamming transition as probed by quasistatic shear flow, *Phys. Rev. Lett.*, **102**, 218303+ (2009).

[39] C. Heussinger, P. Chaudhuri, and J.-L. Barrat, Fluctuations and correlations during the shear flow of elastic particles near the jamming transition, *Soft Matter*, **6**, 3050–3058 (2010).

[40] Y. Forterre and O. Pouliquen, Flows of dense granular media, *Ann. Rev. Fluid Mech.*, **40**, 1–24 (2008).

[41] P. Schall and M. van Hecke, Shear bands in matter with granularity, *Ann. Rev. Fluid Mech.*, **42**, 67–88 (2010).

[42] D. Weaire, J. D. Barry, and S. Hutzler, The continuum theory of shear localization in two-dimensional foam, *J. Phys.: Cond. Matt.r*, **22**, 193101+ (2010).

[43] P. A. Cundall, Numerical experiments on localization in frictional materials, *Ingenieur-Archiv*, **59**, 148–159 (1989).

[44] J. Goyon, A. Colin, G. Ovarlez, A. Ajdari, and L. Bocquet, Spatial cooperativity in soft glassy flows, *Nature*, **454**, 84–87 (2008).

[45] J. Lauridsen, M. Twardos, and M. Dennin, Shear-Induced stress relaxation in a Two-Dimensional wet foam, *Phys. Rev. Lett.*, **89**, 098303+ (2002).

[46] Y. Wang, K. Krishan, and M. Dennin, Impact of boundaries on velocity profiles in bubble rafts, *Phys. Rev. E*, **73**, 031401+ (2006).

[47] G. Katgert, M. Möbius, and M. van Hecke, Rate dependence and role of disorder in linearly sheared Two-Dimensional foams, *Phys. Rev. Lett.*, **101**, 058301+ (2008).

[48] G. Debrégeas, H. Tabuteau, and J. M. di Meglio, Deformation and flow of a Two-Dimensional foam under continuous shear, *Phys. Rev. Lett.*, **87**, 178305+ (2001).

[49] W. A. Beverloo, H. A. Leniger, and J. van de Velde, The flow of granular solids through orifices, *Chem. Eng. Sci.*, **15**, 260–269 (1961).

[50] Deming and A. L. Mehring, The gravitational flow of fertilizers and other comminuted solids, *Ind. Eng. Chem.*, **21**, 661–665 (1929).

[51] R. M. Nedderman, U. Tuzun, S. B. Savage, and G. T. Houlsby, The flow of granular materials–I : Discharge rates from hoppers, *Chem. Eng. Sci.*, **37**, 1597–1609 (1982).

[52] R. T. Fowler and J. R. Glastonbury, The flow of granular solids through orifices, *Chem. Eng. Sci.*, **10**, 150–156 (1959).

[53] D. C. Hong and J. A. McLennan, Molecular dynamics simulations of hard sphere granular particles, *Physica A: Statistical Mechanics and its Applications*, **187**, 159–171 (1992).

[54] F. Vivanco, S. Rica, and F. Melo, Dynamical arching in a two dimensional granular flow, *Granular Matter*, **14**, 563–576 (2012).

[55] A. Janda, I. Zuriguel, A. Garcimartín, L. A. Pugnaloni, and D. Maza, Jamming and critical outlet size in the discharge of a two-dimensional silo, *Europhys. Lett.*, **84**, 44002+ (2008).

[56] X. Hong, M. Kohne, and E. R. Weeks, Clogging of soft particles in 2D hoppers (2016).

[57] M. Asipauskas, M. Aubouy, J. A. Glazier, F. Graner, and Y. Jiang, A texture tensor to quantify deformations: the example of two-dimensional flowing foams, *Granular Matter*, **5**, 71–74 (2003).

[58] R. Benzi, M. Sbragaglia, P. Perlekar, M. Bernaschi, S. Succi, and F. Toschi, Direct evidence of plastic events and dynamic heterogeneities in soft-glasses, *Soft Matter*, **10**, 4615–4624 (2014).

[59] A. D. Gopal and D. J. Durian, Nonlinear bubble dynamics in a slowly driven foam, *Phys. Rev. Lett.*, **75**, 2610–2613 (1995).

[60] S. Tewari, D. Schiemann, D. J. Durian, C. M. Knobler, S. A. Langer, and A. J. Liu, Statistics of shear-induced rearrangements in a two-dimensional model foam, *Phys. Rev. E*, **60**, 4385–4396 (1999).

[61] J. P. Sethna, K. A. Dahmen, and C. R. Myers, Crackling noise, *Nature*, **410**, 242–250 (2001).

[62] D. Fisher, K. Dahmen, S. Ramanathan, and Y. Ben-Zion, Statistics of earthquakes in simple models of heterogeneous faults, *Phys. Rev. Lett.*, **78**, 4885–4888 (1997).

[63] K. Dahmen, D. Ertaş, and Y. Ben-Zion, Gutenberg-Richter and characteristic earthquake behavior in simple mean-field models of heterogeneous faults, *Phys. Rev. E*, **58**, 1494–1501 (1998).

[64] K. A. Dahmen, Y. B. Zion, and J. T. Uhl, Micromechanical model for deformation in solids with universal predictions for Stress-Strain curves and slip avalanches, *Phys. Rev. Lett.*, **102**, 175501+ (2009).

[65] S. Nasuno, A. Kudrolli, and J. Gollub, Friction in granular layers: Hysteresis and precursors, *Phys. Rev. Lett.*, **79**, 949–952 (1997).

[66] J. Krim, P. Yu, and R. P. Behringer, StickSlip and the transition to steady sliding in a 2D granular medium and a fixed particle lattice, *Pure and Applied Geophysics*, **168**, 2259–2275 (2011).

[67] J. S. Urbach, R. C. Madison, and J. T. Markert, Interface depinning, Self-

Organized criticality, and the barkhausen effect, *Phys. Rev. Lett.*, **75**, 276–279 (1995).

[68] I. Zuriguel, D. R. Parisi, R. C. Hidalgo, C. Lozano, A. Janda, P. A. Gago, J. P. Peralta, L. M. Ferrer, L. A. Pugnaloni, E. Clément, D. Maza, I. Pagonabarraga, and A. Garcimartín, Clogging transition of many-particle systems flowing through bottlenecks, *Scientific Reports*, **4**, 7324+ (2014).

[69] D. J. Durian, Bubble-scale model of foam mechanics:mMelting, nonlinear behavior, and avalanches, *Phys. Rev. E*, **55**, 1739–1751 (1997).

[70] E. Pratt and M. Dennin, Nonlinear stress and fluctuation dynamics of sheared disordered wet foam, *Phys. Rev. E*, **67**, 051402+ (2003).

[71] Y. Bertho, C. Becco, and N. Vandewalle, Dense bubble flow in a silo: An unusual flow of a dispersed medium, *Phys. Rev. E*, **73**, 056309+ (2006).

[72] M. Lundberg, K. Krishan, N. Xu, C. S. O'Hern, and M. Dennin, Reversible plastic events in amorphous materials., *Physical review. E, Statistical, nonlinear, and soft matter physics*, **77**, 041505+ (2008).

[73] R. R. Hartley and R. P. Behringer, Logarithmic rate dependence of force networks in sheared granular materials, *Nature*, **421**, 928–931 (2003).

[74] M. A. Aguirre, J. G. Grande, A. Calvo, L. A. Pugnaloni, and J. C. Géminard, Pressure independence of granular flow through an aperture, *Phys. Rev. Lett.*, **104**, 238002+ (2010).

[75] N. Hayman, L. Ducloué, K. Foco, and K. Daniels, Granular controls on periodicity of Stick-Slip events: Kinematics and Force-Chains in an experimental fault, *Pure and Applied Geophysics*, **168**, 2239–2257 (2011).

[76] P. Lafond, M. Gilmer, C. Koh, E. Sloan, D. Wu, and A. Sum, Orifice jamming of fluid-driven granular flow, *Phys. Rev. E*, **87**, 042204+ (2013).

[77] T. J. Wilson, C. R. Pfeifer, N. Mesyngier, and D. J. Durian, Granular discharge rate for submerged hoppers, *Papers in Physics*, **6**, 060009+ (2014).

[78] Y. Wang, K. Krishan, and M. Dennin, Statistics of microscopic yielding in sheared aqueous foams, *Phil. Mag. Letters*, **87**, 125–133 (2007).

[79] M. L. Falk and J. S. Langer, Dynamics of viscoplastic deformation in amorphous solids, *Phys. Rev. E*, **57**, 7192–7205 (1998).

[80] D. Chen, K. W. Desmond, and E. R. Weeks, Experimental observation of local rearrangements in dense quasi-two-dimensional emulsion flow, *Phys. Rev. E*, **91**, 062306+ (2015).

[81] R. Shah, H. Shum, A. Rowat, D. Lee, J. Agresti, A. Utada, L. Chu, J. Kim, A. Fernandez-Nieves, and C. Martinez, Designer emulsions using microfluidics, *Materials Today*, **11**, 18–27 (2008).

[82] M. B. Romanowsky, M. Heymann, A. R. Abate, A. T. Krummel, S. Fraden, and D. A. Weitz, Functional patterning of PDMS microfluidic devices using integrated chemo-masks, *Lab Chip*, **10**, 1521–1524 (2010).

[83] S. L. Anna, N. Bontoux, and H. A. Stone, Formation of dispersions using "flow focusing" in microchannels, *Applied Phys. Lett.*, **82**, 364–366 (2003).

[84] W.-A. C. Bauer, M. Fischlechner, C. Abell, and W. T. S. Huck, Hydrophilic PDMS microchannels for high-throughput formation of oil-in-water microdroplets and water-in-oil-in-water double emulsions, *Lab Chip*, **10**, 1814–1819 (2010).

[85] T. Franke, A. R. Abate, D. A. Weitz, and A. Wixforth, Surface acoustic wave (SAW) directed droplet flow in microfluidics for PDMS devices, *Lab Chip*, **9**, 2625–2627 (2009).

[86] S. Sugiura, M. Nakajima, S. Iwamoto, and M. Seki, Interfacial tension driven monodispersed droplet formation from microfabricated channel array, *Langmuir*, **17**, 5562–5566 (2001).

[87] D. Chen, K. W. Desmond, and E. R. Weeks, Topological rearrangements and stress fluctuations in quasi-two-dimensional hopper flow of emulsions, *Soft Matter*, **8**, 10486–10492 (2012).

[88] P. B. Umbanhowar, V. Prasad, and D. A. Weitz, Monodisperse emulsion generation via drop break off in a coflowing stream, *Langmuir*, **16**, 347–351 (2000).

[89] T. Thorsen, R. W. Roberts, F. H. Arnold, and S. R. Quake, Dynamic pattern formation in a Vesicle-Generating microfluidic device, *Phys. Rev. Lett.*, **86**, 4163–4166 (2001).

[90] A. S. Utada, A. Fernandez-Nieves, H. A. Stone, and D. A. Weitz, Dripping to

jetting transitions in coflowing liquid streams, *Phys. Rev. Lett.*, **99**, 094502+ (2007).

[91] V. Steijn, C. R. Kleijn, and M. T. Kreutzer, Predictive model for the size of bubbles and droplets created in microfluidic t-junctions, *Lab Chip*, **10**, 2513–2518 (2010).

[92] T. S. Majmudar and R. P. Behringer, Contact force measurements and stress-induced anisotropy in granular materials, *Nature*, **435**, 1079–1082 (2005).

[93] K. W. Desmond, *Structure, Dynamics, and Forces of Jammed Systems*, Ph.D. thesis, Emory University (2012).

[94] F. Aurenhammer, Power diagrams: Properties, algorithms and applications, *SIAM Journal on Computing*, **16**, 78–96 (1987).

[95] A. Okabe, B. Boots, K. Sugihara, S. N. Chiu, and D. G. Kendall, Spatial tessellations: Concepts and applications of voronoi diagrams, second edition, *Wiley Online Library*, pages i–xv (2008).

[96] J. C. Crocker and D. G. Grier, Methods of digital video microscopy for colloidal studies, *J. Colloid Interface Sci.*, **179**, 298–310 (1996).

[97] W. Losert, J. C. Geminard, S. Nasuno, and J. P. Gollub, Mechanisms for slow strengthening in granular materials, *Physical review. E, Statistical physics, plasmas, fluids, and related interdisciplinary topics*, **61**, 4060–4068 (2000).

[98] R. Albert, H. Jeong, and A.-L. Barabasi, Error and attack tolerance of complex networks, *Nature*, **406**, 378–382 (2000).

[99] N. Brodu, J. A. Dijksman, and R. P. Behringer, Spanning the scales of granular materials through microscopic force imaging, *Nature Comm.*, **6**, 6361+ (2015).

[100] H. M. Jaeger, S. R. Nagel, and R. P. Behringer, Granular solids, liquids, and gases, *Rev. Mod. Phys.*, **68**, 1259–1273 (1996).

[101] I. Zuriguel, Invited review: Clogging of granular materials in bottlenecks, *Papers in Physics*, **6** (2014).

[102] R. L. Brown and J. C. Richards, Two- and Three-Dimensional flow of grains through apertures, *Nature*, **182**, 600–601 (1958).

[103] H. Sheldon and D. Durian, Granular discharge and clogging for tilted hoppers, *Granular Matter*, **12**, 579–585 (2010).

[104] C. C. Thomas and D. J. Durian, Fraction of clogging configurations sampled by granular hopper flow, *Phys. Rev. Lett.*, **114**, 178001+ (2015).

[105] A. Mehta, G. C. Barker, and J. M. Luck, Cooperativity in sandpiles: statistics of bridge geometries, *J. Stat. Mech.*, **2004**, P10014+ (2004).

[106] L. A. Pugnaloni, M. G. Valluzzi, and L. G. Valluzzi, Arching in tapped deposits of hard disks, *Phys. Rev. E*, **73** (2006).

[107] M. C. Jenkins, M. D. Haw, G. C. Barker, W. C. K. Poon, and S. U. Egelhaaf, Does gravity cause Load-Bearing bridges in colloidal and granular systems?, *Phys. Rev. Lett.*, **107**, 038302+ (2011).

[108] F. C. Franklin and L. N. Johanson, Flow of granular material through a circular orifice, *Chem. Eng. Sci.*, **4**, 119–129 (1955).

[109] G. Lumay, J. Schockmel, D. Henández-Enríquez, S. Dorbolo, N. Vandewalle, and F. Pacheco-Vázquez, Flow of magnetic repelling grains in a two-dimensional silo, *Papers in Physics*, **7** (2015).

[110] A. Garcimart'ın, I. Zuriguel, L. A. Pugnaloni, and A. Janda, Shape of jamming arches in two-dimensional deposits of granular materials, *Phys. Rev. E*, **82**, 031306+ (2010).

[111] J. Tang, S. Sagdiphour, and R. P. Behringer, Jamming and flow in 2D hoppers, *AIP Conf. Proc.*, **1145**, 515–518 (2009).

[112] J. Tang and R. P. Behringer, How granular materials jam in a hopper, *Chaos: An Interdisciplinary Journal of Nonlinear Science*, **21**, 041107+ (2011).

[113] K. To, P.-Y. Lai, and H. K. Pak, Flow and jam of granular particles in a two-dimensional hopper, *Physica A: Statistical Mechanics and its Applications*, **315**, 174–180 (2002).

[114] K. To and P.-Y. Lai, Jamming pattern in a two-dimensional hopper, *Phys. Rev. E*, **66**, 011308 (2002).

[115] K. To, Jamming transition in two-dimensional hoppers and silos, *Phys. Rev. E*, **71**, 060301+ (2005).

[116] V. F. Weisskopf, Search for simplicity: Mountains, waterwaves, and leaky ceilings, *Am. J. Phys.*, **54**, 110–111 (1986).

[117] H. A. Janssen, Versuche über getreidedruck in silozellen, *Zeitschr. d. Vereines deutscher Ingenieure*, **39**, 1045–1049 (1895).

[118] J. H. Shaxby, J. C. Evans, and V. Jones, On the properties of powders. the variation of pressure with depth in columns of powders, *Trans. Faraday Soc.*, **19**, 60–72 (1923).

[119] P. G. de Gennes, Granular matter: a tentative view, *Rev. Mod. Phys.*, **71**, S374–S382 (1999).

[120] M. E. Cates, J. P. Wittmer, J. P. Bouchaud, and P. Claudin, Jamming, force chains, and fragile matter, *Phys. Rev. Lett.*, **81**, 1841–1844 (1998).

[121] S. Dorbolo, L. Maquet, M. Brandenbourger, F. Ludewig, G. Lumay, H. Caps, N. Vandewalle, S. Rondia, M. Mélard, J. van Loon, A. Dowson, and S. Vincent-Bonnieu, Influence of the gravity on the discharge of a silo, *Granular Matter*, **15**, 263–273 (2013).

[122] D. Helbing, Traffic and related self-driven many-particle systems, *Rev. Mod. Phys.*, **73**, 1067–1141 (2001).

[123] E. Altshuler, G. Mino, C. Perez-Penichet, L. D. Rio, A. Lindner, A. Rousselet, and E. Clement, Flow-controlled densification and anomalous dispersion of e. coli through a constriction, *Soft Matter*, **9**, 1864–1870 (2013).

[124] J. Rajchenbach, Flow in powders: From discrete avalanches to continuous regime, *Phys. Rev. Lett.*, **65**, 2221–2224 (1990).

[125] A. W. Jenike, Quantitative design of mass-flow bins, *Powder Technology*, **1**, 237–244 (1967).

[126] M. D. Haw, Jamming, Two-Fluid behavior, and Self-Filtration in concentrated particulate suspensions, *Phys. Rev. Lett.*, **92**, 185506 (2004).

[127] F. Fairbrother and A. E. Stubbs, 119. studies in electro-endosmosis. part VI. the "bubble-tube" method of measurement, *J. Chem. Soc.*, pages 527–529 (1935).

[128] F. P. Bretherton, The motion of long bubbles in tubes, *J. Fluid Mech.*, **10**, 166–188 (1961).

[129] J. Zhang, T. S. Majmudar, A. Tordesillas, and R. P. Behringer, Statistical properties of a 2D granular material subjected to cyclic shear, *Granular Matter*, **12**, 159–172 (2010).

[130] A. Baldassarri, F. Dalton, A. Petri, S. Zapperi, G. Pontuale, and L. Pietronero, Brownian forces in sheared granular matter, *Phys. Rev. Lett.*, **96**, 118002+ (2006).

[131] A. Lemaître and C. Caroli, Rate-Dependent avalanche size in athermally sheared amorphous solids, *Phys. Rev. Lett.*, **103**, 065501+ (2009).

[132] R. White and K. Dahmen, Driving rate effects on crackling noise, *Phys. Rev. Lett.*, **91**, 085702+ (2003).

[133] K. Krishan and M. Dennin, Viscous shear banding in foam, *Phys. Rev. E*, **78**, 051504+ (2008).

[134] C. Veje, D. Howell, and R. Behringer, Kinematics of a two-dimensional granular couette experiment at the transition to shearing, *Phys. Rev. E*, **59**, 739–745 (1999).

[135] E. Woldhuis, V. Chikkadi, M. S. van Deen, P. Schall, and M. van Hecke, Fluctuations in flows near jamming, *Soft Matter*, **11**, 7024–7031 (2015).

[136] Y. Jiang, P. J. Swart, A. Saxena, M. Asipauskas, and J. A. Glazier, Hysteresis and avalanches in two-dimensional foam rheology simulations, *Phys. Rev. E*, **59**, 5819–5832 (1999).

[137] M. Twardos and M. Dennin, Comparison between step strains and slow steady shear in a bubble raft, *Phys. Rev. E*, **71**, 061401+ (2005).

[138] J. Zhang, T. S. Majmudar, A. Tordesillas, and R. P. Behringer, Statistical properties of a 2D granular material subjected to cyclic shear (2009).

[139] A. Kabla and G. Debrégeas, Local stress relaxation and shear banding in a dry foam under shear, *Phys. Rev. Lett.*, **90**, 258303+ (2003).

[140] S. Cox, D. Weaire, and J. A. Glazier, The rheology of two-dimensional foams, *Rheologica Acta*, **43**, 442–448 (2004).

[141] F. Varnik, L. Bocquet, J. L. Barrat, and L. Berthier, Shear localization in a model glass, *Phys. Rev. Lett.*, **90**, 095702+ (2003).

[142] P. Coussot, J. Raynaud, F. Bertrand, P. Moucheront, J. Guilbaud, H. Huynh, S. Jarny, and D. Lesueur, Coexistence of liquid and solid phases in flowing Soft-Glassy materials, *Phys. Rev. Lett.*, **88**, 218301+ (2002).

[143] E. R. Weeks, J. C. Crocker, A. C. Levitt, A. Schofield, and D. A. Weitz, Three-Dimensional direct imaging of structural relaxation near the colloidal glass transition, *Science*, **287**, 627–631 (2000).

[144] C. Donati, J. F. Douglas, W. Kob, S. J. Plimpton, P. H. Poole, and S. C. Glotzer, Stringlike cooperative motion in a supercooled liquid, *Phys. Rev. Lett.*, **80**, 2338–2341 (1998).

[145] W. K. Kegel, Direct observation of dynamical heterogeneities in colloidal Hard-Sphere suspensions, *Science*, **287**, 290–293 (2000).

[146] A. Wyn, I. T. Davies, and S. J. Cox, Simulations of two-dimensional foam rheology: Localization in linear couette flow and the interaction of settling discs, *Euro. Phys. J. E: Soft Matter and Biological Physics*, **26**, 81–89 (2008).

[147] B. Utter and R. P. Behringer, Experimental measures of affine and nonaffine deformation in granular shear, *Phys. Rev. Lett.*, **100**, 208302+ (2008).

[148] G. Lois, A. Lemaître, and J. M. Carlson, Numerical tests of constitutive laws for dense granular flows, *Phys. Rev. E*, **72**, 051303+ (2005).

[149] W. C. K. Poon, E. R. Weeks, and C. P. Royall, On measuring colloidal volume fractions, *Soft Matter*, **8**, 21–30 (2012).

[150] V. Trappe and D. A. Weitz, Scaling of the viscoelasticity of weakly attractive particles, *Phys. Rev. Lett.*, **85**, 449–452 (2000).

[151] B. P. Tighe, E. Woldhuis, J. J. C. Remmers, W. van Saarloos, and M. van Hecke, Model for the scaling of stresses and fluctuations in flows near jamming, *Phys. Rev. Lett.*, **105**, 088303+ (2010).

[152] P. G. Debenedetti and F. H. Stillinger, Supercooled liquids and the glass transition, *Nature*, **410**, 259–267 (2001).

[153] C. Coulais, A. Seguin, and O. Dauchot, Shear modulus and dilatancy softening in granular packings above jamming, *Phys. Rev. Lett.*, **113** (2014).

[154] K. Nichol, A. Zanin, R. Bastien, E. Wandersman, and M. van Hecke, Flow-Induced agitations create a granular fluid, *Phys. Rev. Lett.*, **104**, 078302+ (2010).

[155] J. Geng and R. P. Behringer, Slow drag in two-dimensional granular media, *Phys. Rev. E*, **71**, 011302+ (2005).

[156] K. A. Reddy, Y. Forterre, and O. Pouliquen, Evidence of mechanically activated processes in slow granular flows, *Phys. Rev. Lett.*, **106**, 108301+ (2011).

[157] W. Herschel and R. Bulkley, Konsistenzmessungen von Gummi-Benzollösungen, *Kolloid-Z.*, **39**, 291–300 (1926).

[158] L. Bécu, S. Manneville, and A. Colin, Yielding and flow in adhesive and non-adhesive concentrated emulsions, *Phys. Rev. Lett.*, **96**, 138302+ (2006).

[159] P. Jop, V. Mansard, P. Chaudhuri, L. Bocquet, and A. Colin, Microscale rheology of a soft glassy material close to yielding, *Phys. Rev. Lett.*, **108**, 148301 (2012).

[160] J. Clara-Rahola, T. A. Brzinski, D. Semwogerere, K. Feitosa, J. C. Crocker, J. Sato, V. Breedveld, and E. R. Weeks, Affine and non-affine motions in sheared polydisperse jammed emulsions (2012).

[161] H. P. Zhang and H. A. Makse, Jamming transition in emulsions and granular materials, *Phys. Rev. E*, **72**, 011301+ (2005).